國立交通大學
光電工程學系暨研究所
博士論文

在氧化鋅磊晶薄膜物理特性中晶體缺陷結構的角色

The role of crystal defect structures in the physical properties of ZnO epitaxial films

研 究 生：劉維仁

指 導 教 授：徐嘉鴻 教授

謝文峰 教授

中華民國九十八年二月

在氧化鋅磊晶薄膜物理特性中晶體缺陷結構的角色

The role of crystal defect structures in the physical properties of ZnO epitaxial films

研究生：劉維仁　Student：Wei-Rein Liu

指導教授：徐嘉鴻教授　Advisor : Dr. Chia-Huang Hsu

謝文峰教授　Dr. Wen-Feng Hsieh

國立交通大學

光電工程研究所

博士論文

A Dissertation
Submitted to Department of Photonics and Institute of Electro-Optical Engineering
College of Electrical Engineering and Computer Science
National Chiao Tung University
In Partial Fulfillment of the Requirements
for the Degree of
Doctor of Philosophy
in
Electro-Optical Engineering

February 2009
Hsinchu, Taiwan, Republic of China

中華民國九十八年二月

誌 謝

時間的流逝真是快速，轉眼間我即將離開這個具有充滿回憶的地方。回想過去這幾年，在我腦海裡不斷的浮現出我所經歷的人事物，感覺到所有一切的事都才剛剛發生而已，沒想到我即將要畢業了要進入我人生的另一段旅程了。

本論文得以順利完成，首先我要感謝指導教授徐嘉鴻老師(大媽)及謝文峰老師，從碩士班到博士班這七年半來，老師對我的用心栽培與諄諄教誨，讓我的學識和能力不斷提升；在為學及做人態度上，潛移默化亦使我受益良多。其次要感謝口試委員們對論文的指正以及建議，使本論文更臻完善，也讓我對於未來研究的方向以及需要補強的地方了然於胸。 同時也要感謝清華大學洪銘輝及郭瑞年教授所提供高品質的成長於矽基板上氧化物緩衝層試片，使得實驗得以順利進行；還有東海大學簡世森學長在SPM相關分析與實驗的協助；以及同步輻射的學長世宏、永偉、志謨、同學恒睿、學弟碧軒對於XRD實驗儀器及真空技術所給予的協助及幫忙。

再來我要謝謝雷射診測實驗室那些曾經陪伴我一起走過這些年的夥伴夥伴們:阿政、裕奎及智章學長在實驗、課業、生活上的指導及協助，黃董、楊松及國峰對實驗室公務的分擔以及生活經驗分享；救過我一命的吳俊毅，沒有你那天睡在實驗室，我可能掛在9樓；此外還有實驗室內可愛的學弟妹們岳勳、宜錦、小郭、志遠、小豪、盈璇、延垠等，使得我在這幾年內的生活多采多姿，真是太感謝你們了。還有在廣鎵光電的蔡炯期學長，由於您的幫忙，使得laser MBE沒壞在我手裡，另外曾經跟我一起準備博士資格考的介任、明芳、阿達，沒有你們的陪伴，這一仗真的很難打。

我還要感謝的我的雙親給予我最大的支持與鼓勵。 在我的求學之路曾經跌倒了數次。您們都用最大的包容力，無怨無悔地支持及陪伴我，讓我站起來繼續走下去，希望我的表現沒有讓您們失望。也感謝我的另一半怡欣，在博士生生涯中，辛苦地陪我走過來。而今而後，但願我在為人處世上能夠學得更加謙卑與風趣。

最後感謝國科會的經費支持及交通大學奈米中心、同步輻射中心設備支援，才能讓本論文得以順利完成。

在氧化鋅磊晶薄膜物理特性中晶體缺陷結構的角色

研究生：劉維仁　　　　　　　　指導教授: 徐嘉鴻 教授
謝文峰 教授

國立交通大學光電工程學系暨研究所

摘要

我們利用雷射濺鍍法於不同的基板上成長高品質(0001) c 軸方向的氧化鋅(ZnO)磊晶薄膜;使用的基板包括 c 軸方向的藍寶石(α-Al_2O_3)基板和使用奈米厚的γ相氧化鋁(γ-Al_2O_3)或氧化釔(Y_2O_3)做為緩衝層的(111)方向的矽基板。針對氧化鋅長在藍寶石基板的系統，X 光繞射結果指出相對於 c 軸方向藍寶石基板的晶格，c 軸方向的氧化鋅其晶格沿著樣品表面法線方向旋轉 30 度，亦即兩者的橫向磊晶關係式為$[10\bar{1}0]_{sapphire} \parallel [11\bar{2}0]_{ZnO}$ 和 $[11\bar{2}0]_{sapphire} \parallel [01\bar{1}0]_{ZnO}$。在沿著薄膜表面法線及水平方向氧化鋅 X 光繞射峰寬度呈現巨大的差異，揭示出特定貫穿式差排(threading dislocation)類型的幾何關係；從 X 光繞射及穿透式電子顯微鏡實驗數據計算出的貫穿式差排密度顯示出大部分差排是刃(edge)差排類型。結合散射及顯微術量測結果，證實貫穿式差排並非均勻分布在氧化鋅薄膜內，氧化鋅薄膜是由柱狀的磊晶核芯周圍環繞高密度的貫穿式刃差排的磊晶晶粒所組成。藉由掃描式電容顯微鏡及導電式原子力顯微鏡針對貫穿式差排聚集處做電性量測，發現其平帶電壓平移及電位勢障提高，這歸因於高密度的貫穿式刃差排存在而造成的界面捕獲電荷密度。另一方面，由於貫穿式螺旋(screw)差排密度遠小於貫穿式刃差排，因此我們無法確認貫穿式螺旋差排的位置及其電性。

對 c 軸方向氧化鋅磊晶薄膜成長於使用超薄γ相氧化鋁為緩衝層的(111)矽基

板的結構分析結果顯示(111)方向的γ相氧化鋁磊晶緩衝層在沿磊晶緩衝層水平方向上存在兩個相互旋轉 60 度的晶疇，由此可以歸納三者的磊晶關係式為 $\{10\bar{1}0\}_{ZnO} \parallel \{22\bar{4}\}_{\gamma-Al_2O_3}\ or\ \{4\bar{2}\bar{2}\}_{\gamma-Al_2O_3} \parallel \{22\bar{4}\}_{Si}$。藉由 X 光繞射及光激發光譜實驗對氧化鋅磊晶層的結晶品質及光學性質研究，明確地將能帶邊緣輻射與深層缺陷輻射的強度比值與偏離垂直基板表面方向 X 光繞射峰φ掃描的訊號寬度聯繫起來；並且能帶邊緣輻射的寬度與氧化鋅(0002)繞射峰 θ–rocking curve 的寬度表現出很強的相依性；這些現象證明，能帶邊緣輻射與深層缺陷輻射強度的比值主要受貫穿式刃差排影響，而能帶邊緣輻射的寬度與貫穿式螺旋差排有關。

X 光繞射、光激發光譜及穿透式電子顯微鏡實驗證實，使用奈米厚、高介電質(high-*k*)材料氧化釔為緩衝層的(111)矽基板上可以成長同時具有高品質結晶及光學特性的氧化鋅磊晶薄膜。奈米厚氧化釔不僅可以提供成長完美氧化鋅磊晶薄膜的緩衝層，更可以成為氧化鋅及矽基板間的絕緣層。藉由 X 光繞射及穿透式電子顯微鏡量測，氧化鋅與氧化釔間的磊晶關係式遵循 $(0001)<2\bar{1}\bar{1}0>_{ZnO} \parallel (111)<10\bar{1}>_{Y_2O_3}$ 關係。氧化鋅晶格與氧化釔中的氧六方形次晶格(sub-lattice)具同向排列，二者之間的界面結構可以妥善地用 7 或 8 倍氧化鋅 $\{11\bar{2}0\}$ 的面距匹配 6 或 7 倍氧化釔 $\{4\bar{4}0\}$ 的面距的晶疇匹配磊晶模型描述；如此大的晶格不匹配可以藉由錯配差排(misfit dislocation)在界面上以 6 或 7 倍氧化釔 $\{4\bar{4}0\}$ 面距週期性地排列做調節，使得殘留應力明顯降低。即使是厚度只有 0.21 μm 的氧化鋅薄膜也展現優秀的光激發輻射特性。我們的實驗結果證明了氧化釔可以成為整合氧化鋅光電元件與以矽為主體的積體電路於一體的模板。

最後，從 X 光繞射、穿透式電子顯微鏡實驗數據，分別計算生長於上述三種基板的氧化鋅磊晶薄膜的貫穿式差排密度，結果顯示刃差排型式都是主要的結構缺陷；氧化鋅晶格總是與藍寶石基板，γ 相氧化鋁及氧化釔中氧的六方形次晶格呈同向排列，其所對應的二維次晶格晶格常數分別為 2.75、2.8、3.75 Å，與氧化鋅的晶格常數(3.249 Å)比較，預期沿水平方向的應力狀態對於氧化鋅成長於 c

軸方向的藍寶石、γ相氧化鋁應為壓縮應力；相反地，成長於氧化釔上的氧化鋅應為拉伸應力。然而，僅有成長在藍寶石上的氧化鋅被觀察到其沿水平方向呈壓縮應力；成長在γ相氧化鋁及氧化釔上的氧化鋅都是受到拉伸應力；事實上，對氧化鋅成長於使用其他氧化物為緩衝層的（111）矽基板上，包含氧化釓（Gd_2O_3）和參雜氧化釔的氧化鉿（Y_2O_3-doped HfO_2）等系統，所有氧化鋅磊晶薄膜都在水平方向受到拉伸應力；此外，存在於氧化鋅及氧化物緩衝層界面上的高密度錯配差排，調節了絕大部分晶格匹配所造成的應力。由於氧化鋅的熱膨脹係數（$\alpha \sim 4\text{-}6.5 \times 10^{-6}\ K^{-1}$）小於藍寶石基板($8 \times 10^{-6}\ K^{-1}$)，但大於矽基板的($8 \times 10^{-6}\ K^{-1}$)熱膨脹係數，這個趨勢與我們所觀察的氧化鋅成長於藍寶石基板及矽基板上的應力態相符，顯示氧化鋅磊晶層的應力態主要是由成長完成後冷卻過程中因磊晶薄膜與基板間熱膨脹係數差所導致的熱應力所支配；因為使用的氧化物緩衝層厚度為只有數奈米厚，因此在這些使用的氧化物緩衝層案例中，來自緩衝層熱應力的影響是可以忽略的。

The role of crystal defect structures in the physical properties of ZnO epitaxial films

Student: Wei-Rein Liu Advisor: Prof. Chia-Hung Hsu
Prof. Wen-Feng Hsieh

Department of Photonics & Institute of Electro-Optical Engineering
National Chiao Tung University

Abstract

High-quality c-oriented ZnO film has been epiaxially grown by utilizing PLD on the sapphire (0001), and Si (111) substrates with a nano-thick γ-Al_2O_3 or Y_2O_3 buffer layer, respectively. XRD results show a 30° offset between the $\{20\bar{2}0\}$ reflections of ZnO and sapphire verifies the in-plane epitaxial relationship of $[10\bar{1}0]_{sapphire} \parallel [11\bar{2}0]_{ZnO}$ and $[11\bar{2}0]_{sapphire} \parallel [01\bar{1}0]_{ZnO}$; the great disparity of X-ray diffraction line widths between the normal and in-plane reflections reveals the specific threading dislocation (TD) geometry of ZnO. The calculated TDs densities from XRD and TEM indicate most TDs are pure edge dislocations. From a combination of scattering and microscopic results, it is found that the TDs are not uniformly distributed in the ZnO films, but the ZnO films consist of columnar epitaxial cores

surrounded by annular regions of edge threading dislocations at a large density. The shift of flatband voltage and the raise of potential barrier at the aggregation of TDs observed by scanning capacitance microscope and conduction atomic force microscope were attributed to the interface trap densities caused by the existence of high-density edge threading dislocations. On the other hand, because the distribution of the screw TDs is much less than that of the edge TDs, we cannot identify the location of the screw TDs and their electrical properties.

The structural analysis of c-oriented ZnO epitaxial films on Si(111) substrates with a thin γ-Al_2O_3 buffer layer erveals that epitaxial γ-Al_2O_3 buffer layer consists of two (111) oriented domains rotated 60° from each other against the surface normal and the in-plane epitaxial relationship among ZnO layer, γ-Al_2O_3 buffer and Si buffer follows $(10\bar{1}0)_{ZnO} \parallel \{22\bar{4}\}_{\gamma-Al_2O_3}$ or $\{4\overline{22}\}_{\gamma-Al_2O_3} \parallel \{22\bar{4}\}_{Si}$. Studies on the crystalline quality and optical properties of ZnO epi-layers by XRD and PL measurements clearly indicate the intensity ratio of deep-level emission (DLE) to near-band edge emission (NBE) of ZnO films correlates with the width of ϕ–scan across off-normal reflection and the NBE linewidth is strongly dependent on the width of ZnO (0002) rocking curve. These observations manifest that the (I_{DLE}/I_{NBE}) ratio is dominantly affected by edge TDs and the line width of NBE emission is mainly related to screw TDs.

Both high-quality structural and optical properties of ZnO epi-film on Si (111) substrates using a nano-thick high-*k* oxide Y_2O_3 buffer layer was verified by XRD, TEM, and PL measurements. The nano-thick Y_2O_3 epi-layer serves not only as a buffer layer to ensure the growth of ZnO epi-film of high structural perfection but also as an insulator layer between ZnO and Si. Determined by XRD and TEM the epitaxial relationship between ZnO and Y_2O_3 follows $(0001)<2\bar{1}\bar{1}0>_{ZnO}\|(111)<10\bar{1}>_{Y_2O_3}$. ZnO lattice aligns with the hexagonal oxygen (O) sub-lattice in Y_2O_3 and the interfacial structure can be well described by domain matching epitaxy with 7 or 8 ZnO $\{11\bar{2}0\}$ planes matching 6 or 7 $\{4\bar{4}0\}$ planes of Y_2O_3; the large lattice mismatch is thus accommodated by the misfit dislocations (MDs) localized at the interface with a periodicity of 6(7) times of $(4\bar{4}0)_{Y_2O_3}$ inter-planar spacing, leading to a significant reduction of residual strain. Superior photoluminescence were obtained even for ZnO-films as thin as 0.21 μm. Our results demonstrate that the Y_2O_3 layer well serves as a template for integrating ZnO based optoelectronic devices with Si substrate.

Finally, the calculated TDs densities from XRD and TEM indicate most TDs are pure edge dislocations for ZnO epi-films on sapphire (0001), γ-Al_2O_3/Si(111), or Y_2O_3 /Si(111) substrates. The lattice of ZnO is always aligned with the hexagonal O sub-lattice in the oxide layer underneath. The lattice constant a_o of 2D hexagonal oxygen sub-lattice are 2.75, 2.80, 3.75 Å for sapphire, γ-$Al_2O_3$and Y_2O_3, respectively. As compared with the lattice constant a of ZnO (3.249 Å), compressive strain along in-plane direction is expected for ZnO epi-film grown on sapphire (0001) and γ−Al_2O_3(111). In contrast, the expected lateral strain is tensive for ZnO epi-film on Y_2O_3(111). However, compressive lateral strain is only observed for ZnO epi-layers grown on sapphire. On both γ-Al_2O_3 and Y_2O_3 buffer layers, ZnO epi-films bear tensile strain. In fact, for ZnO epi-film grown on Si(111) using other oxide buffer layers, including Gd_2O_3, and Y_2O_3 doped HfO_2, all ZnO epi-film suffers tensile strain along in-plane direction. Moreover, high density of MDs at ZnO/oxide-buffer interface should accommodate most of the strain caused by lattice mismatch. It is noted that the thermal expansion coefficient of ZnO ($\alpha \sim 4\text{-}6.5 \times 10^{-6}\ K^{-1}$) is less than that of sapphire ($8 \times 10^{-6}\ K^{-1}$) but larger than that of Si ($2.6\text{-}3.6 \times 10^{-6}\ K^{-1}$). The trend agrees with the observed strain state of ZnO layer grown on sapphire and Si. This observation strongly suggests that the strain of the ZnO-epi layers is dictated by the thermal stress built up during the post-growth cooling. Because of the nano-thickness of the employed buffer layers, the influence coming from the buffer is negligible in these cases.

Contents

Chapter 3 Experimental setups and procedures 62

List of Figures

List of Tables

Chapter 1 Introduction

1.1 Basic properties of ZnO, overview of ZnO thin film growth and related problems

1.1.1 Basic properties of ZnO and its potential applications

ZnO is an ideal material for applications in UV light emitters, varistors, transparent high power electronics, surface acoustic wave devices, piezoelectric transducers, and chemical as well as gas sensing. ZnO is a II-VI compound semiconductor with ionicity between covalent and ionic compounds. At ambient conditions, the thermodynamically stable form of ZnO has a hexagonal wurtzite structure belonging to space group C_{6v}^{4} (Schoenflies type symbol) or equivalently $P6_3mc$ (Hermann-Mauguin type symbol) (SG number186) with two formula units per primitive cell, as schematically shown in Fig. 1-1. Its lattice constants are a = 3.249 Å and c = 5.2063 Å.

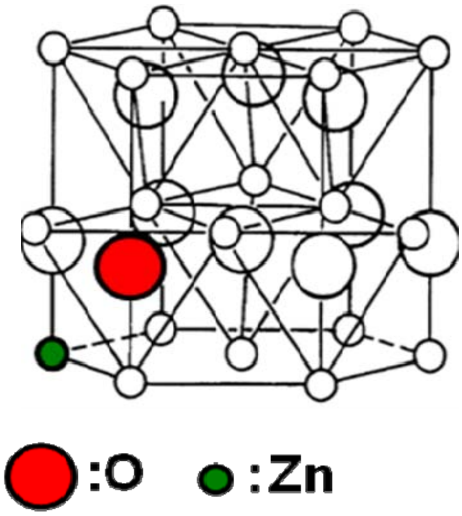

Fig.1-1 Atomic arrangement of wurtzite ZnO

The basic properties of ZnO are summarized in Table 1-1 [1]. ZnO is a direct band-gap semiconductor with energy gap $E_g = 3.37$ eV at room temperature (RT). An attractive feature of ZnO is its large exciton binding energy, 60 meV, which is about three times larger than that of GaN or ZnSe [2, 3]. ZnO thus has great thermal stability for excitons and offers a great application prospect for lasers with small thresholds even at high temperatures. The band gap of ZnO can be tailored by divalent substitution at the cation site to achieve band gap engineering. For example, Cd substitution leads to a reduction of band gap to ~3.0 eV [4]. Substituting Zn by Mg in epitaxial films can increase the band gap to approximately 4.0 eV while still maintaining the wurtzite structure [5].

Electron doping in nominally undoped ZnO has been attributed to Zn interstitials, oxygen vacancies, or hydrogen [6-11]. The intrinsic defect levels that lead to *n*-type doping lie approximately 0.01–0.05 eV below the conduction band. The photoluminescence (PL) spectrum of undoped ZnO measured at RT is shown in Fig. 1-2. The strong near-band-edge (NBE) UV emissions at ~3.28 eV are attributed to exciton states; the features in visible region around 2.3 eV are ascribed to the deep-level defect states. In 2005, Tsukazaki *et al.* demonstrated the first blue light-emitting diode (LED) of homostructural *p*-*i*-*n* junction based on ZnO [12]. The dominant feature in electroluminescence spectrum, as shown in Fig. 1-3, does not originate from the recombination from near band edge but from deep level emission. This provides strong evidence that defects play a crucial role in the performance of ZnO-based photoelectronic devices.

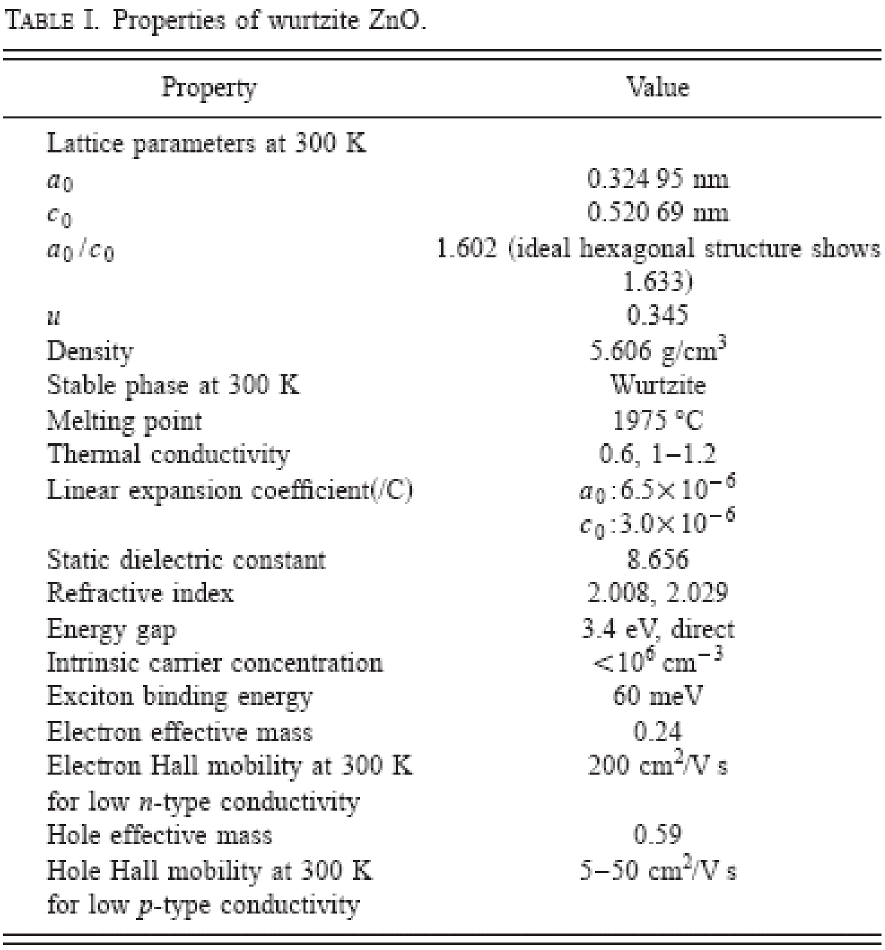

TABLE I. Properties of wurtzite ZnO.

Property	Value
Lattice parameters at 300 K	
a_0	0.324 95 nm
c_0	0.520 69 nm
a_0/c_0	1.602 (ideal hexagonal structure shows 1.633)
u	0.345
Density	5.606 g/cm^3
Stable phase at 300 K	Wurtzite
Melting point	1975 °C
Thermal conductivity	0.6, 1–1.2
Linear expansion coefficient(/C)	a_0:6.5×10^{-6} c_0:3.0×10^{-6}
Static dielectric constant	8.656
Refractive index	2.008, 2.029
Energy gap	3.4 eV, direct
Intrinsic carrier concentration	$<10^6$ cm^{-3}
Exciton binding energy	60 meV
Electron effective mass	0.24
Electron Hall mobility at 300 K for low *n*-type conductivity	200 cm^2/V s
Hole effective mass	0.59
Hole Hall mobility at 300 K for low *p*-type conductivity	5–50 cm^2/V s

Table 1-1 Physical properties of wurtzite ZnO. [1]

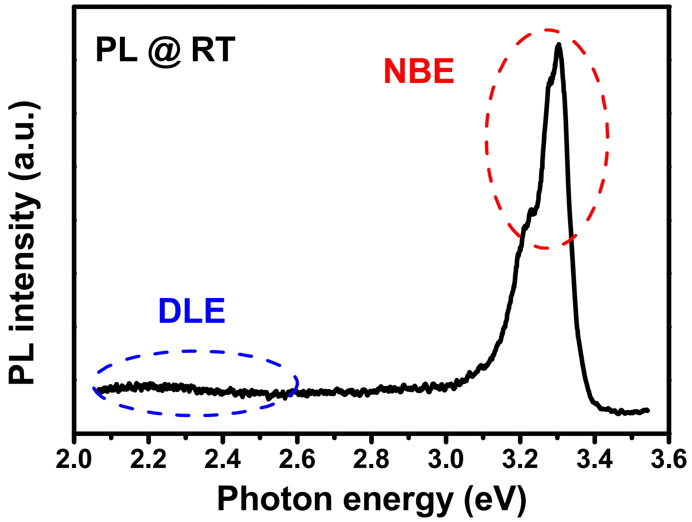

Fig.1-2 The room temperature PL spectrum of ZnO epi-film grown on c-plane sapphire.

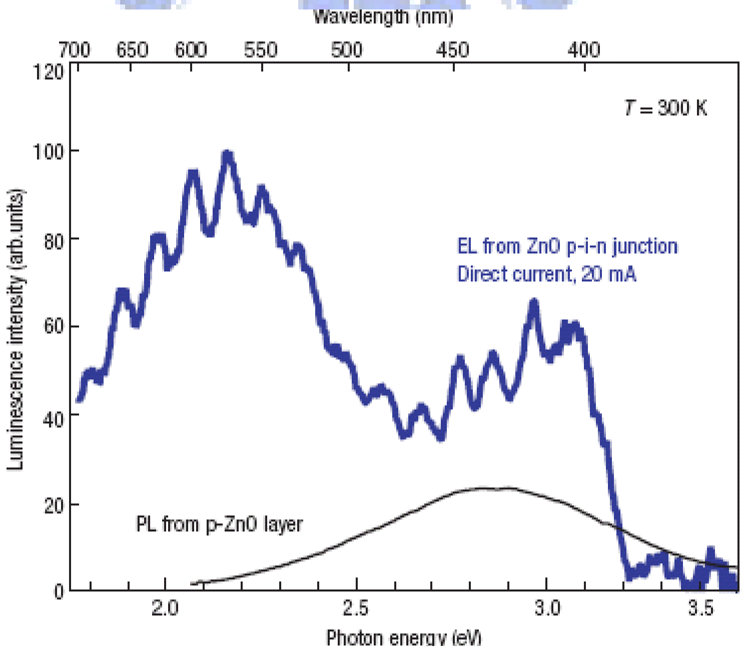

Fig. 1-3 Electroluminescence spectrum from a *p–i–n* junction (blue) and PL spectrum of a *p*-type ZnO film measured at 300 K. The *p–i–n* junction was operated by feeding in a direct current of 20 mA. [12]

1.1.2 Current status of epitaxial ZnO thin film growth and problems

Sapphire has been used most frequently for epitaxial growth partly because high quality, large-size single crystal wafers are easily available. In the case of ZnO heteroepitaxial growth, sapphire (α-Al_2O_3), primarily with the (0001)-plane normal (c-plane) and in some cases with the $(11\bar{2}0)$-plane normal (*a*-plane), is the most commonly used substrate. Sapphire has a rhombohedral crystal structure with lattice constants a = 4.758 Å and c = 12.991 Å. Because of the significant differences in structure and lattice parameters, it has been a challenge to grow high quality ZnO epitaxial films on sapphire. Besides, the significant difference in thermal expansion coefficient between ZnO and sapphire [14] introduces additional strain upon post-growth cooling. ZnO grown on c-plane sapphire usually has the epitaixal relationship of $(0001)[11\bar{2}0]_{ZnO} \parallel (0001)\ [10\bar{1}0]_{sapphire}$, under which ZnO lattice is rotated 30^o against the c-axis of sapphire and lattice mismatch reduces from 32% to 18%. Narayan *et al.* proposed that ZnO films grew on (0001) Al_2O_3 substrate by domain matching epitaxy (DME) with 5 or 6 $(21\bar{1}0)$ planes of ZnO matching 6 or 7 $(30\bar{3}0)$ planes of sapphire at interface [13]. Consequently, most of the lattice mismatch is accommodated by the misfit dislocations (MDs) which are confined at the interface. However, there still exist high densities of threading dislocations (TDs) (typically 10^9~10^{11} cm^{-2}) extending throughout the entire thickness of ZnO epitaxial films, which is still a major problem limiting the performance of ZnO based devices. Therefore, the reduction of defect density is a principal target to pursue for high-quality epitaxial ZnO growth.

The other attractive substrate is silicon because of many advantages, such as low costs, excellent crystalline quality, large-area availability of Si wafer and, most importantly, the unique opportunity of integrating well-established Si electronics with ZnO-based optoelectronic devices. Hence, many efforts have been put to grow high-quality ZnO on Si. Unfortunately, direct growth of epitaxial ZnO films on Si is a difficult task due to large diversity in lattice constants (15.4%) and thermal expansion coefficient (56%) as well as the formation of amorphous SiO_2 layer at ZnO/Si interface [15,16]. Either polycrystalline or highly textured ZnO films with (0001)-plane normal were commonly obtained on Si (111) substrates [17]. Therefore, significant efforts have been made to use various materials as the buffer layer for subsequent ZnO growth and quite some progress has been achieved. Nevertheless, the growth of high-quality ZnO epi-films on Si is still regarded as an arduous challenge.

1.2 Motivation

For heteroepitaxial systems with large mismatches in lattice parameters and thermal expansion coefficients between the deposited layer and substrate, significant strain is built up in the grown layer. When the stored strain energy exceeds certain threshold, the heterostructure becomes metastable and defects are generated to release the large strain energy. As revealed by many studies on another popular optoelectronic semiconductor - GaN thin films, which has the same wurtzite structure as ZnO, defects intimately affect the electrical and optical properties of the films, including the degradation of devices through carrier scattering [18], nonradiative recombination [19], and reverse-bias leakage current [20, 21]. However, the influence of defects on the physical properties of epi-ZnO films is still not well understood. A comprehensive knowledge of structural defects in ZnO epi-layer and their influence on the optical and electrical properties is valuable especially for the design of photoelectronic devices. In this dissertation, the growth of high quality ZnO epitaxial films by pulsed-laser deposition (PLD) on sapphire (0001) and Si(111) using various oxide buffer layers including γ-Al_2O_3 and Y_2O_3 is reported. The microstructure of ZnO epi-films were thoroughly studied by X-ray diffraction (XRD), transmission electron microscopy (TEM) and atomic force microscopy (AFM). The electrical properties of these epi-films were examined by using scanning capacitance microscopy (SCM) and conductive atomic force microscopy (C-AFM). photoluminescence (PL) was employed to characterize the optical properties of the ZnO films. Based on the obtained results, the correlations between structural properties, in particular the structural defects, and electric as well as optical properties are established.

1.3 Organization of the dissertation

This dissertation is organized as follows. A brief review of epitaxial growth, crystal structures, dislocation theory, and defect analysis using XRD and TEM is given in chapter 2. The basic theory of the techniques used to characterize the samples including XRD, scanning probe microscopy (SPM) and PL are also summarized in the same chapter. Chapter 3 contains the details of sample preparation and a description of experimental setups. In chapter 4, the defect structures of high quality ZnO epitaxial films grown on c-plane sapphire are reported; the correlation between TDs and electrical properties, characterized by SCM and C-AFM, of these films is also discussed. Chapter 5 consists of the study on the structural and optical characteristics of ZnO epitaxial films on Si(111) substrates with a thin γ-Al_2O_3 buffer layer; the correlation between various types of TDs and the features in PL spectrum is described. In chapter 6, we show both high-quality crystalline and optical properties of ZnO epi-films grown on Si (111) substrates using a nano-thick Y_2O_3 buffer layer and a discussion of the role of MDs at the ZnO/Y_2O_3 interface in stabilizing the structure of this heteroepitaxial system is also presented. Finally, chapter 7 contains the conclusion of the studies in the ZnO epi-films and the topics proposed for future studies.

References

[1] D. P. Norton, Y. W. Heo, M. P. Ivill, K. Ip, S. J. Pearton, M. F. Chisholm, and T. Steiner, *Materials Today* **7**, 34 (2004).

[2] D. M. Bagnall, Y. F. Chen, Z. Zhu, T. Yao, S. Koyama, M. Y. Shen, andT. Goto, *Appl. Phys. Lett.* **70**, 2230 (1997).

[3] Y. F. Chen, D. M. Bagnall, H. J. Koh, K. T. Park, J. Hiraga, Z. Zhu , and T. Yao, *J. Appl. Phys.* **84** 3912 (1998).

[4] L. K. Singh and H. Mohan, *Indian J. Pure Appl. Phys.* **13**, 486 (1975).

[5] A. Ohtomo, K. Tamura, M. Kawasaki, T. Makino, Y. Segawa, Z. K. Tang, G. Wong, Y. Matsumoto, and H. Koinuma, *Appl. Phys. Lett.* **77**, 2204 (2000).

[6] D. C. Look, J. W. Hemsky, and J. R. Sizelove, *Phys. Rev. Lett.* **82**, 2552 (1999)

[7] B. J. Jin, S. H. Bae, S. Y. Lee, and S. Im, *Mater. Sci. Eng,* B **71**, 301(2000).

[8] D. M. Hofmann, A. Hofstaetter, F. Leiter, H. Zhou, F. Henecker, B. K. Meyer, S. B. Orlinskii, J. Schmidt, and P. G. Baranov, *Phys. Rev. Lett.* **88**,045504 (2002).

[9] C. G. Van de Walle, Phys. *Status Solidi B* **229**, 221 (2002).

[10] S. F. J. Cox, E. A. Davis, P. J. C. King, J. M. Gil, H. V. Alberto, R. C. Vilao, J. Piroto Duarte, N. A. De Campos, and R. L. Lichti, *J. Phys.: Condens. Matter* **13**, 9001 (2001)

[11] C. G. Van de Walle, *Phys. Rev. Lett.* **85**, 1012 (2000).

[12] A. Tsukazaki, A. Ohtomo, T. Onuma, M. Ohtani, T. Makino, M. Sumiya, K. Ohtani, S. F. Chichibu, S. Fuke, Y. Segawa, H. Ohno, H. Koinuma, and M. Kawasaki, *Nature Mater.* **4** 42 (2005)

[13] J. Narayan, andB. C. Larson, *J. Appl. Phys*. **93**, 278 (2003).

[14] F. Vigué, P. Vennéguès, S. Vézian, M. Laügt, and J.-P. Faürie, *Appl. Phys. Lett.* **79**, 194 (2001).

[15] Y. Z. Yoo, T. Sekiguchi, T. Chikyow, M. Kawasaki, T. Onuma, S. F. Chichibu, J. H. Song, and H. Koinuma, *Appl. Phys. Lett.* **84**, 502(2004).

[16] A. Nahhas, H. K. Kim, and J. Blachere, *J. Appl. Phys. Lett.* **78**, 1511(2001).

[17] H. M. Cheng, H. C. Hsu, S. Yang S.C. Y. Wu, Y. C. Lee, L.J. Lin, and W. F. Hsieh, *Nanotechnology* **16**, 2882 (2005).

[18] H. M. Ng, D. Doppalapudi, T. D. Moustakas, N. G. Weimann, and L. F. Eastman, *Appl. Phys. Lett.* **73**, 821 (1998).

[19] T. Sugahara, H. Sato, M. Hao, Y. Naoi, S. Tottori, K. Yamashita, K. Nishino, L. T. Romano, and S. Sakai S. (1998). *Jpn. J. Appl. Phys. Part* 2, **37**, L398 (1998).

[20] J. W. P. Hsu, M. J. Manfra, R. J. Molnar, B. Heying, and J. S. Speck, *Appl. Phys. Lett.* **81**, 79(2002).

[21] E. J. Miller, D. M. Schaadt, E. T.Yu, C. Poblenz, C. Elsass, and J. S. Speck, *J. Appl. Phys.* **91**, 9821 (2002).

Chapter 2 Theoretical background and characterization techniques

2.1 Epitaxy

Epitaxy refers to the growth on a crystalline substrate of a crystalline substance that mimics the orientation of the substrate. If a film is deposited on a substrate of the same compositions, the process is called homoepitaxy; otherwise it is called heteroepitaxy [1]. Depending on the degree of lattice mismatch, $(a_f - a_s)/a_s$, where a_f and a_s, respectively, denote the lattice constants of film and substrate, the epitaxy of heterosystems can be modeled by lattice mismatch epitaxy (LME) or domain match epitaxy (DME). A brief review of the two epitaxy models and the difference between them is given in the following.

2.1.1 Lattice mismatch epitaxy (LME)

The well-established lattice-matching epitaxy is suitable for describing systems with small lattice misfit (less than 7%–8%). The deposited layer grows by one-to-one matching of lattice constants across the film–substrate interface. The film grows pseudomorphically up to a ‘‘critical thickness’’ where it becomes energetically favorable for the film to contain dislocations [2, 3]. In this case, the dislocations are generated at the film surface and glide to the interface; therefore, the Burgers vectors and planes of the dislocations are dictated by the slip vectors and glide planes of the crystal structure of the film [4]. Smaller lattice misfit leads to smaller elastic energy and coherent epitaxy is formed. Above this misfit, it was surmised that the film will grow textured or largely polycrystalline.

2.1.2 Domain mismatch epitaxy (DME)

The DME concept represents a considerable departure from the conventional LME for hetero-systems with lattice misfit less than 7–8%. For hetero-systems with larger lattice misfit, integral multiples of lattice planes - domains, instead of lattice constants, match across the film–substrate interface. The size of the domain equals integral multiples of planar spacing in the DME. The detailed description of DME model can be consulted in Ref [5].

The hetero-system of ZnO grown on c-plane sapphire is an example of DME. The lateral lattice constants of ZnO and sapphire are 3.249 and 4.758 Å, respectively, yielding a lattice mismatch of -31.7%. Figure 2-1(a) shows high-resolution TEM cross-section image taken with electrons incident along ZnO $[1\bar{1}00]$ pole, in which an atomically sharp interface between ZnO epi-film and substrate is demonstrated. The Fourier-filtered image of Fig. 2-1 (b) is shown in Fig. 2-1 (b), in which the vertical lines above and below the interface are associated with the $(2\bar{1}\bar{1}0)$ planes of ZnO film and the $(01\bar{1}0)$ planes of sapphire substrate, respectively. The image clearly manifests the matching of 5 or 6 $(2\bar{1}\bar{1}0)$ planes of ZnO with 6 or 7 $(30\bar{3}0)$ planes of sapphire at the interface. The corresponding diffraction pattern, shown in

Fig. 2-1 (c), confirms the relative orientation between film and substrate. The *c*-plane of ZnO lies on the basal plane of sapphire with a 30° in-plane rotation, as illustrated in Fig. 2-1(d), which leads to the alignment of the $\{30\bar{3}0\}$ planes of sapphire with the $\{2\bar{1}\bar{1}0\}$ planes, i.e. *a* planes, of ZnO. Thus, the domain consisted of an average 5.5 ZnO $\{2\bar{1}\bar{1}0\}$ planes with size of 8.935 Å matches nicely with the domain made of an average 6.5 sapphire $\{30\bar{3}0\}$ planes with size of 8.928 Å. The DME of ZnO on (0001) sapphire has also been demonstrated by *in-situ* x-ray diffraction measurement during initial stage of film growth [5]. Narayan *et al.* applies the time-resolved x-ray crystal truncation rod (CTR) measurements made after each excimer laser ablation pulse. They found the surface structure transients associated with ZnO clustering and crystallization last for about 2 sec. following the abrupt ~5 μs duration of laser deposition and discovered the rapid relaxation of ZnO films on sapphire. The relaxation process requires the creation of dislocations, which involves nucleation and propagation of dislocations. The rapid relaxation process in DME is consistent with the fact that the critical thickness under these large misfits is less than 1 monolayer [6]. As a result, dislocations can nucleate during initial stages of growth and most defects are confined to the region near the interface, leading to fewer defects in the interior of the deposited layer, the active region of the device.

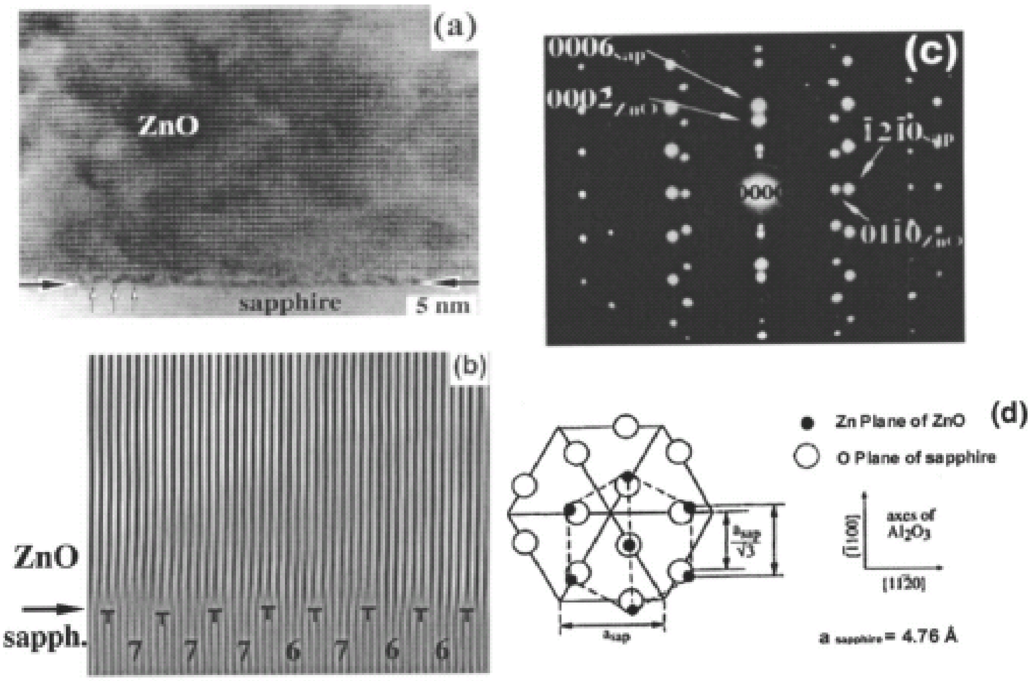

Fig. 2-1 (a) High-resolution TEM cross section image with $(01\bar{1}0)$ foil plane of sapphire and $(2\bar{1}\bar{1}0)$ plane of ZnO showing domain epitaxy in ZnO/apphire system; (b) Fourier-filtered image of the region near interface manifesting the matching of ZnO $(2\bar{1}\bar{1}0)$ and sapphire $(30\bar{3}0)$ planes with a 5/6 and 6/7 ratio; (c) corresponding electron diffraction pattern showing the alignment of planes in ZnO and sapphire; and (d) schematic of atomic arrangement in the basal plane of ZnO and sapphire. [5]

2 .2 Structural defect in epitaxy

The structural defects in epitaxial film are generally categorized as threading and misfit dislocation, stacking fault, oval defect, and etc., as illustrated in Fig. 2-2. The most important structural defect in epitaxial films is the dislocation which also named as line defect. Dislocations can be further clarified into two sections according to their location in epitaxial films. One is threading dislocations (TDs) which extends throughout the entire thickness of an epitaxial film and the other one is misfit dislocation (MDs) located mainly at the interface between the substrate and the deposited layer during initial stage of epitaxy. In following section, a brief review of dislocation theory is given.

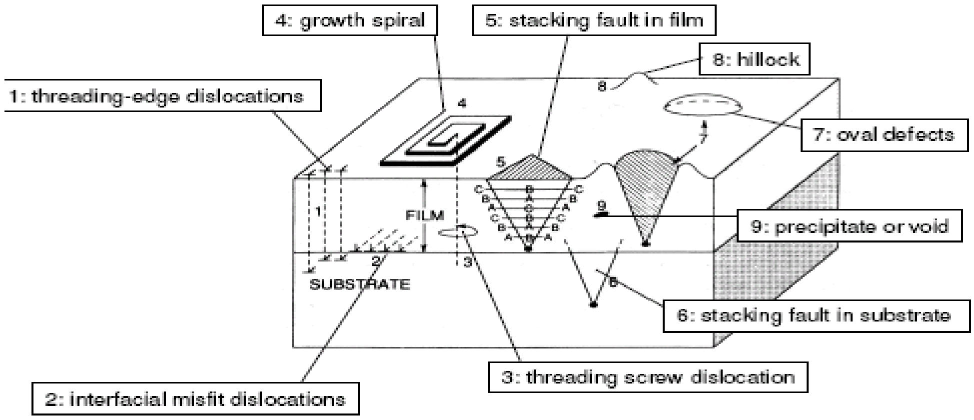

Fig. 2-2 The typical structural defect in epitaxy

2.2.1 Dislocations

2.2.1.1 The theory of dislocation

A dislocation is a crystallographic defect, or irregularity, within a crystal structure. The presence of dislocations strongly influences the properties of materials. Some types of dislocations can be visualized as being caused by the termination of a plane of atoms in the middle of a crystal. In such a case, the surrounding planes are not straight but bend around the edge of the terminating plane so that the crystal structure is perfectly ordered on either side. According to the relationship between Burgers vector and dislocation line, there are two primary types of dislocations, screw and edge dislocations. Mixed dislocation is a combination of the two types of dislocation [7-9]. Some characteristics of both screw and edge dislocations are summarized below.

1. Screw dislocations:

A screw dislocation is much harder to visualize. Imagine cutting a crystal along a plane and slipping one half across the other by a lattice vector, the halves will fit back together without leaving a defect. If the cut only goes part way through the crystal and then slipped, the boundary of the cut is a screw dislocation. It comprises a structure in which a helical path is traced around the linear defect (dislocation line) by the atomic planes in the crystal lattice, as shown in Fig.2-3 (a). For pure screw dislocations, the Burgers vector ***b*** is parallel to the dislocation line. A screw dislocation moves (in the slip plane) in a direction perpendicular to the Burger vector (slip direction) cause the strain and elastic stress field surrounding a screw dislocation, as shown in Fig. 2-4 (a) are written as

$$\varepsilon = \frac{b}{2\pi r} \text{ , } \tau = \mu\varepsilon = \frac{\mu b}{2\pi r} \qquad (2\text{-}1)$$

Here r and μ are the radius of the Burgers circuit and the shear modulus of the material, respectively. According to the linear elasticity theory, the strain energy density in the stress field of the screw dislocation is $\tau^2/2\mu$. The strain energy per unit length of the screw dislocation can be estimated with the following integration.

$$W_s = \int_{r_0}^{r'} \left(\frac{\mu b}{2\pi r}\right)^2 \left(\frac{1}{2\mu}\right) 2\pi r dr = \frac{\mu b^2}{4\pi} \ln\frac{r'}{r_0} \qquad (2\text{-}2)$$

where W_s is the energy per unit length of the screw dislocation, r_0 is the inner radius that excludes the dislocation core and *r'* is an outer limiting radius for integration. It is normally assumed that linear elasticity does not hold below $r_0 \sim b$.

2. *Edge dislocations:*

An edge dislocation is a line defect where an extra half-plane of atoms is introduced mid way through the crystal, distorting nearby planes of atoms. When enough force is applied from one side of the crystal structure, this extra plane passes through planes of atoms breaking and joining bonds with them until it reaches the grain boundary. The "extra half-plane" concept of an edge dislocation can be used to illustrate lattice defects such as dislocations, as shown in Fig. 2-3(b). An edge lies perpendicular to its Burgers vector and moves in the direction of the Burgers vector. The stress field surrounding an edge orientation is more complicated than that surrounding a screw dislocation. It is generally assumed that an edge dislocation lies in an infinitely large and elastically isotropic material. Assuming the dislocation line coincides with the z-direction, the stress at a point with polar coordinates r and θ, as shown in Fig. 2-4 (b), can be calculated based on the elasticity theory and has the following component:

$$\sigma_{rr} = \sigma_{\theta\theta} = \frac{-\mu b}{2\pi(1-\nu)}.(\frac{\sin\theta}{r}), \quad \tau_{r\theta} = \frac{\mu b}{2\pi(1-\nu)}.(\frac{\cos\theta}{r}) \qquad (2\text{-}3)$$

where the σ_{rr} and $\sigma_{\theta\theta}$ are tensile stress components in the *r* and *θ* direction, $\tau_{r\theta}$ is the shear force, and ν denotes the Possion's ratio. The strain energy per unit length of edge dislocation, W_E is given as

$$W_{\mathrm{E}} = \int_{r_0}^{r'} \left(\frac{\mu b}{2\pi r}\right)^2 \left(\frac{1}{2\mu}\right) 2\pi r dr = \frac{\mu b^2}{4\pi(1-\nu)} \ln\frac{4r'}{b} \qquad (2\text{-}4)$$

3. Mixed dislocations

The mixed type is the combination of edge and screw dislocation.

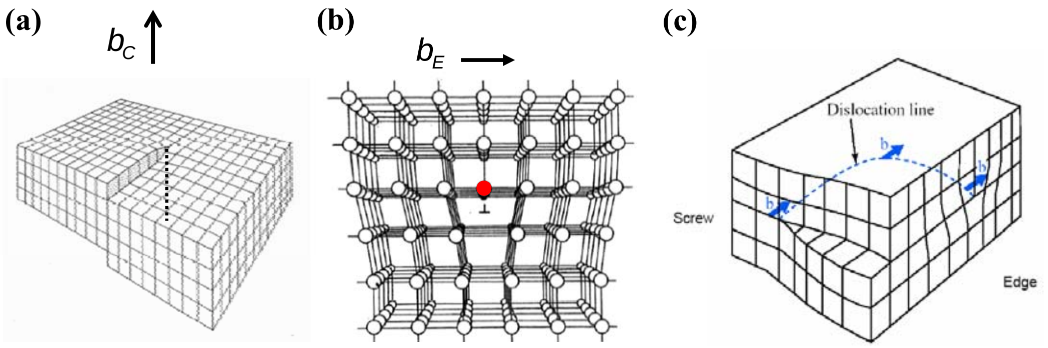

Fig. 2-3 Three types of dislocation are screw (a), edge (b), and mixed (c) types, respectively.

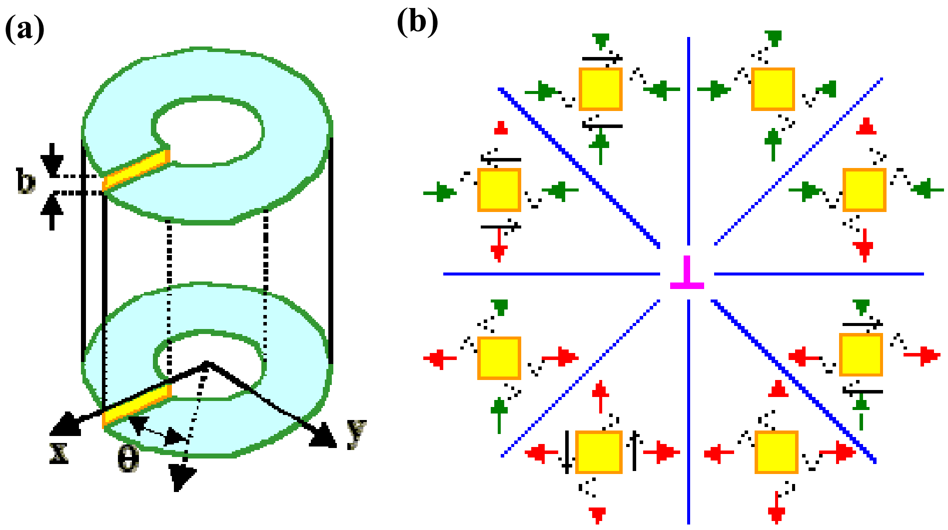

Fig. 2-4 The stress and strain associated with screw (a) and edge (b) dislocation.

2.2.1.2 The influence of dislocation on electrical and optical properties

Dislocations are known to exhibit a wide variety of effects that can have a significant impact on the mechanical, electrical, and optical properties of materials [8, 10]. As reported in a large number of studies in GaN, dislocations indeed influence the optical properties and device performance through nonradiative recombination. Table 2-1 summarizes the influence of threading dislocations (TDs) on electrical and optical properties for GaN epitaxial film.

Table 2-1. The influence of TDs on electrical and optical properties of GaN epitaxial film

TDs type	Electrical property	Optical property
Screw TDs	Leakage current under reverse bias voltage [11, 12]	Degradation of PL intensity at NBE [13, 14]
Edge TDs	Extra negative charge [15], nonconductive [16]	Enhancement of PL intensity at DLE [17, 18]

2.3 Characterization techniques

2.3.1 X-ray diffraction (XRD)

The reciprocal lattice plays a fundamental role in most analytic studies of periodic structures, particularly in the theory of diffraction. Using the information collected in reciprocal space, one can infer the atomic arrangement of a crystal in real space. The following sections give an introduction of crystal structure and corresponding reciprocal space, the basic theory of diffraction, a description of both the Laue and Bragg condition for diffraction, and the formula for defect analysis based on XRD data [19, 20].

2.3.1.1 The equivalence of Bragg law and reciprocal lattice

For three-dimensional (3D) lattice, the lattice is given by a set of vectors R_n of the form $R_n = n_1a_1 + n_2a_2 + n_3a_3$; where a_1, a_2, and a_3 are the lattice vectors, and n_1, n_2, and n_3 are integers. These vectors a_1, a_2, and a_3 define the unit cell. To describe a crystal structure completely, we need to associate a *basis*, consisting of atoms or molecules, with each lattice point. The construction of a 2D crystal from a "*lattice*+*basis*" is illustrated schematically in Fig. 2-5. The position of each atom in the crystal can be written as R_n+r_j , where R_n specifies the origin of the n^{th} unit cell and $\mathbf{r}_j$ denotes the position of the j^{th} atom within the unit cell. The scattering amplitude for a crystal can be factorized into two parts and written as

$$F^{crystal}(q) = \overbrace{\sum_j f_j(q) e^{iq\cdot r_j}}^{unit\ cell\ structure\ factor} \overbrace{\sum_n e^{iq\cdot R_n}}^{lattice\ sum} \qquad (2\text{-}5)$$

The first part is the scattering amplitude from the single unit cell and is know as the structure factor

$$F^{u.c.}(q) = \sum_j f_j(q) e^{iq\cdot r_j} \qquad (2\text{-}6)$$

where f_j denotes the scattering cross section of atom j. It is a linear combinational of atomic form factor f, weighted by the corresponding phase factor $e^{iq\cdot r_j}$ to taken into account the path difference of scattered x-rays. The structure factor is a function of scattering vector.

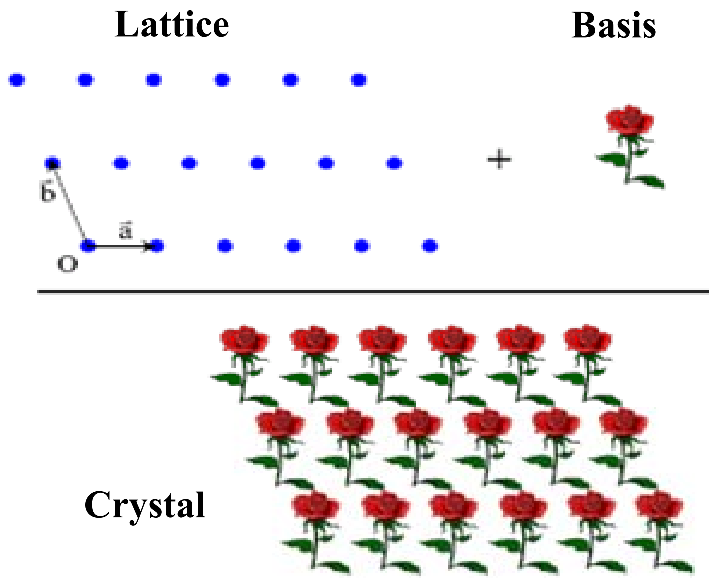

Fig. 2-5 The construction of a 2D crystal structure from '*lattice+basis*".

The second term is the lattice sum to add up the contribution of all the unit cells. The sum of phase factors is negligible except when the phases associated with all the unit cells are different by 2π or its multiple, i.e.

$$q \cdot R_n = 2\pi \times \text{integer} \quad \text{for all } n\text{'s} \tag{2-7}$$

In such a case, all the atoms interfere constructively and the lattice sum will be equal to a huge number. To express the periodic atomic arrangement of a crystal, we can construct a corresponding lattice in the reciprocal space (which has dimensions of reciprocal length) spanned by basis vectors (a_1*, a_2*, a_3*) which fulfill $a_i \cdot a_j^* = 2\pi\delta_{ij}$, where δ_{ij} is the Kronecker delta function which equals to 1 if $i=j$ and is zero otherwise. Similarly, a lattice point in the reciprocal lattice can be specified by $g = ha_1^* + ka_2^* + la_3^*$, where *h, k, l* are all integers. It is now apparent that any reciprocal lattice vector *g* satisfies Eq. (2-7) since the scalar product of *g* and R_n $g \cdot R_n = 2\pi(hn_1 + kn_2 + ln_3)$ is always a multiple of 2π. In other word, only if *q* coincides with a reciprocal lattice vector will the scattered amplitude of a crystallite be non-vanishing. This is known as the Laue condition for X-ray diffraction: $q = g$. To satisfy the requirement of $g \cdot R_n = 2\pi \quad n$, the reciprocal lattice basis vectors can be expressed by

$$a_1^* = \frac{2\pi}{V_c} a_2 \times a_3 \text{ , } a_2^* = \frac{2\pi}{V_c} a_3 \times a_1 \text{ , } a_3^* = \frac{2\pi}{V_c} a_1 \times a_2 \tag{2-8}$$

where $V_c = a_1 \cdot (a_2 \times a_3)$ is the volume of the unit cell. Each point (*hkl*) in the reciprocal lattice corresponds to a set of lattice planes with the miller indices of (*hkl*) in the real space lattice. The direction of the reciprocal lattice vector corresponds to the normal of the real space planes, and the magnitude of the reciprocal lattice vector is equal to 2π times of the reciprocal of the interplanar spacing of the real space planes. The Laue condition can be equivalently expressed by the Bragg's Law. In Fig. 2-6 (a) the proof of this equivalence is illustrated for the case of a 2D square lattice. X-rays are reflected from atomic planes with a spacing of d. The requirement that the path length difference between x-rays reflected by the adjacent planes is a multiple of the wavelength leads to the well-known statement of Bragg's law: $\lambda = 2d\sin\theta$, where θ is the angle between incident x-rays and reflecting planes. Replot the Bragg diffraction condition in reciprocal space using the outgoing wave vector k' and incoming x-ray wave vector k, both of which have magnitude of $2\pi/\lambda$ in the elastic scattering process, and scattering vector $q \equiv k' - k = 2k\sin\theta$, we can obtain the same diffraction condition $q = g$, the Laue condition [19]. The reciprocal lattice in this case is also a square lattice with a lattice spacing of $2\pi/d$ as shown in Fig. 2-6 (b) and the corresponding scattering vector q equals to $g = 2\pi/d$ (01). Hence, each set of parallel planes (hkl) in real space can be expressed by a corresponding reciprocal lattice vector g_{hkl}. The relationship between the reciprocal lattice point and the planes in real space are concluded by two points:

1. g_{hkl} is perpendicular to the planes with Miller indices (hkl).
2. $|g_{hkl}| = 2\pi/d_{hkl}$, where d_{hkl} is the interplanar spacing of the (hkl) planes.

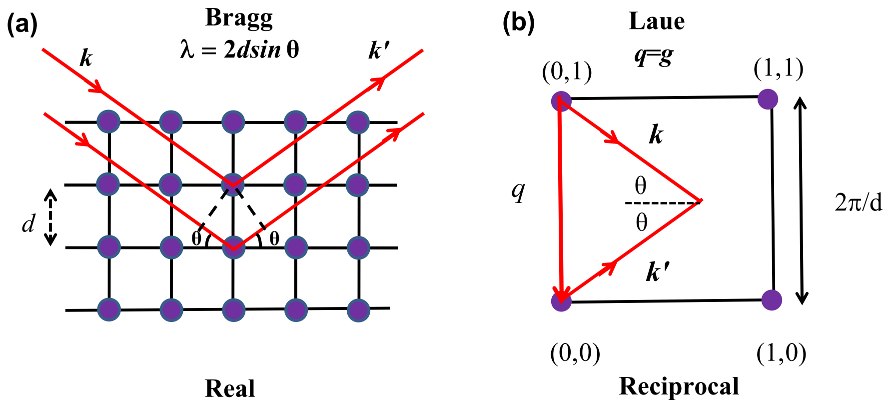

Fig. 2-6 The equivalence of Bragg's Law and the Laue condition for a 2D square lattice

Considering a 3D cubic crystal with lattice parameters a, Fig. 2-7 shows the lattice points in real and corresponding reciprocal space, respectively. As for a hexagonal symmetric crystal, including ZnO studied in this work, with lattice parameters a_0 and c_0 ($a = b = a_0 \neq c_0$, $\alpha = \beta = 90^\circ$, $\gamma = 120^\circ, V_c = \frac{\sqrt{3}}{2} a_0^2 c_0$) we also plot the real and corresponding reciprocal space, as shown in Fig. 2-8.

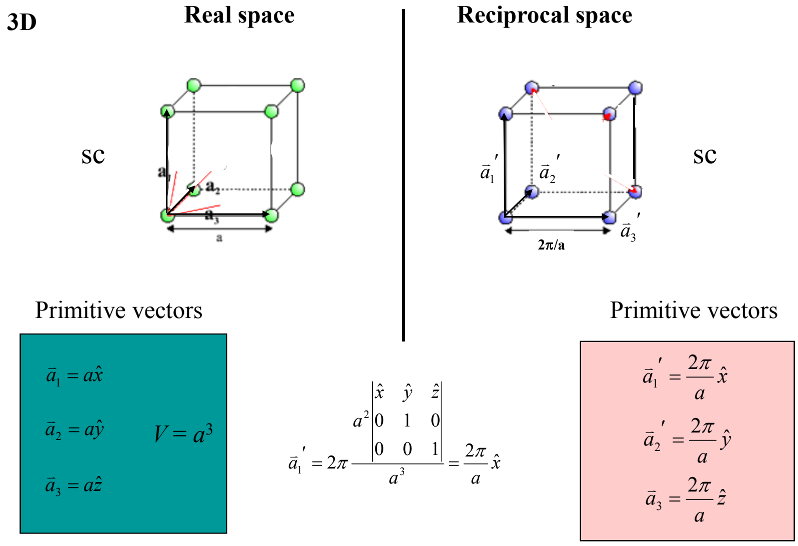

Fig. 2-7 The diagram of direct and the reciprocal lattice of a cubic symmetric crystal.

Hexagonal system

Projection ⊥ z-axis

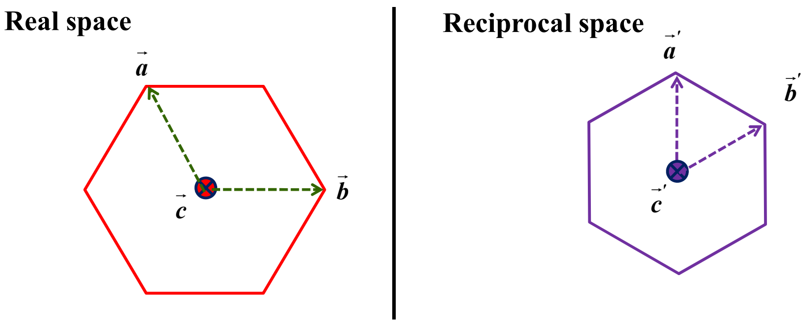

$$a = b = a_0 \neq c$$
$$\alpha = \beta = 90^\circ;\ \gamma = 120^\circ$$

$$\left.\begin{array}{l}\vec{a}' \perp \vec{b},\vec{c}\\ \vec{b}' \perp \vec{a},\vec{c}\end{array}\right\} \gamma' = 60^\circ$$
$$\vec{c}' \parallel \vec{c} \qquad \alpha' = \beta' = 90^\circ$$

$$a' = \frac{bc\sin\alpha}{V_c} = \frac{2}{a_0\sqrt{3}}$$
$$b' = \frac{ac\sin\beta}{V_c} = \frac{2}{a_0\sqrt{3}}$$
$$c' = \frac{ab\sin\gamma}{V_c} = \frac{1}{c_0}$$

Fig. 2-8 The diagram of direct and the reciprocal lattice for a hexagonal symmetric crystal.

Derived from Eq. (2-8) reciprocal lattice vector g_{hkl} of a cubic lattice and g_{hkil} of a hexagonal lattice can be expressed by

$$|g_{hkl}| = \frac{2\pi}{d_{hkl}} = \frac{2\pi}{a}\sqrt{h^2+k^2+l^2} \quad \textit{for cubic lattice}$$

and

$$|g_{(hkil)}| = \frac{2\pi}{d_{(hkil)}} = \pi\sqrt{\frac{4}{3}\left(\frac{h^2+hk+k^2}{a_0^{\,2}}\right)+\frac{l^2}{c_0^{\,2}}} \quad \textit{for hexagona lattice} \qquad (2\text{-}9).$$

Here the (*hkl*) is the three-axis Miller indices. Conventionally, for crystals with hexagonal and rhombohedral symmetry, crystallographic planes are denoted using the four indices based on a four-axis Miller-Bravias coordinate system, consisting of three basal plane axes (a_1, a_2, a_3) at 120° angles to each other and a fourth axis (c) perpendicular to the basal plane. The Miller-Bravias indices (*hkil*) satisfy the conditions $i = -(h+k)$. When using the Miller-Bravias indices one may clearly see the equivalence of the respective directions and planes in the crystal. In this thesis, 4-digit Miller-Bravias indices are used for materials with hexagonal and rhombohedral symmetries including ZnO and sapphire to distinguish them from those with cubic symmetry, e.g. Si, Y_2O_3 and γ-Al_2O_3 where 3-digit Miller indices are employed.

2.3.1.2XRD technique

X-ray diffraction is a well established technique for structure determination of three-dimensional crystals. The diffracted intensity from crystal is collected by proper arrangement of diffractometer to match the Laue condition in sample reciprocal lattice. The four-circle diffractometer utilized consist of four rotatable circles, which are θ, 2θ, χ and ϕ circle; the 2θ circle is the detector axis controlling the magnitude of scattering vector q. The ϕ, χ, and θ circles control the sample orientation. When the q vector coincides with the specific reciprocal lattice vector g, the Laue condition is satisfied. Conceptually, the ϕ angle is equivalent to the azimuthal angle and the χ angle is related to the polar angle of crystal.

[1] Radial scans

Radial scans collect scattered X-ray intensity while the scattering vector q is scanned along the any radial directions in reciprocal space. The most commonly performed radial scan is the one along sample surface normal, which is often known as the θ–2θ or ω−2θ scan as shown in Fig. 2-9. From the positions of diffraction peaks we can determine the corresponding interplanar spacing along the direction of q and the linewidth of the diffraction peak can yield the structural coherence length (grain size) and inhomogeneous strain along the same direction. Similar to the radial scans along surface-normal, radial scans along in-plane and off-normal direction for reciprocal lattice of c-oriented ZnO are shown in (a) (0002) (b) $(10\bar{1}0)$ and (c) $(10\bar{1}2)$ planes of Fig. 2-10, respectively. They can provide the interplanar spacing, structural coherent length along corresponding direction.

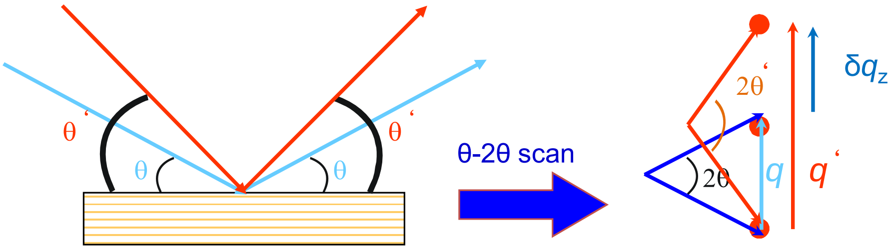

Fig. 2-9 The diagram shows the radial scan along surface normal of XRD and corresponding variation of q vector in reciprocal space.

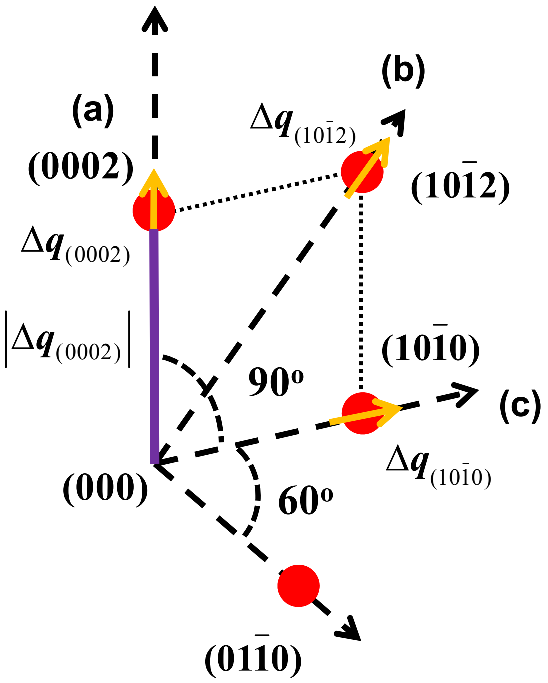

Fig. 2-10 The diagram show the reciprocal lattice for c-oriented ZnO and the radial scans along surface-normal, in-plane and off- normal direction, respectively.

[2] Rocking curve (ω-scan)

For a given incident x-ray direction and detector position, scattered x-ray collected while the crystal is rotated or called rocked through the Bragg angle θ_B. The resulting intensity *vs* the sample angular position θ or equivalently $\omega = \theta - \theta_B$ yields the rocking curve. The width of a rocking curve is a direct measure of the range of orientation distribution, mosaicity, present in the irradiated area of the sample because each subgrain of a typical mosaic crystal successively comes into reflecting position as the crystal is rocked, as shown in Fig. 2-11(a). Rocking curve performed at reflections along surface-normal is sensitive the tilt (polar) angle distribution of the sample; on the other hand the rocking curved measured at surface Bragg peaks mainly reflect the twist (azimuthal) angle distribution of the sample, because the variation of scattering vector Δq is perpendicular to the radial direction of corresponding reflections, as shown in Fig. 2-11(b).

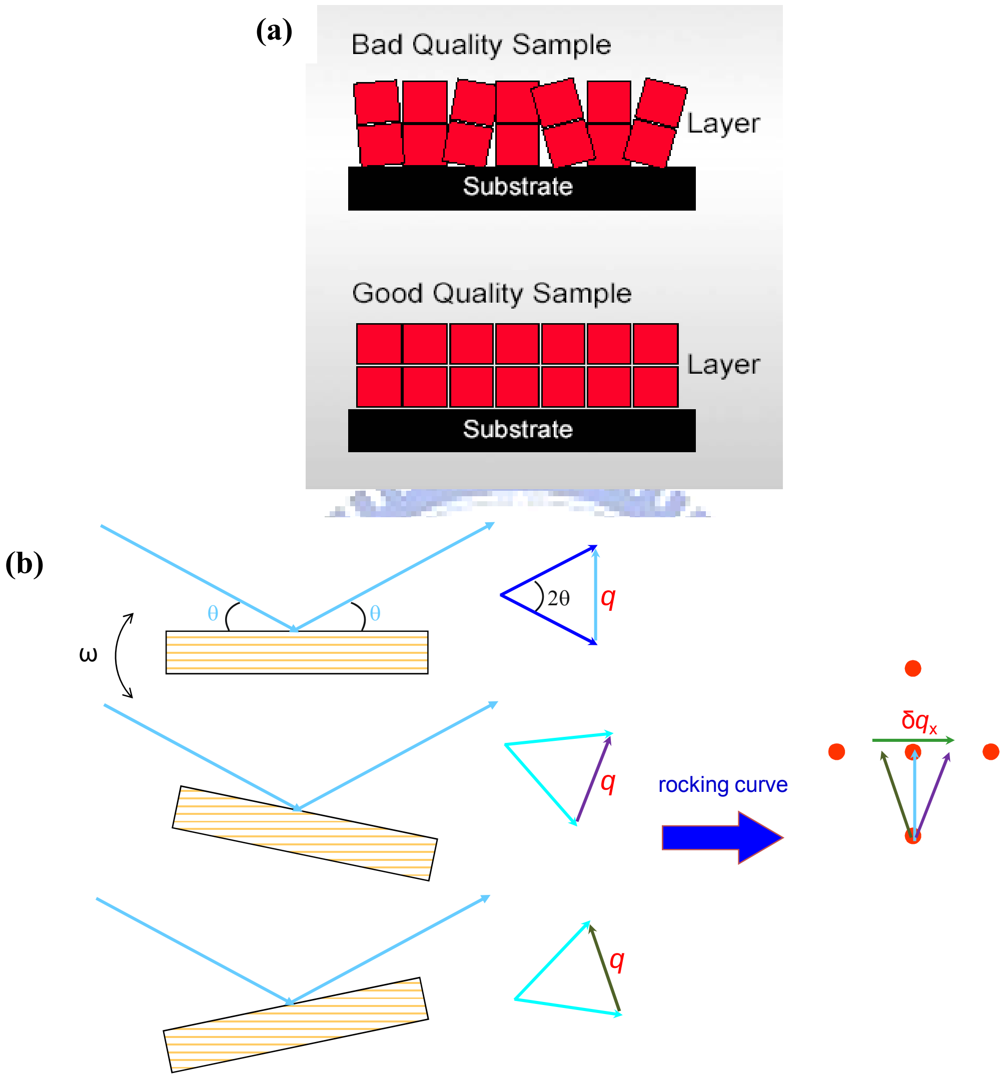

Fig. 2-11 The diagrams show the orientation distribution of subgrains of a typical mosaic crystal (a) and the rocking curve of XRD and corresponding variation of q vector (b).

[3] Azimuthal scan

Azimuthal scan means measuring the diffraction intensity as a function of azimuthal angle ϕ by rotating the sample along an axis which is usually parallel to surface normal or, in some cases, to a specific crystallographic axis. Figure 2-12 illustrates schematically the reciprocal lattice of a c-oriented ZnO film. Using azimuthal scan, we can study the symmetry and crystal quality of the grown film and determine its relative orientation with substrate in epitaxy.

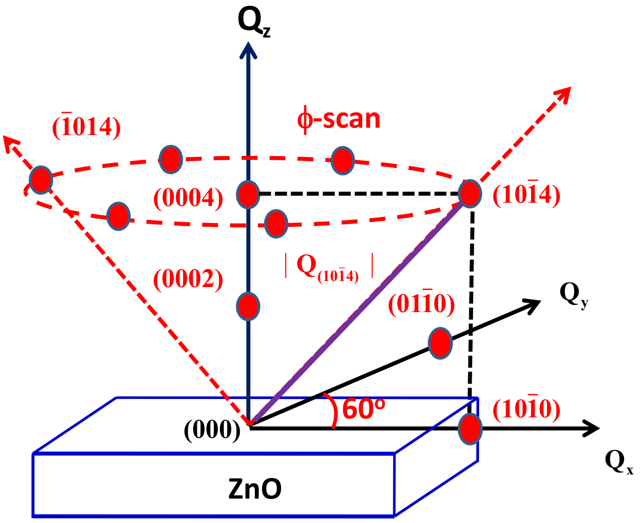

Fig. 2-12 The diagram show azimuthal scan across the off-normal ZnO $(10\bar{1}4)$ peak.

2.3.1.3 Threading dislocation distortion for XRD analysis

The presence of TDs in materials gives rise to crystalline plane distortion [21]. Depending on the geometry of TDs, lattice is deformed in a different way. Have a thin film with hexagonal wurtzite crystalline symmetry and c-plane normal orientation as an example. Pure screw TDs along [0001] direction generate a pure shear strain field, where (*hkil*) crystalline planes with nonzero *l* are deformed. The width of (000*l*) rocking curve and radical scan are only sensitive to the screw TDs in the films. Therefore, the width of (000*l*) diffraction peaks is investigated to determine the strain field induced by screw TDs. The density of the screw dislocations N_S can be obtained using the following equation [22, 23]

$$N_s = \frac{\alpha_\Omega^2}{4.35 b_c^2} \qquad (2\text{-}10)$$

where b_c is the Burgers vector of screw TDs and α_Ω is the tilting angle. From the radial-scan line width of (000*l*) reflections, the inhomogeneous strain ε_S can be obtained. Considering that each dislocation is accompanied by a strain field, it is possible to calculate the dislocation density from the strain induced broadening of Bragg reflections in the radial direction β_ε using the following equations provided that the slip planes and Burgers vectors of the dislocations are known [24].

$$\beta_\varepsilon^2 = 8(\ln 2)\left\langle \varepsilon_S^2 \right\rangle \tan^2\theta \qquad (2\text{-}11)$$

$<\varepsilon_S^2>$ is the mean square strain and can be calculated for a pure screw dislocation by [24, 25]

$$\left\langle \varepsilon_S^2 \right\rangle = \frac{b_s^2}{4\pi^2 r_s^2} \ln\left(\frac{r_s}{r_0}\right) \sin^2 \Psi_s \qquad (2\text{-}12)$$

Ψ_s is the angle between the Burgers vector b_s and the normal of the diffracting lattice plane and r_S and r_0 denote the upper and lower integration limits of the strain field, respectively. For r_0, a value of 10^{-7} cm is assumed and r_s is related to the screw dislocation density N_s by

$$r_s = \left(\frac{1}{4N_s}\right)^{1/2} \qquad (2\text{-}13)$$

On the other hand, pure edge TDs with dislocation line along [0001] direction and Burgers vector $b_E = \frac{1}{3} < 11\bar{2}0 >$ cause an azimuthal rotation of crystallites around the surface normal, consequently, the crystalline planes (*hkil)* with $l = 0$ are twisted. The presence of pure edge TDs not only influences the width of rocking curve but also that of radical scan of (*hki0*) reflections. The twist angle α_ϕ can be measured by performing ϕ-scans. Using measured broadening β_ϕ of the ϕ–scans, the dislocation density N_E can be calculated from following equation when the broadening due to small correlation lengths |L| can be neglected, i.e. $\beta_\phi = \alpha_\phi$ [22, 23]

$$N_E = \frac{\alpha_\phi^2}{4.35 b_E^2} \qquad (2\text{-}14)$$

where b_E is the Burgers vector of the edge dislocations. (In the case of ZnO, $|b_E| = a_0 =$ 0.3238 nm.) This equation holds only for a strictly random distribution of dislocations.

If dislocations are piled up in small angle grain boundaries, the following formula should be used,

$$N_E^{'} = \frac{\alpha_\phi^{'}}{2.1 |b_E||L|} \qquad (2\text{-}15)$$

where $|L|$ is the average size of subgrains and $\alpha_E^{'}$ is again the twist angle. For a system with both dislocation distributions (randomly and piled up), as observed in the ZnO sample, the real dislocation density will fall between these two values. For the calculation of the mean square strain of edge dislocations $<\varepsilon_E^2>$, the following equation is adapted:

$$\left\langle \varepsilon_E^2 \right\rangle = \frac{5b_E^2}{64\pi^2 r_E^2}\ln\left(\frac{r_E}{r_0}\right) f\left(\Delta, \Psi_E\right),\ where\ f\left(\Delta, \Psi_E\right) = \left(2.45\cos^2\Delta + 0.45\cos^2\Psi_E\right) \qquad (2\text{-}16)$$

where Ψ_E is again the angle between the Burgers vector and the diffraction plane normal and Δ is the angle between the normal of the slip plane and the normal of the diffracting plane. The edge dislocation density N_E is related to r_E, the outer limit of strain filed caused by edge dislocations, by:

$$r_E = \left(\frac{1}{4N_E}\right)^{1/2} \qquad (2\text{-}17)$$

As a cross examination, the line width broadening of an off-normal reflection which is sensitive to both screw and edge types of TDs is usually examined. Reflection $(10\bar{1}4)$ is a proper choice. Because there are three distinct dislocation systems for pure edge dislocations in ZnO, i.e. $b_E = \frac{1}{3}[11\bar{2}0]$, $\frac{1}{3}[\bar{2}110]$, and $\frac{1}{3}[1\bar{2}10]$, the mean square strain $< \varepsilon_E^2 >$ is influenced by all three possible orientations. In table 2-2, the angles Ψ_E and Δ as well as the corresponding values of $f\ (\Delta, \Psi_E)$ are listed for the three individual slip systems $\{1010\}$ for diffraction vector $(10\bar{1}4)$. From Eq. (2-16) it is clear that pure edge threading dislocations with $b_E = \frac{1}{3} < 11\bar{2}0 >$ do not influence the (000*l*) reflections of ZnO since the angles Ψ_E and Δ are both 90°. In order to calculate the mean square strain due to screw and edge dislocations, the individual square strains are summed up as follows:

$$\beta_\varepsilon^2 = 8\left(\ln 2\right)\left(\left\langle \varepsilon_S^2 \right\rangle + \left\langle \varepsilon_E^2 \right\rangle\right)\tan^2\theta \qquad (2\text{-}18)$$

Using Eqs. (2-10) ~ (2-18), the strain broadening of $(10\bar{1}4)$ reflections can be simulated for different densities of screw and edge dislocations and then compared with the measured values.

Table 2-2. The values of Δ, Ψ_E, and $f(\Delta, \Psi_E)$ for the three edge dislocation systems in ZnO with $b_E = \frac{1}{3} < 11\bar{2}0 >$ and slip planes $\{1\bar{1}00\}$ for $(10\bar{1}4)$ reflection.

Slip plane	Δ (deg.)	Ψ_E (deg.)	$f(\Delta, \Psi_E)$
$(0\bar{1}10)$	102.19	68.55	0.1694
$(10\bar{1}0)$	65.02	90	0.4369
$(1\bar{1}00)$	102.19	111.45	0.1694

2.3.1.4 XRD line width analysis

The particle size and lattice distortion can be obtained, in principle, by XRD line profile analysis [26, 27]. The kinematic theory of X-ray scattering shows that the influence of particle size and lattice distortion to the diffraction peak line width broadening are diffraction order independent and dependent, respectively, enabling the separation of the two effects. Williamson-Hall (W-H) method, which essentially combines the Scherrer equation for grain size determination with an expression for the strain induced broadening obtained by differentiating the Bragg's law, is one of the most commonly used method to decouple the two contributions [28]. The most popular expression used for W-H analysis is

$$\Delta q = \Delta q_{size} + \Delta q_{strain} = \frac{2\pi}{L} + q\varepsilon \qquad (2\text{-}19)$$

where L and ε represent the coherent length and inhomogeneous strain, respectively. Thus, the inverse of ordinate intercept of a W-H plot yields the coherence length (L), i.e., the effective domain size, and the slope yields the root-mean-square (RMS) inhomogeneous strain (ε) averaged over the effective domains.

2.3.2 Transmission electron microscope (TEM) [29]

TEM has become one of the premier tools for micro-structural characterization of materials. In practice, the diffraction patterns measured by x-ray methods are more quantitative and have better resolution than electron diffraction patterns, but electrons have an important advantage over x-ray: electrons can be easily focused to s small spot size [23]. Therefore, TEM is a powerful technique for studying defects in great details. The section below is a brief description of TEM technique.

2.3.2.1 Selected area electron diffraction (SAED)

Due to the wave-particle duality, electron beam can be considered as wave and is subjected to diffraction from periodic arrangement of scatters with proper length scale. A crystal can thus act as a diffraction grating to electrons. Because the strong interactions between electrons and materials, the TEM specimen has to be thinning to 50 ~100 nm to allow electrons to transmit. SAED is the electron diffraction pattern taken from a selected area of the sample and can be described as the first Fourier transformation of atoms arranged periodically. By tilting the specimen relative to the electron beam, we can choose the optimal geometry to satisfy the Bragg law for a specific reciprocal lattice vector *g* or a group of *g's*.

2.3.2.2 Threading dislocation density analysis

TEM image is the second (inverse) Fourier transformation of SAED by electromagnetic lens. The imaging mode is often done by utilizing the primary beam (bright field mode) or any diffracted beam for imaging (dark field mode). To obtain the best contrast for TDs analysis, the "two-beam" case with only one "reflex" excited; i.e. the Bragg condition is only met for one diffraction vector *g*, is preferred.

Dislocations are invisible or exhibit only weak contrast if $g{\cdot}b = 0$. This can be used for Burgers vector analysis by imaging the same dislocation with different diffraction vectors and observing the contrast, as shown in Fig. 2-13. The dislocation density can be obtained by

$$D = \frac{n}{lh} \tag{2-20}$$

where n is obtained by counting the number n of dislocations, l is the length of the observation region and h is specimen thickness in cross sectional TEM. The number of dislocations and specimen length can be measured from the TEM image; however, the specimen thickness has to be derived from thickness fringe in TEM image.

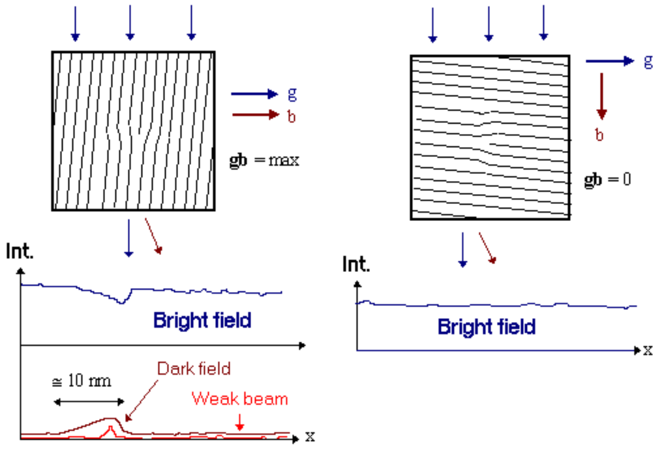

Fig. 2-13 The picture illustrates imaging conditions for dislocations with the maximum and minimum of *gb* product.

2.3.3 Scanning probe microscopy (SPM)

The scanning probe microscope (SPM) is an imaging tool with a vast dynamic range, covering from the micron all the way down to the atomic level. Two fundamental components of SPM are the scanner and the probe. The scanner precisely controls the position of the probe relative to surface, both vertically and laterally. The probe is the point of interface between the SPM and the sample. Depending of the design of the probe, various qualities of the surface are measured. SPM has been employed to characterize surface topography, the local electrical properties, such as capacitance, resistance, electrical field gradient, and so on in semiconductor materials. Scanning capacitance microscopy (SCM) and conductive atomic force microscopy (C-AFM) are applied in this work to measure the distribution of dislocations near the surface.

2.3.3.1 Theory of SCM [30-32]

SCM images two-dimensional majority electrical carrier distribution in semiconductor devices and materials by measuring small capacitance variations with high spatial resolution. While scanning in contact mode, the capacitance value is monitored using a high frequency resonant circuit through the metal-insulator-semiconductor (MIS) capacitor structure formed by the probing tip and sample. By maintaining a constant force between tip and sample, simultaneous topographic and capacitive images are generated. Selectable AC and DC biases are applied between the sample and the conductive tip and an ultra high frequency resonant capacitance sensor is the detection system, as shown Fig. 2-14. When the resonating probe tip is put in contact with a semiconductor, the sensor, probe and sample all become part of the resonator. Small changes in the amplitude of applied AC signal create enormous changes in the amplitude of capacitive response. It has been demonstrated that this kind of setup can be sensitive to variations as small as attofarads (10^{-18} farads).

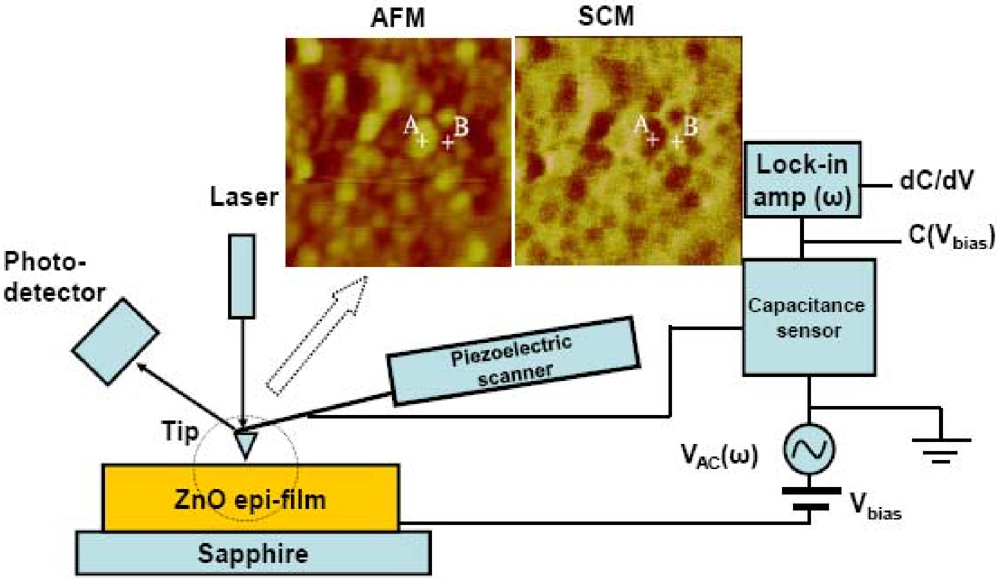

Fig. 2-14 Scanning capacitance microscopy block diagram.

SCM induces the desired capacitance variations in the sample near the tip by applying an electric field between the scanning contact AFM tip and sample. This is done using a kilohertz AC bias voltage applied to the semiconductor. The free carriers beneath the tip are alternately attracted and repulsed by the tip due to the alternating electric field. The alternating accumulation and depletion of carriers under the tip may be modeled as a moving capacitor plate, as shown in Fig. 2-15.

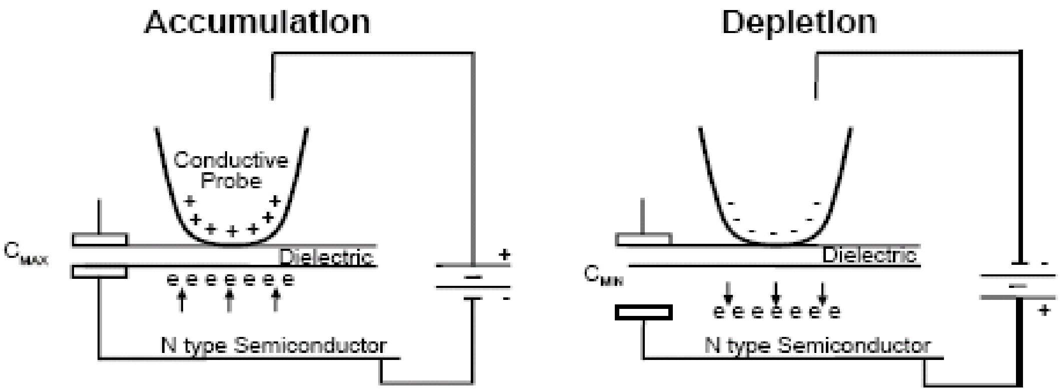

Fig. 2-15 Change from accumulation to depletion due to alternating electric field of SCM.

The depth of depletion and hence capacitor plate movement is determined by three quantities: [1] the strength of the applied field; [2] the quality and thickness of the dielectric (usually an oxide) between the conductive probe and the semiconductor; and, [3] the free carrier concentration.

Figure 2-16 shows a typical high frequency capacitance-verses-voltage (C-V) curve for *n*-type semiconductors with high and low doping concentration. As positive voltage is applied to the conductive probe; the electrons are attracted to the surface and accumulate there. As the voltage on the probe is swung negative, electrons move away from the probe (depletion) which increases the spacing between the probing tip and equivalent moving capacitor plate in semiconductor and lowers the capacitance. A material with the lower carrier concentration is depleted faster and hence the capacitance decreases faster with voltage. Therefore, the slope of the C-V curve, i.e. dC/dV, is larger for the material with lower carrier concentration. The SCM is probing the slope of C-V curve.

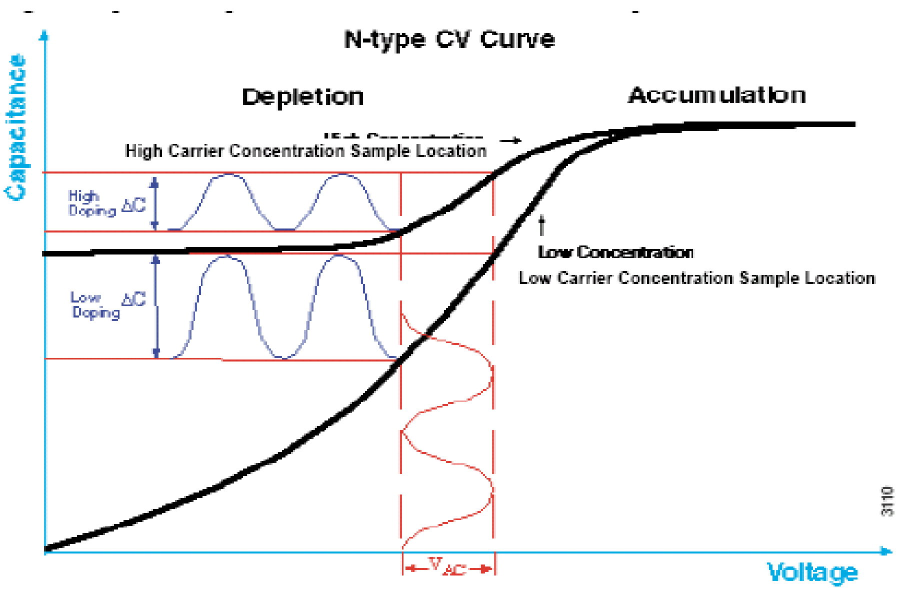

Fig. 2-16 Capacitance versus applied AC voltage (C-V) curves for n-type semiconductor with different carrier concentration.

2.3.3.2 Theory of CAFM [33]

Conductive Atomic Force Microscopy (C-AFM) characterizes conductivity variations across surface of medium- to low-conducting and semiconducting materials with the same high lateral resolution as AFM. With the tip at virtual ground, a selectable DC bias voltage is applied between the conductive tip and sample (see Fig. 2-17). C-AFM probes the current passing through the tip and sample within the range from 1 pA to 1 μA. By maintaining a constant force between tip and sample, simultaneous topographic and current images are recorded, enabling the establishment of a direct correlation of local topography to electrical properties.

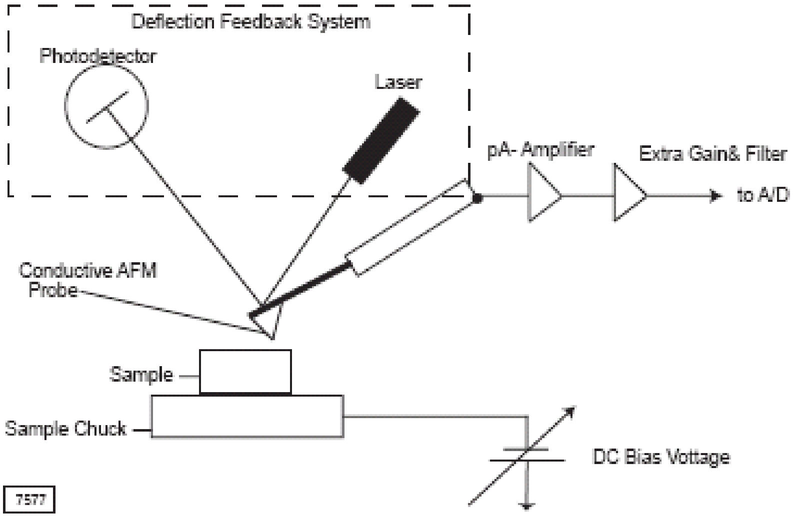

Fig. 2-17 Conductive AFM block diagram.

2.3.4 Photoluminescence characterization

Photoluminescence (PL) is a process in which a substance absorbs photons and then re-radiates photons. In quantum mechanics, this can be described as an excitation to a higher energy state and then a return to a lower energy state accompanied by the emission of a photon. The energy of the emitted photons is thus related to the difference in energy levels between the two electronic states involved in the transition between the excited state and the equilibrium state. Available electronic states and allowed transitions between states are determined by the rules of quantum mechanics. PL is a nondestructive method of probing the electronic structure of materials and has become an important technique for the semiconductor industry owing to its powerful and sensitive ability to characterize impurities and defects in semiconductors, which affect material quality and device performance.

The characteristic features in the PL spectrum of ZnO and their origins are reviewed in the following.

2.3.4.1 General concepts [34, 35]

PL emission requires that the system be in a nonequilibrium condition and photo-excitation is adapted to produce the hole-electron pairs in semiconductors. The electronic ground state of a perfect semiconductor consists of completely filled valance band and completely empty conduction band. We can define this state as the "zero" energy or "vacuum" state. If we start from the above-defined ground state and excite one electron to the conduction band, we simultaneously create a hole in the valance band. In this sense, an optical excitation is considered as a two-particle transition. The same argument holds for the recombination process. An electron in the conduction band can return radiatively or nonradiatively back to the valance band only if there is a free space, i.e., a hole, available there. Two quasi-particles annihilate in the recombination process. The optical properties of a semiconductor can thus be described in terms of the excited states of a N-particle problem. The quanta of these excitations are called excitons, which are further classified to be Frenkel excitons and Wannier excitons according to the spatial distribution of their associated wavefucntions. In insulators like NaCl or organic crystals such as anthracene, excitons exist with the electron-hole pair wavefunctions confined to one unit cell. These so-called Frenkel excitons cannot be described in the effective mass approximation. For Wannier excitons, their Bohr radii, defined as the mean distance between electron and hole, are larger compared to the lattice constant. This condition is met in most II-VI, III-V, and column IV semiconductors. Thus, we will focus on the Wannier excitons in this work.

Based on the effective mass approximation, the system of an electron-hole pair can be treated as a hydrogen-like problem with Coulomb potential $\frac{-e^2}{4\pi\varepsilon_0\varepsilon\left|r_e - r_h\right|}$. Excitons in semiconductors form, to a good approximation, a hydrogen- or positronium-like series of states below the gap. For a simple parabolic band in a direct-gap semiconductor one can separate the relative motion of electron and hole and the motion of the center of mass. This leads to the dispersion relation of exciton as shown in Fig. 2-18

$$E_{ex}(n_B, K) = Eg - Ry^* \frac{1}{n_B^2} + \frac{\hbar^2 K^2}{2M} \tag{2-21}$$

where $n_B = 1, 2, 3\ldots$ is the principal quantum number, $Ry^* = 13.6\frac{\mu}{m_0}\frac{1}{\varepsilon^2}$ is the exciton binding energy, $M = m_e + m_h$, and $K = k_e + k_h$ are translational mass and wave vector of the exciton, respectively.

In following sections, a brief review on the characteristic features in a typical low temperature PL spectrum, including intrinsic excitonic properties, donor- and acceptor-bound excitons, two-electron satellites, and longitudinal optical (LO)-phonon replicas is given. Then, the donor-acceptor-pair (DAP) transition, green, yellow, and orange defect emissions are also discussed.

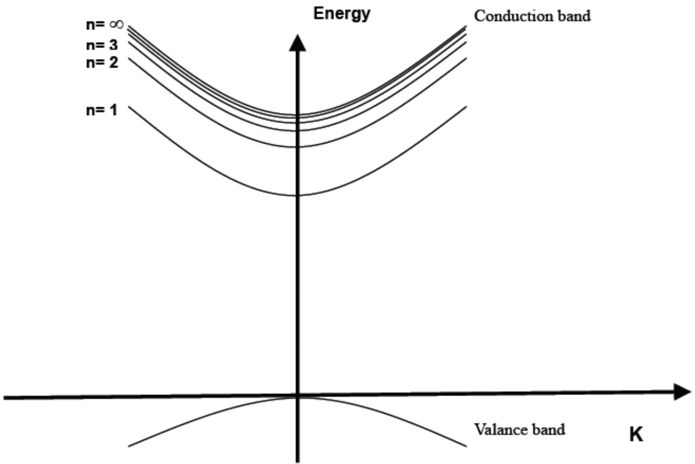

Fig. 2-18 The exciton dispersion in a two-particle (electron-hole) excitation diagram of the entire crystal. The crystal ground state (zero energy and zero momentum) is the point at the origin. Different parabolas represent the kinetic energy bands associated with different terms of the excitonic series. [34]

2.3.4.2 Free excitons [35, 36]

The optical properties of a semiconductor are connected with both intrinsic and extrinsic effects. The intrinsic excitonic features are typically in the 3.376–3.450 eV range. The wurtzite ZnO conduction band is mainly constructed from the *s*-like state having (Γ_7^c) symmetry, whereas the valence band is a *p*-like state, which is split into three bands due to the influence of crystal field and spin-orbit interactions. The ordering of the crystal-field and spin-orbit coupling split states of the valence-band maximum in wurtzite ZnO was calculated by our group using tight-binding theory. The obtained electronic band structure of wurtzite ZnO is shown in Fig. 2-19. The valence-band symmetry ordering (A-Γ_9, B-Γ_7, and C-Γ_7) in ZnO is consistent with that observed in low temperature PL and magnetoluminescence measurements by other researchers [37-39].

According to the group theory, the direct product of the group representations of the band symmetries (Γ_7 the conduction band, Γ_9 for the A valence band, Γ_7 upper for the B valence band, and lower Γ_7 for the C valence band) yields the following intrinsic exciton ground state symmetries:

$$\Gamma_7 \times \Gamma_9 \rightarrow \Gamma_5 + \Gamma_6 \text{ , } \Gamma_7 \times \Gamma_7 \rightarrow \Gamma_5 + \Gamma_1 + \Gamma_2$$

The Γ_5 and Γ_6 exciton ground states are both doubly degenerate, whereas Γ_1 and Γ_2 are both singly degenerate. Γ_5 and Γ_1 are allowed transitions with $\mathbf{E} \perp \mathbf{c}$ and $\mathbf{E} \| \mathbf{c}$, respectively, where **E** is electric field of incident light and **c** denotes the crystallographic c-axis, but the Γ_6 and Γ_2 are forbidden.

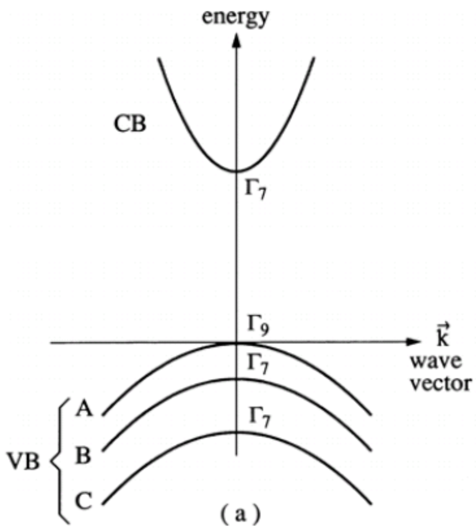

Fig. 2-19 Details of the band structure of hexagonal semiconductors around the *Γ* point.

Figure 2-20 displays the PL spectrum in the fundamental excitonic region measured at 10 K in the **E**⊥**c** polarization geometry for a high quality ZnO crystal. The A-free exciton and its first excited state emission are observed at $FX_A^{n=1}$ = 3.3771 eV and $FX_A^{n=2}$ = 3.4220 eV for Γ_5 band symmetry, respectively. The A-free exciton and associated first excited state emission for Γ_6 band symmetry are also observed at $FX_A^{n=1}$ = 3.3757 eV and $FX_A^{n=2}$ = 3.4202 eV. Although Γ_6 exciton emissions should be forbidden at k = 0 in the adapted experimental polarization condition, they are still observed. This could be due to the finite momentum of the photons. Geometrical effects such as not having the sample orientation exactly perpendicular to the electric field may be another reason for observing Γ_6 transition. According to the energy separation between the ground state and the excited state peak positions, the exciton binding energy and band gap energy can be derived. The energy difference of about 45 meV gives A-free exciton binding energy of 60 meV and corresponding band gap energy of 3.4371 eV at 10 K. Based on the reported energy separation of the A- and B-free excitons（in the range of 9–15 meV）, we assigned the weak emission centered at 3.3898 eV, which is about 12.7 meV apart from the A exciton, to the B exciton transition.

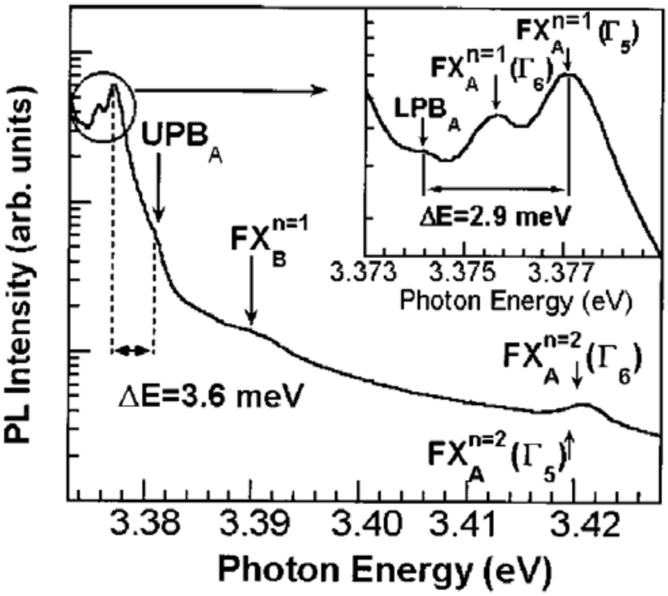

Fig. 2-20 Free excitonic fine structure region of the 10 K PL spectrum of a ZnO single crystal. [36]

2.3.4.3 Bound excitons [36]

A real crystal is never perfect. Imperfections such as ion vacancies, interstitials, or substitutional atoms (either native or intentionally introduced) exist with a density n_i less than 10^{12} cm^{-3} in ultrapure crystals. Extrinsic optical properties of ZnO as well as other semiconductors are closely related to dopants and structural defects, which usually create discrete electronic states in the band gap and therefore influence both optical absorption and emission processes. Furthermore, the imperfections can attract excitons that become localized at the defect sites to form bound excitons. The binding energy of the exciton to the defect is often quite small, typically a few meV. Therefore, the bound excitons are best observed at very low temperatures. Excitons could be bound to neutral or charged donors and acceptors. A basic assumption in the description of the bound exciton states for neutral donors and acceptors is a dominant coupling of the like particles in the bound exciton states. These two classes of bound excitons are by far the most important cases for direct band gap materials. In high quality bulk ZnO, the neutral shallow donor-bound exciton（DBE） often dominates because of the presence of donors due to unintentional impurities and/or shallow donor-like defects. In samples containing acceptors, the acceptor-bound exciton (ABE) is observed. The recombination of bound excitons typically gives rise to sharp lines with the photon energy characteristic of the corresponding defect. The low-temperature PL spectra are dominated by several bound excitons in the range from 3.348 to 3.374 eV for bulk ZnO sample, as seen in Fig. 2-21. The prominent lines located at 3.3598 ($D_1^0 X_A$), 3.3605 ($D_2^0 X_A$), 3.3618 ($D_3^0 X_A$), 3.3650 ($D_4^0 X_A$), and 33664 ($D_5^0 X_A$) eV are the A excitons bound to neutral donors. Based on the energy separation between the $FX_A^{n=1}(\Gamma_5)$ and the DBE peaks, the binding energies of the DBEs associated with different donors, in the range of 10 to 20 meV, can be derived.

On the high-energy side of the neutral DBE, transitions between 3.3664 and 3.3724 eV have been attributed to the excited states or excited rotator states of the neutral-donor-bound excitons. These excited states are analogous to the rotational states of the H molecule. In Fig. 2-21 we also saw the relatively strong emission line at 3.3724 eV ($D_2^0 X_B$) that is attributed to the transition due to the B-free exciton bound to the same main neutral donor. The energy separation between this peak and the main peak at 3.3605 eV ($D_2^0 X_A$) is about 12 meV, which is consistent with the energy splitting of the A- and B- free exciton lines. In the lower energy part of the PL spectrum, ABEs at 3.3564 ($A_1^0 X_A$), 3.353($A_2^0 X_A$), and 3.3481 eV ($A_3^0 X_A$) are also observed. However, relative peak intensities of the particular donor-related exciton lines show some differences from sample to sample. This is because the concentration of the particular donor could vary from sample to sample as well as its capture cross section.

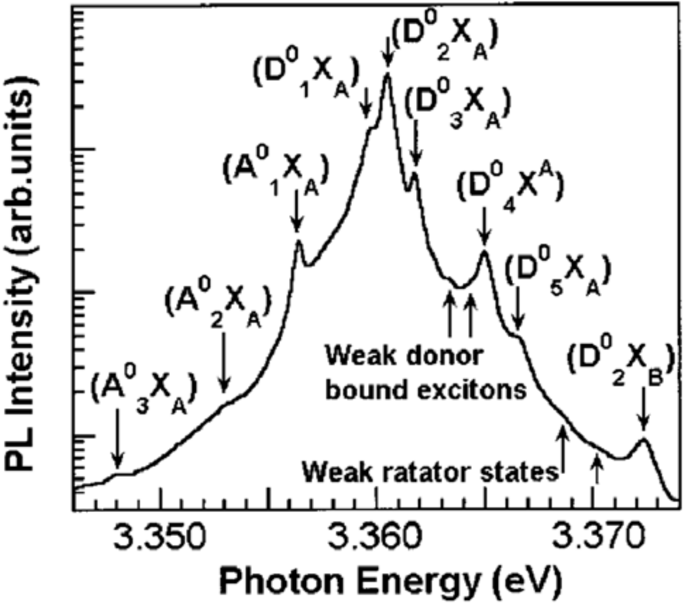

Fig. 2-21 Bound excitonic region of the 10 K PL spectrum of a ZnO single crystal. [36]

2.3.4.4 Two-electron satellites [36]

Another characteristic of the neutral-donor-bound exciton transition is the two-electron satellite（TES）transitions in the spectral region of 3.32–3.34 eV.

These transitions involve radiative recombination of an exciton bound to a neutral donor, leaving the donor in the excited state. In the effective mass approximation, the energy difference between the ground-state neutral DBEs and their excited states（TES）can be used to determine the donor binding energies（the donor excitation energy from the ground state to the first excited state equals to 3/4 of the donor binding energy, E_D）and catalog the different species present in the material. The spectral region for the expected two-electron satellite transitions is shown in Fig. 2-22 for ZnO single crystal. The main peak at 3.3224 eV $(D_2^0X_A)_{2e}$ is the excited state associated with the most intense neutral DBE at 3.3605 eV ($D_2^0X_A$). The shoulder located at about 3.3268 eV $(D_3^0X_A)_{2e}$ on the high-energy side of the main TES peak is related to the excited state of the donor whose ground state emission is at 3.3618 eV ($D_3^0X_A$). A weak emission at 3.3364 eV $(D_4^0X_A)_{2e}$ is also attributed to the TES transition of the neutral donor whose ground state is at 3.3650 eV ($D_4^0X_A$). From the separation of the ground state and the corresponding excited states, we were able to calculate the donor binding energies as 51 meV for the donor at 3.3605 eV, 47 meV for the donor at 3.3618, and 38 meV for the donor at 3.365 eV.

From the separation between the A-free exciton and the ground-state neutral DBEs, we can also determine the binding energies of these excitons as 16.5 meV（for 3.3605 eV）, 15.3 meV（for 3.3618 eV）, and 12.1 meV（for 3.3560 eV）. According to the empirical Haynes rule, the binding or localization energy of the DBEs is proportional to the binding energy of the corresponding donor. Indeed, this relation is clearly seen in the inset of Fig. 2-22. Besides, there are two additional peaks at 3.332 and 3.313 eV on both sides of the main TES lines; they may be related to the excitons bound to structural defects but their origins is not identified at this point.

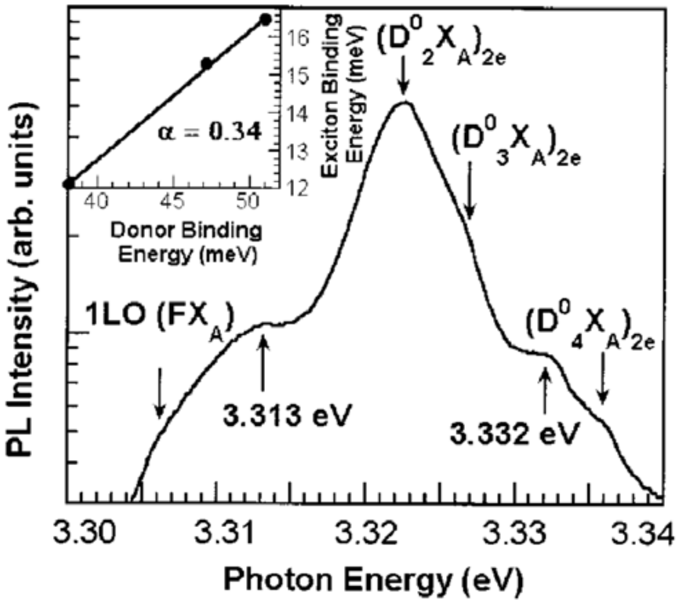

Fig. 2-22 10K PL spectrum in the TES region of the main bound exctions line.[36]

2.3.4.5 LO-phonon replicas [36]

The intensive exciton–LO phonon interaction may induce phonon-assisted exciton emissions accompanying the exciton recombination. As indicated in Fig. 2-23, the bump labeled by 1LO (FX_A) at approximate 3.306 eV matches the expected value for the 1LO-phonon replica of the free exciton peak (about 71 meV apart from the $FX_A^{n=1}$ free-exciton peak). Although the signals are weak, the second and third order LO phonon replicas labeled as 2LO (FX_A) and 3LO (FX_A), respectively, are also observed in the PL spectrum, as marked by upward arrows. It is noted that LO-phonon replicas occur with a separation of 71-73 meV, which corresponds to the LO-phonon energy in ZnO.

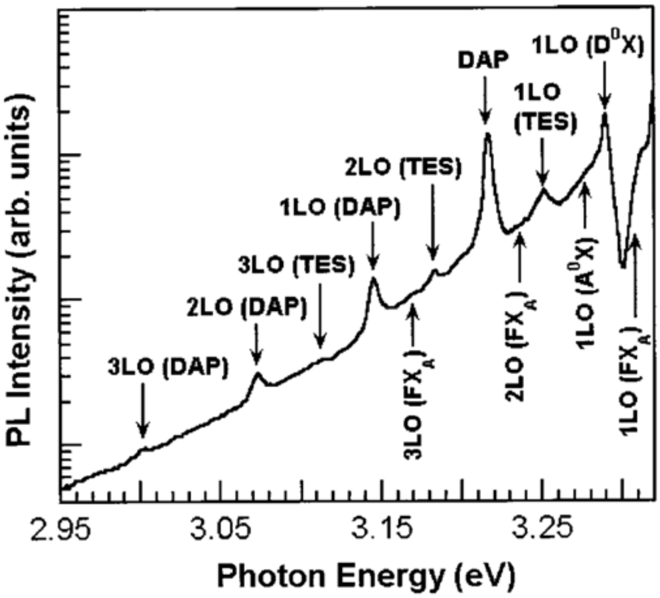

Fig. 2-23 10K PL spectrum in the region where DAP transition and LO-phonon replicas are expected to appear. [36]

The peak at 3.2898 is the first LO-phonon replica of both 3.3618 and 3.3605 eV lines, whereas the first LO-phonon replica of 3.3650 eV line appears as a shoulder on the high energy side of this intense peak. Resolving the second and higher order LO replicas is even harder because the energy position (3.218–3.223 eV) falls in the spectral region where the donor-acceptor-pair (DAP) transition and its LO phonon replicas are expected to appear (will be described in the following section). In fact, the radiative recombination peak at 3.217 eV is attributed to the DAP; its first, second, and third LO-phonon replicas also show up at 3.145, 3.073, and 3.001 eV, respectively, in Fig. 2-23 Two closely spaced peaks at 3.2898 and 3.2920 eV can be barely resolved. They are about 72 meV below the main neutral DBE lines at 3.3605 and 3.3650 eV and assigned as the first LO-phonon replicas of the corresponding DBEs. The LO-phonon replicas are expected to be roughly two orders of magnitude less intense than the neutral DBE lines due to the weak coupling between donor-related bound exciton lines and optical phonons. The relatively broad peak around 3.280 eV is the first LO-phonon replica associated with the most intense ABE line (3.3564 eV). This is marked by 1LO ($A^o X$) in Fig. 2-23. Finally, first, second, and third order LO-phonon replicas of the TES lines are also clearly observed in the PL spectra. These peaks are labeled as 1LO, 2LO, and 3LO-TES and they are positioned at 3.252 3.182, and 3.112, respectively.

2.3.4.6 Defect emission [40, 41]

Besides exciton-related emissions in the photon energy range of 3.25–3.4 eV, PL spectrum of ZnO usually contains a sharp peak at about 3.22 eV followed by at least two LO-phonon replicas. This emission has been attributed to the DAP transitions involving a shallow donor and a shallow acceptor. This conclusion is based mostly on a characteristic transformation of the DAP emission lines to similar, but shifted, emission lines arising from the transitions from the conduction band to the same shallow acceptor (*e-A* transitions) with increasing temperature. The DAP line is quenched and gives way to the *e-A* line at elevated temperatures due to thermal ionization of the shallow donors. From the position of the *e-A* and DAP lines, the ionization energy of the unintentional doped shallow acceptor in ZnO can be estimated.

In addition to UV excitonic emission lines, ZnO commonly exhibits luminescence in the visible spectral range with dissimilar emission wavelengths due to intrinsic or extrinsic defects. The origin of these emissions, including three different types of defects (green at ~2.3 eV, yellow at ~2.1 eV, and red at ~1.8 eV), has been controversial, especially the green emission. Assignment of various defect emissions to the specific transitions in ZnO is often complicated by the presence of multiple emissions and broad emission peaks containing contributions from multiple transitions. Different fabrication conditions (pressure, temperature, flow rate, etc.) resulted in different defect types and concentrations resulting in different luminescence spectra.

A number of hypotheses have been proposed to explain the green emission, such as transition between singly ionized oxygen vacancy and photoexcited hole, transition between electron close to the conduction band and a deeply trapped hole at V_o^{2+}, surface defects, etc. While green emission is typically associated with oxygen deficiency, yellow/orange emission is associated with excess oxygen. The yellow/orange defect emission observed in ZnO synthesized by a hydrothermal method is typically assigned to interstitial oxygen, although other hypotheses such as dislocation related luminescence centers and the DAP-type transitions including a shallow donor and the Li acceptor dominating at low temperatures have been proposed. The assignment of the emission to interstitial oxygen has been confirmed by the reduction of this emission after annealing in a reducing environment. Unlike green emission, yellow emission is not significantly influenced by the surface modifications. On the other hand, red-orange emission (peak position at ~640–680 nm or ~1.8-1.9 eV) has been less commonly observed than green and yellow emissions.

References

[1] Jaeger and C. Richard C. "*Introduction to Microelectronic Fabrication"* (Prentice Hall, Upper Saddle River, 2002).

[2] J. W. Mathews and A. E. Blakeslee, *J. Cryst. Growth* **27**, 188 (1974).

[3] J. W. Mathews, "*Epitaxial Growth, Part B, Materials Science Series*" (Academic, New York, 1975).

[4] J. Narayan and S. Sharan, *Mater. Sci. Eng.* B **10**, 261 (1991).

[5] J. Narayan and B. C. Larson, *J. Appl. Phys.* **93,** 278. (2003)

[6] M. Ichimura and J. Narayan, *Philos. Mag.* A, **72**, 297 (1995).

[7] R. E. Reed-Hill, and R. Abbaschian, "*Physical Metallurgy Principles*", (Pws-Kent, Boston, 1992).

[8] J. P. Hirth, and J. lothe, "*Theory of dislocations*, 2nd edition" (Wiley-Interscience, New York, 1982).

[9] J. Weertman and J. R. Weertman, "*Elementary Dislocation Theory"* (The Macmillan Co., New York, 1964.)

[10] D. Hull and D. J. Bacon, "*Introduction to Dislocations*, 3rd ed." (Pergamon, New York, 1997).

[11] J. W. P. Hsu, M. J. Manfra, R. J. Molnar, B. Heying, and J. S. Speck, *Appl. Phys. Lett.* **81,** 79 (2002).

[12] E. J. Miller, D. M. Schaadt, E. T. Yu, C. Poblenz, C. Elsass, and Speck, *J. Appl.*

Phys. **91**, 9821 (2002).

[13] T. Sugahara, H. Sato, M. Hao, Y. Naoi, S. Tottori, K. Yamashita, Nishino, L. T. Romano, and S. Sakai, *Jpn. J. Appl. Phys. Part* 2 **37,** L398(1998).

[14] S. J. Rosner, E. C. Carr, M. J. Ludowise, G. Girolami, and H. I. Erikson, *Appl. Phys. Lett.* **70**, 420 (2002).

[15] P. J. Hansen, Y. E. Strausser, A. N. Erickson, E. J. Tarsa, P. Kozodoy, E. G. Brazel, J. P. Ibbetson, U. Mishra, V. Narayanamurti, S. P. DenBaars, and J. S. Speck, *Appl. Phys. Lett.* **72**, 2247 (1998).

[16] H. M. Ng, D. Doppalapudi, T. D. Moustakas, N. G. Weimann, and Eastman, *Appl. Phys. Lett.* **73**, 821 (1998).

[17] D. G. Zhao, D. S. Jiang, Hui Yang, J. J. Zhu, Z. S. Liu, S. M. Zhang, J. W. Liang, X. Li, X. Y. Li, and H. M. Gong, *Appl. Phys. Lett.* **88,** 241917 (2006).

[18] J. Y. Shi, L. P. Yu, Y. Z. Wang, G. Y. Zhang, and H. Zhang, *Appl. Phys. Lett.* **80**, 2293 (2002).

[19] J. Als-Nielsen, Des McMorro, "*Elements of Modern X-Ray Physics",* (Wiley&Sons, New York, 2001).

[20] B. D. Cullity, "*Element of X-ray diffraction, 2nd ed"* (Addison Wesley, Cabada, 1978).

[21] B. Heying, X. H. Wu, S. Keller, Y. Li, D. Kapolnek, B.P. Keller, *Appl. Phys. Lett.*

68, 643 (1996)

[22] P. Gay, P. B. Hirsch, and A. Kelly, *Acta Metall.* **1**, 315(1953).

[23] C. O. Dunn, and E. F. Koch, *Acta metall.* **5**, 548 (1957).

[24] P. F. Fewster, 1989, *J. Appl. Cryst.* **22**, 64 (1996).

[25] H. Stehle, and A. Seeger, *Z. Phys.* **146**, 217 (1956)

[26] B. E. Warren, and B. L. Averbach, *J. Appl. Phys.* **21**, 595 (1950).

[27] G. K. Williamson, and W.H. Hall, *Acta Metal.* **1**, 22 (1953).

[28] L. H. Schwartz, and J. B. Cohen, " *Diffraction from Materials, 2nd ed.*" (Springer-Verlag, Berlin,1987).

[29] D. B. Wiliams and C. B. Carter, "*Transmission Electron Microsdopy*" (Plenum Press, New York, 1996).

[30] J. R. Matey, J. Blanc, *J. Appl. Phys.* **57**, 1437 (1985).

[31] C. C. Williams, W. P. Hough, S. A. Rishton, Appl. Phys. Lett. **55**, 203 (1989).

[32] Digital Instruments Inc. *Support Note No. 224, Rev. D.*

[33] Digital Instruments Inc. *Application Modules: Dimension and MultiMode Manual, Rev. B.*

[34] C. F. Klingshirn, "*Semiconductor Optics*" (Springer, Berlin, 1997).

[35] M. Ueta, H. Kanzaki, K. Kobayashi, Y. Toyozawa, and E. Hanamura, "*Excitonic Processes in Solids*" (Springer-Verlag, Berlin, 1984).

[36] A. Teke, Ü. Özgür, S. Dogan, X. Gu, H. Morkoç B. Nemeth, J. Nause, and H. O. Everitt, *Phys. Rev.* B **70**, 195207 (2004).

[37] D. C. Reynolds, D. C. Look, B. Jogai, C. W. Litton, G. Cantwell, and W. C. Harsch, *Phys. Rev.* B **60**, 2340 (1999).

[38] K. Thonke, Th. Gruber, N. Teofilov, R. Schönfelder, A. Waag, and R. Sauer, *Physica* B **308–310**, 945 (2001).

[39] C. Boemare, T. Monteiro, M. J. Soares, J. G. Guilherme, and E. Alves, *Physica* B **308–310**, 985 (2001).

[40] Ü. Özgür, Ya. I. Alivov, C. Liu, A. Teke, M. A. Reshchikov, S. Doğan, V. Avrutin, S.-J. Cho, and H. Morkoç, *J. Appl. Phys.* **98**, 041301 (2005).

[41] A. B. Djurišić, Y. H. Leung, K. H. Tam, L. Ding, W. K. Ge, H. Y. Chen, and S. Gwo, *Appl. Phys. Lett.* **88**, 103107 (2006).

Chapter 3 Experimental setups and procedures

3.1 Epitaxial growth of ZnO film

Various growth methods, such as pulse laser deposition (PLD), metal organic chemical vapor deposition (MOCVD), plasma-assisted molecular beam epitaxy (P-MBE), atmospheric pressure halide vapor phase epitaxy (AP-HVPE), and RF magnetic sputtering have been employed to fabricate ZnO epitaxial films. Among them, PLD is a favorable one because of the advantages of ultra-clean, simplicity, and no need for corrosive gas. Moreover, high-quality epitaxial films of ZnO can be obtained at a relatively low growth temperature (500 °C) due to the high kinetic energy (10-100 eV) of laser ablated species. Besides, the source of Zn and O can be obtained directly from the ZnO target; no extra oxygen supply is necessary. PLD is thus adapted in this work to grow ZnO.

3.1.1 Preparation of substrate and buffer layer

Three different substrates, c-plane sapphire, $\gamma-Al_2O_3/Si(111)$ and $Y_2O_3/Si(111)$ composite substrates, were used for ZnO growth. High quality c-plane sapphire wafers were cut into pieces of an area of 10×10 mm^2 before surface treatment and then cleaned by using the following steps:

(1) Rinse in deionized (D. I.) water for 5 min.

(2) Clean in a supersonic oscillator with Acetone (ACE) for 5 min.

(3) Rinse in D.I. water for 5 min.

(4) Shake in a supersonic oscillator with Isotropic Alcohol (IPA) for 5 min.

(5) Rinse in D.I water for 5 min.

(6) Immerse in $H_2SO_4 : H_2O_2=3:1$ for 10 min.

(7) Rinse in D.I water for 5 min.

(8) Blow dry with N_2 gas.

After the surface treatment, the substrates were mounted on the substrate holder and ready to grow ZnO thin films.

As to the oxide/Si composite substrates, they were prepared by Hong *et al.* [1-3]. The detailed process of manufacture used is described in the following**.** The Si wafers, 2 inch in diameter with (111) as the normal to the wafer plane, were put into a multi-chamber MBE/ultrahigh vacuum (UHV) system [4, 5], after being cleaned with the Radio Corporation of America (RCA) method and a HF dip. Si wafers were heated to temperatures above ~550 °C, and then transferred under UHV (hence, any possibility of Si oxidation was eliminated) to an oxide growth chamber for Al_2O_3 or Y_2O_3 deposition. A high-purity sapphire or Y_2O_3 ceramic pellet was employed. During the oxide deposition using electron beam evaporation, the vacuum in the chamber was maintained in the low 10^{-9} Torr (even with the evaporation of sapphire) and substrate temperatures were maintained at about 700–750 °C for γ-Al_2O_3 and 770 °C for Y_2O_3, respectively.

After the deposition of Al_2O_3 and Y_2O_3, the composite substrates (γ-Al_2O_3/Si and

Y_2O_3/Si) were cut into squares of 10 × 10 mm^2 area for subsequent epitaxial growth of ZnO. Before transferring these substrates into PLD load lock chamber, each substrate was cleaned in a supersonic oscillator with acetone for 5 minutes to remove the particles on the substrate surface. After the surface treatment, the substrates were mounted on the substrate holder and ready for ZnO growth.

3.1.2 Preparation of ZnO films

After the surface cleaning, the substrate was loaded in the chamber with a base pressure of 1×10^{-9} torr (Fig.3-1). We used a focusing lens (f = 40 cm) to converge the laser beam through a chamber window onto the target, which makes 45 degree to the normal of the target. A beam out of a KrF excimer laser (λ = 248 nm) at a repetition rate of 10 Hz was focused to produce an energy density ~ 5–7 $J \cdot cm^{-2}$ on a commercial hot-pressed stoichiometric ZnO (5N) target. At the same time, the laser beam was scanning by moving a reflection mirror, which is carried by a step motor, to prevent laser hitting at the same point on the target that leads to non-uniform film growth. In order to grow a uniform thin film, both the target holder and the sample holder rolled during deposition. The substrate is heated with a halogen light bulb through a programmable temperature controller. The temperatures of the substrate holder were varied from room temperature (RT) to 800 °C. The deposition of the ZnO thin films were carried out without flowing oxygen, under which a background chamber pressure of 1×10^{-8} torr was maintained. Prior to ZnO deposition, Y_2O_3/Si (111) substrates were thermally treated at ~375°C under UHV condition to further clean the surface and to remove the moisture. Table 3-1 lists the growth parameters for ZnO epi-films on different substrates.

Table 3-1 List the parameters of growth for ZnO epi-films on different substrates

Substrate	Growth temperature	Growth rate	Typical thickness	In-situ annealing
c-Al_2O_3	600°C	0.625 $Ås^{-1}$	~650 nm	700 °C
γ-Al_2O_3/Si(111)	300 °C	0.4 $Ås^{-1}$	~300 nm	No
Y_2O_3/Si(111)	400 °C	0.28 $Ås^{-1}$	~210 nm	No

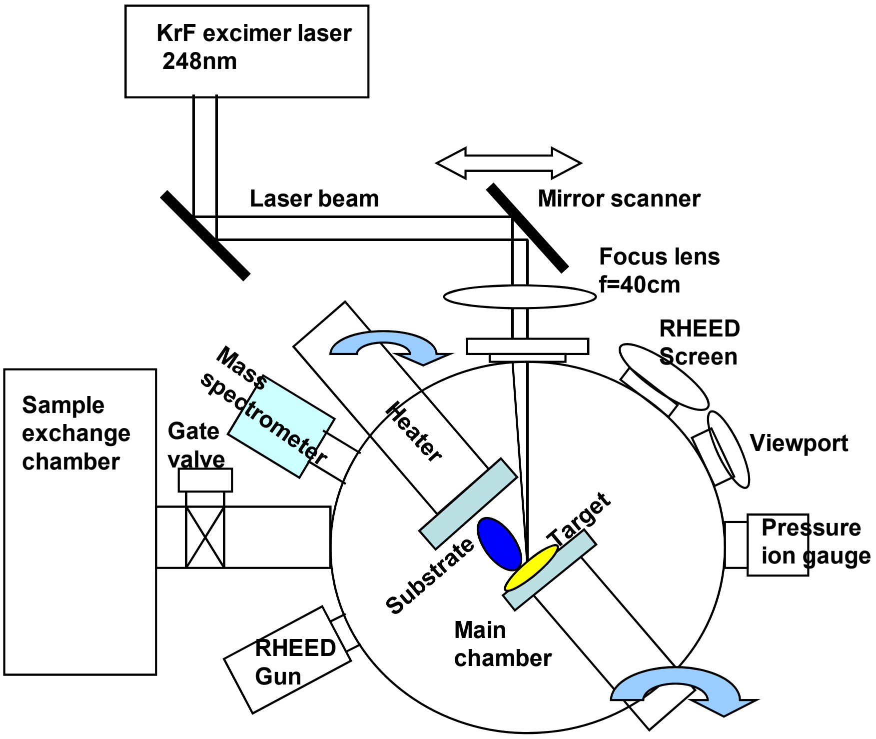

Fig. 3-1 Layout of the PLD growth system

3.2 Structural characterization

3.2.1 X-ray Diffraction

XRD measurements were performed using a four-circle diffractometer, as illustrated in Fig. 3-2 (a), in the single crystal diffraction geometry. A NaI scintillation is mounted on the 2θ circle with a distance of approximate 90 cm away from the sample. Three degrees of freedom, ϕ, χ, and θ circles control the sample orientation as illustrated in the schematic of a four-circle diffractometer (Fig. 3-2 (b)). When sample surface normal is aligned with the z-axis, a ϕ-scan is equivalent to an azimuthal scan often performed to examine the in-plane epitaxial relationship between the grown film and substrate. The combination of χ and θ determines the tilting angle (polar angle) between the surface normal and incident x-ray.

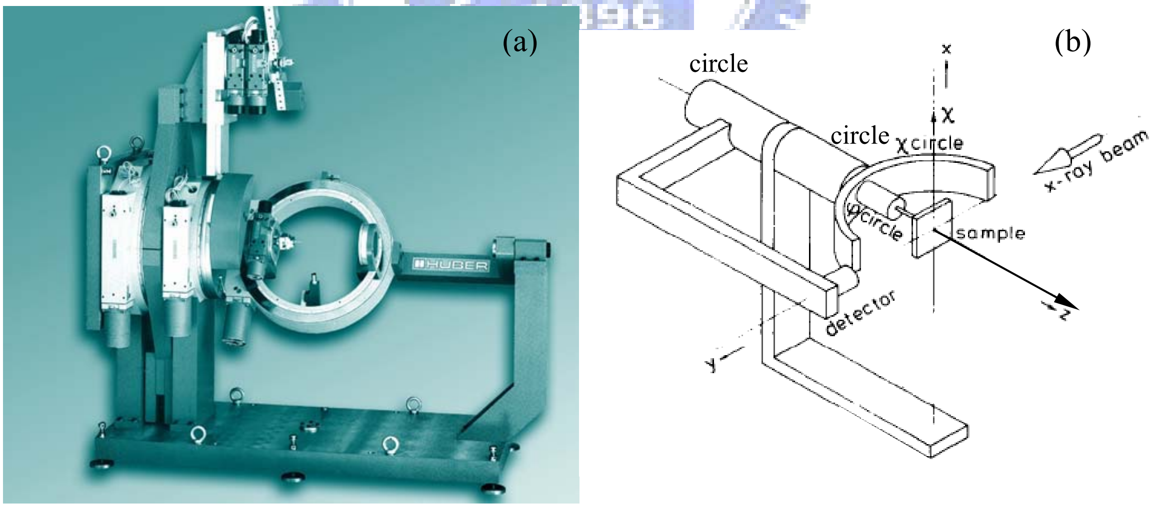

Fig. 3-2 The picture (a) and schematic (b) of a four-circle diffractomter. In (b), all circles are drawn at zero position, so that the coordinate frames attached to the different axes coincide. ϕ and χ are the rotation axes of the corresponding circles. [6]

XRD measurements were conducted at the National Synchrotron Radiation Research Center (NSRRC) in Taiwan. Two pairs of slits located between the sample and detector were employed and yielded a typical resolution of better than 4×10^{-2} nm^{-1}. In terms of line width analysis, the full width at half maximum (FWHM) of each reflection was obtained by fitting the measured data with a pseudo-Voigt function, which is a combination of Gaussian and Cauchy functions [7]. Finite crystallite size and inhomogeneous strain are known as the two major sources of diffraction peak broadening. Line width broadening due to the former is independent of the diffraction order; whereas broadening due to the latter is proportional to the diffraction order. We thus employed a Williamson-Hall plot, which takes advantage of the mentioned different dependence of the line width broadening on the scattering order to discriminate between the two effects.

3.2.2 Transmission Electron Microscopy

Complementary to XRD measurements, cross sectional TEM micrographs were also taken for structural defect analysis. For samples with sapphire substrate, the TEM specimens with the thickness of about 90±10 nm were prepared by focused ion beam (FIB). For samples with Si substrate, TEM specimens were prepared with mechanical polishing, dimpling, and ion milling using a Gatan precision ion polishing system (PIPS) system operated at 4 kV. TEM images were taken with a Philips

TECNAI-20 field emission gun type TEM or a field-emission-gun TEM (JEOL 2100F) operated at 200 kV.

3.3 Electrical characterization

The background electron concentration and mobility of ZnO film was conducted by using Hall measurement with the Van der Pauw configuration (Bio-Rad Microscience HL5500 Hall System) at room temperature. The commercial closed-loop scanning probe microscope (SPM) (Digital Instruments 3100) with Ti/Pt-coated cantilevers (MikroMasch) was adopted for surface morphology and local electrical property measurements. For the SCM measurements, V_{ac} (2 V) and V_{tip} (2 V) were applied

3.4 Optical characterization

3.4.1 Photoluminescence

For photoluminescence (PL) measurements, we used a He–Cd laser (λ = 325 nm) as the excitation source. The schematic of the PL system is shown in Fig. 3-3. The excitation laser beam was directed normally and focused onto the sample surface with power being varied with an optical attenuator. The spot size on the sample is about 100 μm. Spontaneous and stimulated emissions were collected by a fiber bundle and coupled into a 0.32 cm focal-length monochromator (TRIAX 320) with a 1200 lines/mm grating, then detected by either an electrically cooled CCD (CCD-3000) or a photomultiplier tube (PMT-HVPS) detector. The temperature-dependent PL measurements were carried out using a closed cycle cryogenic system. A closed-cycle refrigerator was used to set the temperature anywhere between 15 and 300 K.

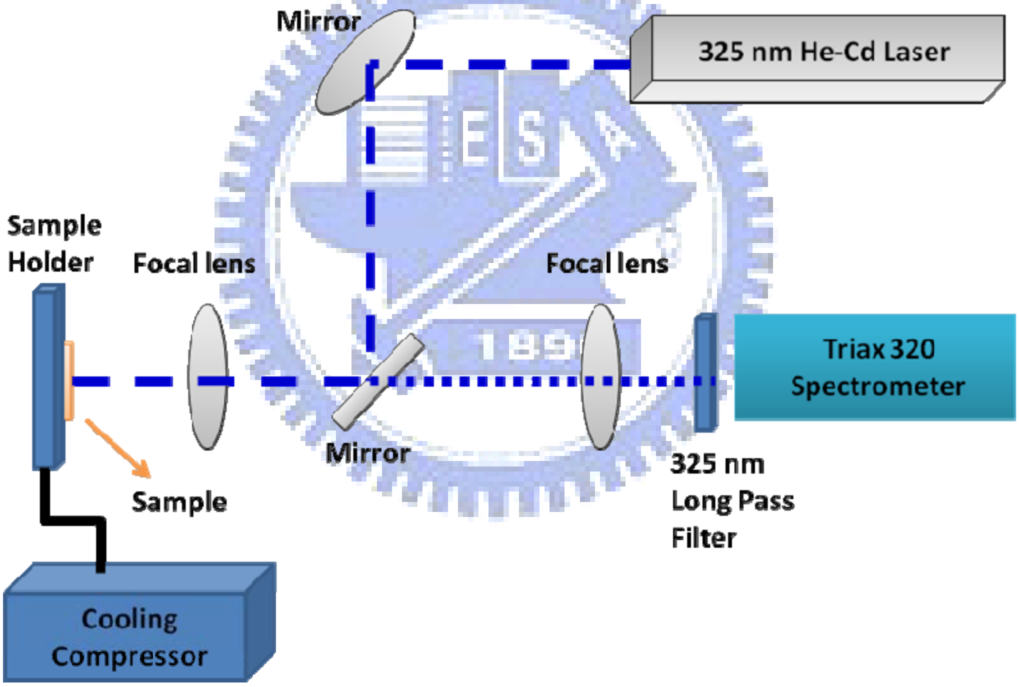

Fig. 3-3 Layout of the PL system

References

[1] S. Y. Wu, M. Hong, A. R. Kortan, J. Kwo, J. P. Mannaerts, W. C. Lee, and Y. L. Huang, *Appl. Phys. Lett.* **87**, 091908 (2005).

[2] M. Hong , J. P. Mannaerts , J. E. Bowers, J. Kwo, M. Passlack, W-Y Hwang, L. W. Tu, *J. Cryst. Growth* **175/176**, 422 (1997).

[3] C. W. Nieh, Y. J. Lee , W. C. Lee, Z. K. Yang,A. R. Kortan, M. Hong, J. Kwo and C.-H. Hsu, *Appl. Phys. Lett.* **92**, 061914 (2008).

[4] M. Hong, M. Passlack, J. P. Mannaerts, J. Kwo, S. N. G. Chu, N. Moriya, S. Y. Hou, and V. J. Fratello, *J. Vac. Sci. Technol.* B **14**, 2297 (1996).

[5] Y. J. Lee, W. C. Lee, C. W. Nieh, Z. K. Yang, A. R. Kortan, M. Hong, J. Kwo, and C.-H. Hsu, *J. Vac. Sci. Technol.* B, **26**, 1124 (2008).

[6] E. Vlieg, J. F. Van der Veen, and J. E. Macdonald, *J. Appl. Cryst.* **20**, 330 (1987).

[7] Th. H. De. Keijser, J. I. Langford, E. J. Mittemeijer, and A. B. P. Vogels, *J. Appl. Cryst.* **15**, 308 (1982).

Chapter 4 Epitaxial ZnO films on c-plane sapphire

4.1. Introduction

Two critical factors govern the quality of heteroepitaxial films are the mismatches of lattice parameters and thermal expansion coefficients between the deposited layer and substrate. As mentioned above in chapter 2, Narayan *et al*. proposed that ZnO films grow on a c-plane sapphire substrate by domain-matching epitaxy (DME), which lattice mismatch decrease from 32 % to 18 % in the initial stage of growth [1]. The distinct thermal expansion coefficient of ZnO and sapphire introduces an additional strain upon post-growth cooling [2]. To accommodate such a large lattice mismatch, the strain energy must be released through the generation of various defects in the epitaxial films. The type and geometry of these defects play a crucial role in determining the mechanical, electric and optic properties of the films. As known for GaN thin films, which have the same wurtzite crystal structure as ZnO, the characteristic defects were high-density, typically 10^9~10^{11} cm^{-2}, threading dislocations (TDs) with the dislocation lines penetrating throughout the entire films. TDs affect the electrical and optical properties of films, including the degradation of devices through carrier scattering [3], non-radiative recombination [4], and a reverse-bias leakage current [5, 6]. Therefore, to understand and subsequently to effectively improve the physical properties of the ZnO thin films, a thorough structural investigation of the characteristics of defects in ZnO epi-films is warranted.

In this chapter, we report the comprehensive study on the structural properties of the ZnO epitaxial layers grown by pulsed-laser deposition (PLD) on (0001) sapphire substrates, including heterogeneous strain, correlation length, tilt and twist angles, and the density of TDs. Cross-sectional TEM was conducted to identify the type and density of the TDs; XRD was carried out to perform quantitative structural analysis. To correlate the surface morphology with the distribution of TDs and to characterize the influence of the TDs on the electric properties at the microscopic scale, we have also conducted AFM and SCM measurements.

4.2 Structural properties and analysis of defect structures

Hall measurements was performed using the Van der Pauw configuration (Bio-Rad Microscience HL5500 Hall System) at 23 °C and yielded a background electron concentration $2.87\times10^{16} - 7.06\times10^{18}$ cm^{-3} with mobility 28.2 - 40.9 $cm^{2}\cdot V^{-1}\cdot s^{-1}$ and resistivity 0.771-0.0216 Ω·cm. The strong PL peak of free exciton at 3.28 eV with FWHM of 105 meV is inspected at room temperature, as shown in Fig. 4-1. No defect emission is also observed at the visible region, ensuring a good optical quality of the ZnO films.

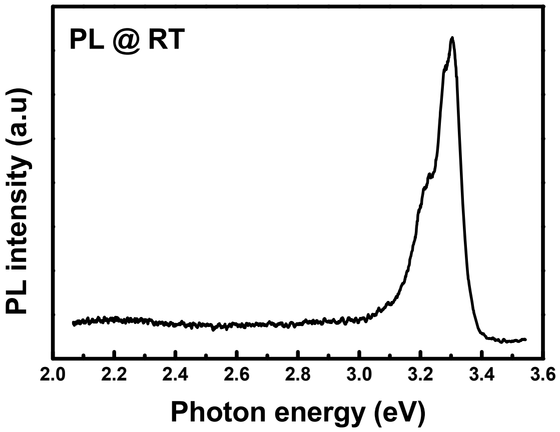

Fig. 4-1 PL spectrum measured at room temperature

X-ray diffraction (XRD) is well established for quantitative exploration of the defect structure over a macroscopic length scale in accordance with crystal imperfection [7]. Radial (2θ–ω) scans along surface normal were conducted and only the (000*l*) reflections of both sapphire and ZnO were observed, elucidating the c-plane orientation of the grown ZnO layers. Azimuthal cone scans (ϕ scans) across the off-normal ZnO $\{20\bar{2}2\}$ and sapphire $\{20\bar{2}2\}$ peaks, as illustrated in Fig. 4-2(a), were measured to examine the in-plane epitaxial relation. Six ZnO diffracted peaks (FWHM ~ 0.57°) that are evenly spaced 60° apart confirm that the ZnO film has 6-fold rotational symmetry against surface normal and is grown epitaxially on the *c*-plane sapphire. The 30° offset between the $\{20\bar{2}2\}$ reflections of ZnO and sapphire verifies the in-plane epitaxial relationship of $[10\bar{1}0]_{\text{sapphire}} \parallel [11\bar{2}0]_{\text{ZnO}}$ and $[11\bar{2}0]_{\text{sapphire}} \parallel [01\bar{1}0]_{\text{ZnO}}$.

To characterize the structural quality of the grown films, the ω–rocking curve of the ZnO (0002) reflection, as shown in Fig. 4-2(b), was measured. The rocking curve of the nearly resolution-limited sapphire (0006) reflection was also shown as a reference. The narrow width, 0.0072°, of sapphire (0006) reflection reveals that the contribution of instrumental broadening to the ZnO width is negligible. The obtained mosaic spread of the ZnO film, 0.0482°, is much smaller than other reported values, typical of ~0.2°, of ZnO films prepared with PLD [8, 9]. It is also noticed that the line widths of ZnO specular (0002) and off-normal $\{20\bar{2}2\}$ reflections are different by more than an order of magnitude. Such a prominent difference of diffraction features in these two groups reveals the structural characteristics of the films.

TDs in a film produce crystalline plane distortions and the associated lattice deformation depends on the geometry of the TDs [10]. For a c-plane ZnO layer, TDs with their dislocation lines lying along the [0001] direction, i.e. normal to the ZnO/sapphire interface are most often observed [2, 11]. In our case, the majority of TDs have their lines along the [0001] direction, which will be discussed in more details in TEM results. For a (0001) oriented thin film with wurtzite structure, the TDs are classified to three different types according to the direction of the corresponding Burgers vector (b) relative to the [0001] line direction. They are edge dislocation with $b_E = 1/3\cdot\langle 11\bar{2}0\rangle$, screw dislocation with $b_C = \langle 0001\rangle$, and mixed dislocation with b_M = 1/3·<11$\bar{2}$3>, which is a combination of b_E and b_C. Pure edge TDs twist surrounding ZnO lattice about [0001], leading to the formation of vertical grain boundaries [2, 12]. Under this circumstance, the (*hkil)* crystalline planes with nonzero in-plane component, i.e. either *h* or *k* is not zero, are distorted. On the other hand, the pure screw TDs result in the tilting of the ZnO lattice, generating a pure shear strain field [13], and the crystalline planes with nonzero *l* are deformed. Therefore, to investigate the influence of edge TDs, we measured the profiles of $(h0\bar{h}0)$ surface reflections, which are not sensitive to lattice distortion caused by pure screw TDs. Such scans were performed in the grazing incidence diffraction geometry by keeping the surface normal almost perpendicular to the vertical scattering plane. The FWHMs of ω-rocking curves reflect the lattice twist and the widths of radial scan yield the lateral strain field and domain size. As a complement, we also recordemeasured the line widths of the (000*l*) normal reflections, which are not affected by the pure edge TDs. The ω-rocking curves and radial scans provide the lattice tilt angle and coherence size as well as strain profile along surface normal, respectively.

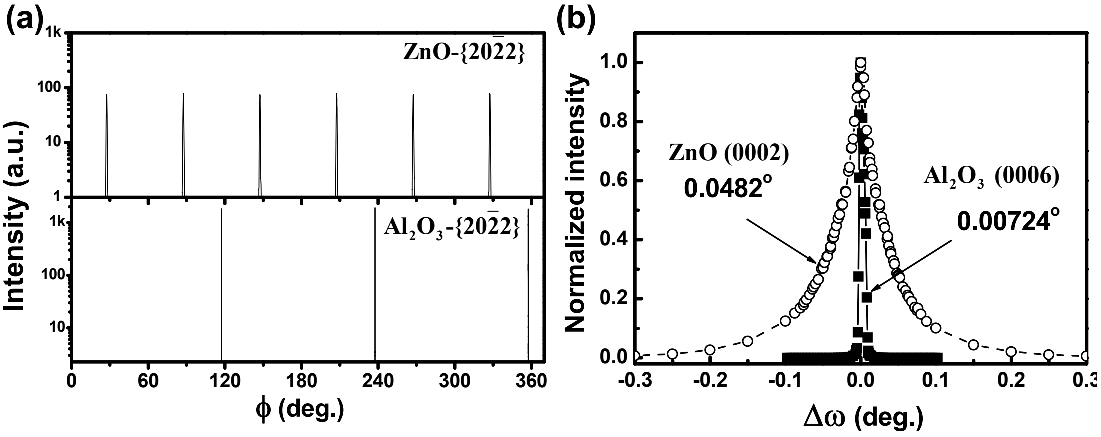

Fig. 4-2 (a) Azimuthal scans of ZnO $\{20\bar{2}2\}$ and sapphire $\{20\bar{2}2\}$ peaks. (b) Comparison of ω scans of ZnO (0002) and substrate sapphire (0006) peaks. (All marked values denote FWHM.)

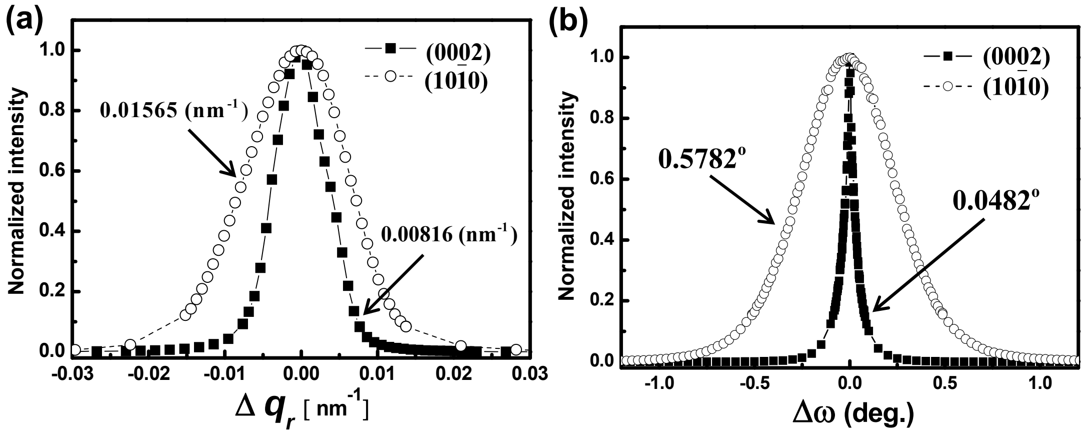

Fig. 4-3 Superimposed radial (a) and symmetric ω scans (b) of ZnO (0002) and $(10\bar{1}0)$ reflections. The abscissa of Fig. (a), Δq_r, is the deviation of the scattering vector, $q = 2\pi\sin(\theta)/\lambda$, away from the corresponding reflection in the radial direction. (All values denote FWHM.)

Figure 4-3 (a) displays the intensity distribution of scattered X-rays along the radial scans across ZnO (0002) and $(10\bar{1}0)$ reflections, of which the former is along the growth direction and the latter lies on the sample surface. The FWHM of the former, 0.00816 nm^{-1}, is significantly smaller than that of the latter, 0.01565 nm^{-1}, indicating the strain along surface normal caused by screw TDs is much smaller than that along lateral direction caused by edge TDs. The profiles of ω-rocking scans across ZnO (0002) and $(10\bar{1}0)$ reflections are illustrated in Fig. 4-2(b). Similarly, the FWHM of the (0002) reflection, 0.048°, is much smaller than that of the $(10\bar{1}0)$ reflection, 0.578°, revealing the tilt angle to be smaller than the twist angle. This pronounced difference of widths between (0002) and $(10\bar{1}0)$ reflections strongly indicates that the density of pure edge TDs is greater than that of pure screw TDs. These observations are qualitatively similar to what observed for GaN grown on *c*-sapphire [10, 14]. Analogous phenomena are attributed to the same crystal structure of ZnO and GaN, both belonging to space group $P6_{3mc}$, and the similar lateral lattice parameter, with a difference ~1.8 %.

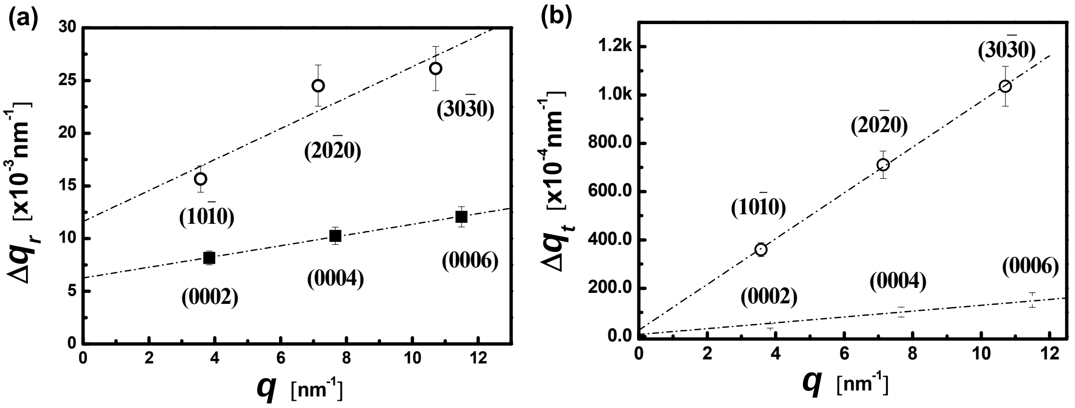

Fig. 4-4 Williamson-Hall plots for a ZnO layer of radial scans (a) and ω-rocking curves (b). The symmetric radial scans and ω-rocking curves were measured for (000*l*) and $(h0\bar{h}0)$ reflections as indicated in the figures. Dashed lines are linear fits of the data.

To obtain meaningful quantitative results, we employed a Williamson-Hall plot, Δq_r *vs*. q plot with $q = 2\sin\theta/\lambda$ denoting the scattering vector and Δq_r standing for the line width in q along the radial direction, to separate the broadening due to finite structural coherence length from strain induced broadening. The inverse of ordinate intercept yields the coherence length, i.e., the effective domain size, and the slope yields the root-mean-square (RMS) inhomogeneous strain averaged over the effective domains [15]. Figure 4-4(a) illustrates the Williamson-Hall plot of radial scans along ZnO $(000l)$ and $(h0\bar{h}0)$ reflections. The correlation lengths obtained are 159.8 nm along the surface normal, which is only a fraction of the film thickness, and 86.1 nm along the lateral direction. The average lateral strain is 1.49×10^{-3}, about three times that along the surface normal, 0.51×10^{-3}, manifesting edge dislocations to be the dominant cause of distortion of the ZnO lattice. Analogous to the Williamson-Hall plot for radial scans, Fig. 4-4 (b) shows a Δq_t *vs*. q plot, where $\Delta q_t = \Delta\omega \times q$ denoting the line width in q along the transverse direction, for ω-scans across the $(000l)$ and in-plane $(h0\bar{h}0)$ reflections, of which the slopes yield the spreads of tilt and twist angle, respectively. The obtained tilt angle (α_Ω) is 0.089°, which is only one sixth of the twist angle (α_Φ), 0.542°. The density of TDs can be evaluated from the corresponding Burgers vector and the tilt/twist angular. For screw TDs, the density N_S is calculated according to $N_S = \dfrac{\alpha_\Omega^2}{4.35 b_C^2}$ [16], in which α_Ω is the tilt angle and b_C denotes the length of corresponding Burgers vector b_C, which is [0001] with $b_C = 0.5225$ nm in this case. Applying the values determined from XRD, we obtained $N_S = 2.03\times10^{8}$ cm^{-2}. For edge TDs, the formula employed to calculate the density, N_E, depends on the spatial arrangement of the TDs [17]. Assuming a random distribution, we apply $N_E = \dfrac{\alpha_\Phi^2}{4.35 b_E^2}$, in which $\alpha_{.}$ stands for the twist angle. In the case of TDs accumulating at a small-angle boundary, we adopt the formula $N_E = \dfrac{\alpha_\Phi}{2.1|b_E|L}$, where L denotes the correlation length along the in-plane direction. In both formulae of N_E, b_E is the length of associated Burgers vector $b_E = 1/3 < 11\bar{2}0 >$, 0.3238 nm. The edge TDs densities for a random distribution and for accumulating at small-grain boundaries so obtained are 2.00×10^{10} cm^{-2} and 1.62×10^{10} cm^{-2}, respectively. Even though the authentic distribution of edge TDs is uncertain, we expect it to be between a random distribution and an accumulation at a small-angle grain boundary, and the density N_E to be of order 10^{10} cm^{-2}. The results indicate that N_E is about 100 times higher than N_S, hence edge TDs are indeed the dominant type of dislocations in ZnO films grown on *c*-plane sapphire, in agreement with a conclusion drawn from a qualitative comparison of the FWHMs of (0002) and $(10\bar{1}0)$ reflections.

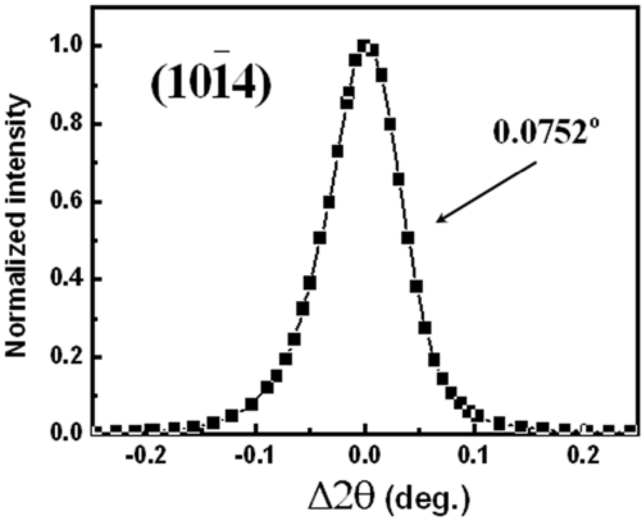

Fig. 4-5 The profile of a radial scan across ZnO $(10\bar{1}4)$ reflection measured in an asymmetric geometry.

In a further examination of those results, we measured the radial scan profile of an off-normal $(10\bar{1}4)$ reflection, of which both edge and screw TDs contribute to the line width broadening. The radial scan measured in an asymmetrical geometry is displayed in Fig. 4-5. The obtained width was compared with the calculated value by using the characteristic parameters of the edge and screw TDs respectively determined from $(h0\bar{h}0)$ and $(000l)$ reflections. The mean square strain of $(10\bar{1}4)$ planes induced by three edge dislocation systems with $b_E = 1/3 <11\bar{2}0>$ and slip planes $\{1\bar{1}00\}$ and the screw dislocation with b_C = <0001> can thus be calculated using the TDs density obtained above (N_E=1.62×10^{10} cm^{-2}, N_S=2.03×10^{8} cm^{-2}) [14]. The strain broadening of the $(10\bar{1}4)$ Bragg reflection in the radial direction is subsequently calculated based on such strain fields to yield an average 0.078°. This value is in good agreement with the measured one, 0.074°.

TEM contrast analysis was also performed to characterize the nature of the TDs. On the basis of the invisibility criterion, $g \cdot b = 0$, where g denotes the diffraction vector, the dislocations with Burgers vector b perpendicular to the diffraction vector g are invisible in the images. We thus took bright-field cross-sectional TEM images under a two-beam contrast condition with the zone axis near $[10\bar{1}0]$ and diffraction vectors g equal to (0002), $(11\bar{2}0)$ and $(11\bar{2}2)$, as shown in Fig. 4-6(a), (b) and (c), respectively. Pure edge TDs with $b_E = 1/3 \cdot \langle 11\bar{2}0 \rangle$ are invisible in images recorded with $g = (0002)$ but are in contrast in images with $g = (11\bar{2}0)$ and $(11\bar{2}2)$. On the contrary, pure screw TDs with $b_C = \langle 0001 \rangle$ are out of contrast in the $g = (11\bar{2}0)$ case and are visible as $g = (0002)$ and $(11\bar{2}2)$. As to the TDs of mixed type with $b_M = 1/3 \cdot \langle 11\bar{2}3 \rangle$, they are visible in all three images. In all three micrographs, TDs seen as dark lines stem from the ZnO/sapphire interface with their dislocation lines primarily along the [0001] direction. The number of TDs is significantly less in Fig. 4-6(a) as compared with those in 6(b) and 6(c), manifesting that only a small fraction of TDs belongs to pure screw type. Taking the specimen thickness 90±10 nm into account, we calculated the densities of edge, screw and mixed TDs to be approximately $1.5\pm0.2\times10^{10}$ cm^{-2} (~ 77%), $4.3\pm0.3\times10^{8}$ cm^{-2} (~ 2%), and $4.1\pm0.5\times10^{9}$ cm^{-2} (~ 21%), respectively. Amounting to 98% of the total TDs contains the edge component as determined from the TEM measurements.

In some regions, as shown in Fig. 4-6(d), the mergence of dislocation lines to form half loops was observed, especially in the bottom half of the film close to the interface, revealing the strong interaction between the TDs. It appears that the annihilation of two nearby dislocations of opposite Burgers vectors leads to the formation of these loops. The presence of many half loops and the difference of TDs density in depth may explain the smaller vertical structural coherence length found in XRD measurements as compared with the film thickness.

4.3 Correlation between defect structures and morphology

By tilting the TEM specimen about growth direction, we found that the diameters of columnar grains varied between 50 and 150 nm. After careful analysis, we obtained a mean diameter 94 nm and a FWHM 56 nm in lateral size distribution. Small-angle grain boundaries were also observed during the TEM measurement by tilting the sample about 0.6°, which is comparable to the FWHM (0.58°) of the azimuthal scan across ZnO$\{20\bar{2}2\}$ reflections. From the TEM images, we found that the pure TDs are not uniformly distributed in the film, but aggregate and encircle epitaxial ZnO cores. The structure of the ZnO layer is thereby described as a columnar-grain structure consisting of epitaxial cores and small-angle grain boundaries (annular regions) with edge TDs at a large density. Figures 4-7(a) and (b) also show the AFM topography and SCM (dC/dV) images concurrently acquired with a V_{tip} of 2 V. The charge carriers of the ZnO film is in the accumulation condition under a tip bias of 2 V, because ZnO is an intrinsic n-type semiconductor. The features observed in the two images are clearly mutually correlated. The hexagonal domains are clearly resolved in Fig. 4-7(b); the lateral domain size about 86 nm is comparable with that obtained with XRD and TEM. Figure 4-7(c) shows the dual section profiles recorded along the line marked with arrows in both images to illustrate the correlation between the topography and the SCM signals. Comparing with the structural information obtained from XRD and TEM measurements, we ascribed the yellow circumferential curves and red regions to grain boundaries and epitaxial cores, respectively. We exclude the possibility that the contrast in the capacitance signal is resulted from a topographic effect because the SCM contrast varied with tip bias (the stripe near the top of Fig. 4-7(b) with dim contrast was recorded with $V_{tip} = 1$ V) and the root-mean-square (RMS) roughness is small, about 0.25 nm. The contrast of AFM and SCM images is opposite, i.e., the annular region has a higher SCM signal level.

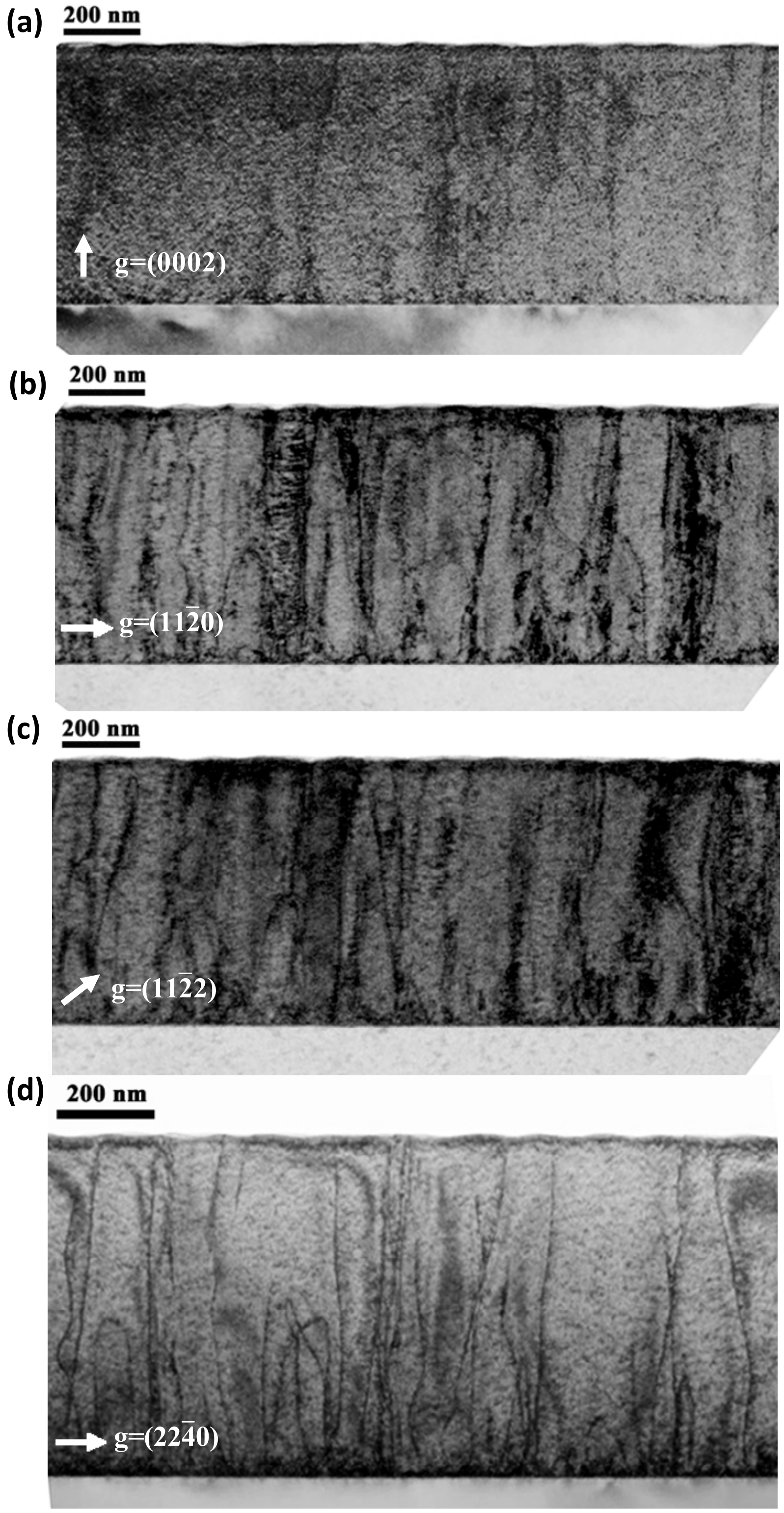

Fig. 4-6 Two-beam bright-field cross-sectional electron micrographs of a ZnO thin film with g = (0002) (a), $(11\bar{2}0)$ (b), and $(11\bar{2}2)$ (c). Image (d) with g = $(22\bar{4}0)$ was taken at a region with particularly high TDs density, in which several half loops were clearly identified.

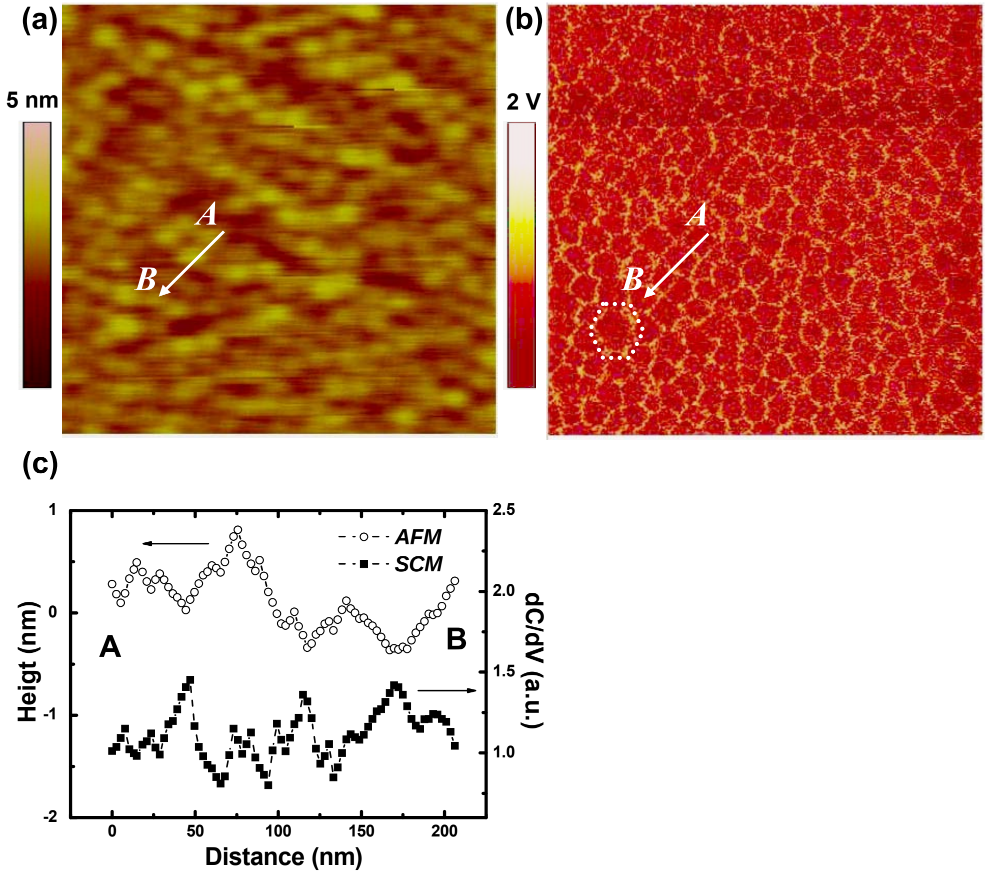

Fig. 4-7 AFM topography (a) and SCM differential capacitance (dC/dV) image (b) of a ZnO film of area 1×1 μm^2 acquired at V_{tip} = 2 V. The region near the top with dim contrast in (b) was acquired at V_{tip} = 1 V. (c) A dual-section profile recorded along the line indicated from A to B by arrows in (a) and (b).

4.4 Correlation between defect structures and electrical properties

Figure 4-8(a) and (b) show the AFM topography and the SCM images simultaneously acquired while the tip was applied with a V_{tip} of 0.664 V plus a 2 V ac modulation at 23 kHz. Viewing the topographic image, we observed small grains of 80 ~ 110 nm in diameter, which is comparable to the grain size obtained by XRD and TEM. As discussed above, the structure of the ZnO layer is described as a columnar-grain structure consisting of epitaxial cores and small-angle grain boundaries (annular regions) with edge TDs at a large density. The bright and dark regions in the topographic AFM image are associated with the epitaxial cores and the boundaries, respectively.

The correlation between the AFM and the SCM images is obvious. It is worth noting that we exclude that the correlation is due to topographic effect on the capacitance signals since the root-mean-square surface roughness is only 1.2 nm and the SCM contrast vanishes as a negative V_{tip} is applied. The $\mathrm{d}C/\mathrm{d}V$-V_{tip} curves shown in Fig. 4-8(c) were extracted from the grain region (cross marked A) and from the boundary region (cross marked B) in Fig. 4-8(b), respectively. The curves were obtained after averaging forward and reverse sweeps to exclude the piezoelectricity of ZnO. It was found that the peak value of $\mathrm{d}C/\mathrm{d}V$ signal at point A is lower than that at point B, implying that the grain region has the capacitance with less dependence on the dc bias and its local free carrier concentration in the grain region is higher than that at the boundary. The flatband voltage, defined as the voltage at the $\mathrm{d}C/\mathrm{d}V$ peak, shifts about +0.57 V between the two regions; this accounts for the SCM contrast at the optimum V_{tip} (0.664 V). Furthermore, the coincidence of the curves as the V_{tip} set below −0.7 V suggests that the response of charge carriers to ac modulation is similar between the post-depletion and the inversion realms.

The shift of flatband voltage can be attributed to two factors: interface trap density

(D_{it}) and fixed charge density (N_f) [18]. N_f only causes a shift of dC/dV curve, but D_{it} can introduce not only a shift but also a stretch. Hong *et al*. [19] reported that the ratio of FWHM of dC/dV curve to ΔV is fixed if only D_{it} is present, where ΔV represents the deviation in bias from the dC/dV peak with a given change in dC/dV value (and hence a change in surface potential). The ratios of FWHM to ΔV in the grain and boundary regions estimated from Fig. 4-8(c) are 0.85 and 0.91, respectively. Consequently, we believe that the shift of flatband voltage is mainly caused by the effect of D_{it}, which is higher in boundary regions than in the grain regions. Accordingly, the local carrier concentration should be lower at the boundary region, which agrees with the inference from the peak value of dC/dV above. The TDs would increase the D_{it} in the annular region and consequently introduce deep acceptor-like trap states in ZnO films.

This SCM result agrees with the reported charge density distribution around the dislocation cores by Müller *et al.*, who measured the electrostatic potential in the vicinity of charged dislocations by employing electron holography in a TEM and derived the charge density accordingly [20]. Since wurtzite ZnO has a high piezoelectric constant, it is possible that part of charges observed by SCM could be piezoelectric (bound) charges at the surface, generated by the strain field of the dislocations [21]. However, Müller *et al.* estimated the magnitude of piezoelectric charges in the dislocations is insignificant as compared with that of charges filled in the dislocations. Therefore, we suggest that D_{it} is the major component of dislocation charges in ZnO.

Fig. 4-9(a) and (b) show the AFM topography and current images simultaneously extracted under V_{tip} = 3 V, with the current image shown at reverse contrast. To manifest the correlation between topography and conductivity, these two images are overlaid as shown in Fig. 4-9(c). The current spots, indicative of the more conductive regions, occur only in the grains but not at the boundaries. The *I-V* curves taken in the grain (cross marked A) and at the boundaries (cross marked B) are both shown in Fig. 4-9 (d). The observed shift of forward bias between grain and boundary indicates the possibility of charge trapping. The current apparently diminishes at the reverse bias because of the rectification of the nonideal Pt/ZnO Schoktty contact, as there exists a native insulator at the tip-sample junction. In addition, the emission current at the boundary is lower than that at the grain, reflecting that the boundary has a potential barrier higher than the grain. Tivarus *et al.* [22] has demonstrated that the negative charge states related to the TDs close to the surface increased the local potential barrier at the dislocation, and that the emission current was suppressed at the boundary due to the increase in potential barrier associated with the negative-charged D_{it}.

Recently, we further investigated the potential barrier height by fitting the local *I-V* curve of CAFM in the negatively charged edge TDs region using the model proposed by Müller *et al.* [20]. The result indicates the potential barrier height of larger than 0.4 eV below the conduction band minimum (E_{CBM}) of ZnO between edges TDs region and epitaxial core, implying the dislocation states of ~0.4 eV below E_{CBM}. Collating the defect energy level of ZnO with dislocation state, we suggest the negatively trapped charges are associated with the point defects formed by the Zinc vacancy (V_{Zn}), which is ~0.4 - 0.5 eV below E_{CBM} [23, 24]. The observation indicates the edge dislocation core is formed by Zn vacancies and electrically active.

The increase in the potential barrier and the charge scattering related to D_{it} would lead to the reduction of the carrier mobility, thereby degrading the performance of electro-optic devices. Therefore, the reduction of TDs is an important issue for the future application of ZnO thin films. On the other hand, because the distribution of the screw TDs is much less than that of the edge TDs, we cannot confirm the location of the screw TDs and their electrical properties.

4.5 Summary

Our XRD, TEM, AFM and SCM measurements on epitaxial ZnO films grown by PLD on c-plane sapphire substrates reveal that the predominant defect structure in it are edge TDs. These TDs are not uniformly distributed in the ZnO layer but aggregate to form annular regions around columnar epitaxial cores. The local spectra of the dC/dV-V_{tip} and I-V_{tip} curves obtained from the SCM and C-AFM analyses suggest that the flatband voltage shifts and the potential barrier increases at the grain boundary, due to the interface trap density induced by the existence of high-density edge TDs. The TDs would increase the D_{it} in the annular region and consequently introduce deep acceptor-like trap states in ZnO films. To effectively reduce TDs density is still an important issue in the future applications of ZnO thin films.

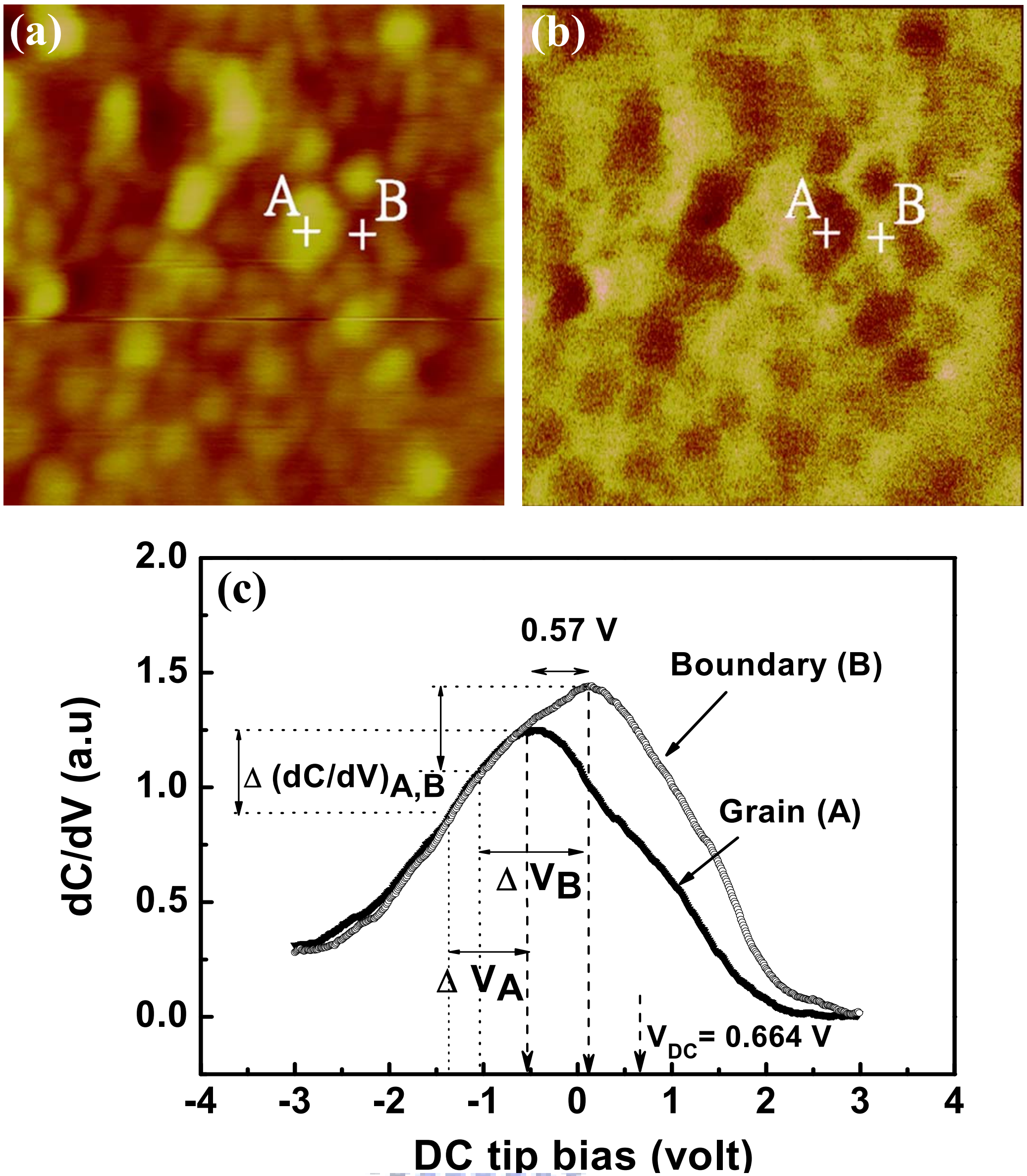

Fig. 4-8 AFM topography (a) and SCM differential capacitance (dC/dV) image (b) acquired at V_{tip} = 0.664 V in ZnO film. Local dC/dV-V_{tip} curve measured on the grain (cross marked A) and at the boundary (cross marked B) as a function of V_{tip} are shown in (c). ΔV_{A} and ΔV_{B} represent the variation of V_{tip} with the same change in (dC/dV)$_{\mathrm{A,B}}$ (or surface potential). The dash lines show the dC/dV peaks (flatband voltage) of the curves.

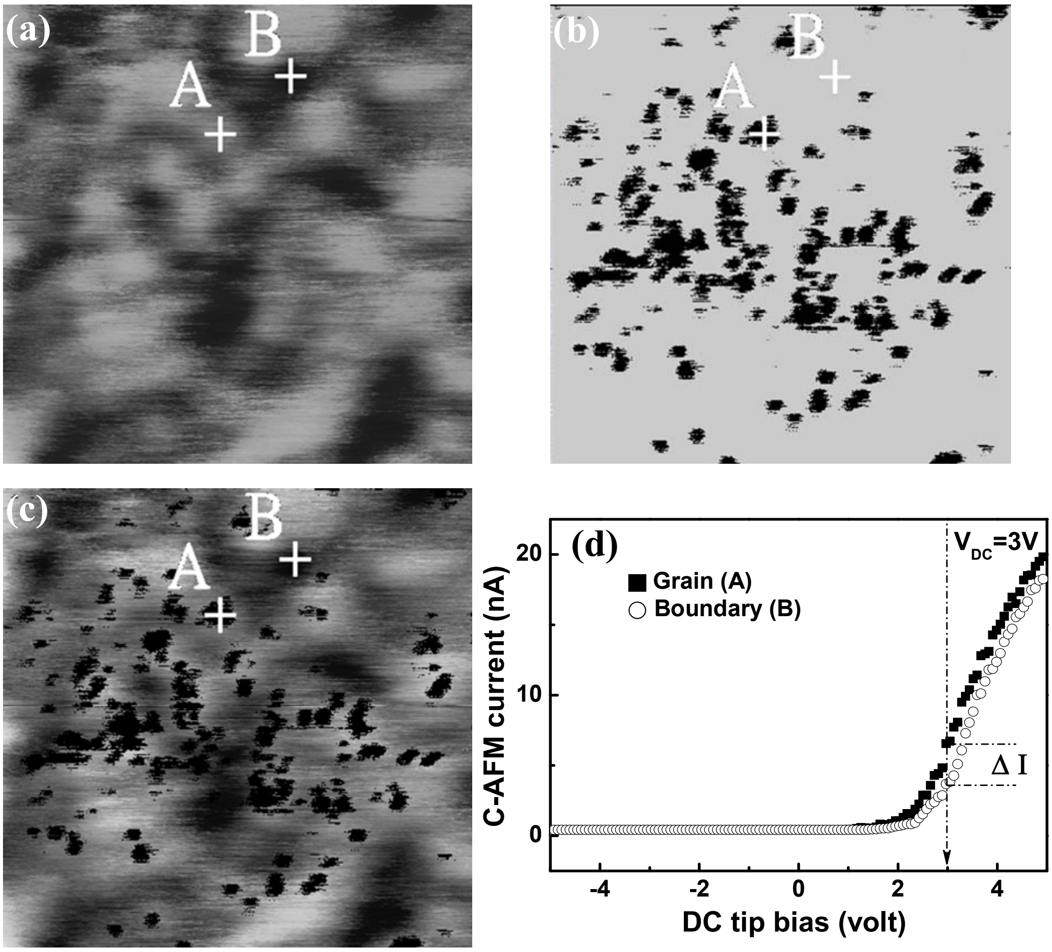

Fig. 4-9 AFM topography (a) and C-AFM current image (b) of ZnO film with area of 0.4×0.4 μm^2 acquired at V_{tip} = 3 V. The current image was shown at reverse contrast. Overlaid images of (a) and (b) with the same area was shown in (c). Local I-V_{tip} curves taken in the bright region (cross marked A) and the dark region (cross marked B) of (a) as a function of V_{tip} was plotted in (d). The ΔI marks the current difference of the I-V_{tip} curves between A and B at V_{tip} = 3 V.

References

[1] J. Narayan, and B. C. Larson, *J. Appl. Phys.* **93**, 278 (2003).

[2] F. Vigué, P. Vennéguès, S. Vézian, M. Laügt, and J.-P. Faürie, *Appl. Phys. Lett.* **79**, 194 (2001).

[3] H. M. Ng, D. Doppalapudi, T. D. Moustakas, N. G. Weimann, and L. F. Eastman, *Appl. Phys. Lett.* **73**, 821(1998).

[4] T. Sugahara, H. Sato, M. Hao,Y. Naoi, S. Tottori, K. Yamashita, K. Nishino, L. T. Romano and S. Sakai, *Jpn. J. Appl. Phys. Part* 2, **37**, L398 (1998).

[5] J. W. P. Hsu, M. J. Manfra, R. J. Molnar, B. Heying, and J. S. Speck, *Appl. Phys. Lett.* **81**, 79 (2002).

[6] E. J. Miller, D. M. Schaadt, E. T. Yu, C. Poblenz, C. Elsass, C. And J. S. Speck, *J. Appl. Phys.* **91**, 9821-9826 (2002).

[7] M. A. Krivoglaz, Editor. "*X-Ray and Neutron Diffraction in Non-ideal Crystals*" (Berlin: Springer, 1996).

[8] R. D. Vispute, V. Talyansky, Z. Trajanovic, S. Choopun, M. Downes, R. P. Sharma, T. Venkatesan, M. C. Woods, R. T. Lareau, K. A. Jones, and A. A. Iliadis, *Appl. Phys. Lett.* **70**, 2735 (1997).

[9] A. Fouchet, W. Prellier, B. Mercey, L. Méchin, V. N. Kulkarni, and T. Venkatesan, *J. Appl. Phys.* **96**, 3228 (2004).

[10] B. Heying, X. H. Wu, S. Keller, Y. Li, D. Kapolnek, B. P. Keller, S. P. DenBaars, and J. S. Speck, *Appl. Phys. Lett.* **68**, 643 (1996).

[11] S. H. Lim, J. Washburn, Z. Liliental-Weber, and D. Shindo, J. *Vac. Sci. Technol.* A **19**, 2601 (2001).

[12] R. Chierchia, T. Böttcher, H. Heinke, S. Einfeldt, S. Figge, and D. Hommel, *J. Appl. Phys.* **93**, 8918 (2003).

[13] V. Strikant, J. S. Speck, and D. R. Clarke, J. Appl. Phys. **82**, 4286 (2002).

[14] T. Metzger, R. Hö pler, E. Born, O. Ambacher, M. Stutzmann, R. Stömmer, M. Schuster, H. Gö bel, S. Christiansen, M. Albrecht, and H. P.Strunk, *Philos. Mag.* A, **77**, 1013(1998).

[15] G. K. Williamson, and W. H. Hall, *Acta Metall.* **1**, 22 (1953).

[16] P. Gay, P. B. Hirsch, and A. Kelly, *Acta Metall.* **1**, 315 (1953).

[17] H. J. Hordon, and B. L. Averbach, *Acta Metall.* **9**, 237 (1961).

[18] E. H. Nicollian and J. R. Brews, “ *MOS Physics and Technology* ” (New York: Wiley, 1982).

[19] Y. D. Hong, Y. T. Yeow, W. K. Chim, K. M. Wong, and J. J. Kopanski, *IEEE Trans. Electron Devices* **51**,1496(2004).

[20] E. Müller, D. Gerthsen, P. Brückner, F.Scholz, Th. Gruber, and A. Waag, *Phys. Rev.* B **73**, 245316-1(2006).

[21] C. Shi, P. M. Asbeck, and E. T. Yu, *Appl. Phys. Lett.* **74**, 573 (1999).

[22] C. Tivarus, Y. Ding, and P. Pelz, *J. Appl. Phys.* **92**, 6010(2002).

[23] S.A.M. Lima, F.A. Sigoli, M. Jafelicci Jr, and M.R. Davolos, *Int. J. Inorg. Mater.* **3**,749 (2001).

[24] S. B. Zhang, S.-H. Wei, and Alex Zunger, *Phys. Rev.* B **63**, 075205 (2001)

Chapter 5 Epitaxial ZnO films on Si (111) using a γ-Al_2O_3 buffer Layer

5.1 Introduction

Recently, much attention has been paid to heteroepitaxially grown ZnO on Si substrate because of the unique possibility of integrating well-established Si electronics with ZnO-based optoelectronic devices. Unfortunately, direct growth of epitaxial ZnO films on Si is an extremely difficult task due to the formation of amorphous SiO_2 layer at ZnO/Si interface [1, 2] that usually results in polycrystalline films with preferred orientation [3]. Although significant efforts have been made to use nonoxide materials, such as ZnS [1], Si_3N_4 [2], Zn/MgO [4], and Mg/MgO [5], as buffer layers, the growth of high-quality ZnO epi-films on Si is still regarded as an arduous challenge.

The other issue for the growth of high quality ZnO epi-films is the existence of high-density threading dislocations (TDs) originated from the large difference in lattice mismatch (-15.4%) and thermal expansion coefficient (56%) between ZnO (thermal expansion coefficient $\alpha \sim 5\times10^{-6}$ K^{-1} [6], lattice parameters a = 3.249 Å, c = 5.2063 Å) and underneath Si substrate ($\alpha = 3.6\times10^{-6}$ K^{-1} [7], a = 5.431 Å). The point defects captured by TDs stress field act as traps and recombination sites forming deep electronic states inside the band gap [8, 9]. They can lead to electron scattering [10], significantly affect the optical performance and electron mobility [9, 11], and adversely demote the device efficiency. In this chapter, the growth of high-quality epitaxial ZnO films using PLD on Si(111) substrates with a ~ 15.3 nm thick γ-Al_2O_3 film as the buffer layer is reported. The good crystal structure of thin ZnO films was confirmed by XRD and TEM. Their optical characteristics were studied using PL and correlated with its structural properties.

5.2 Structural properties

Radial scan along surface normal (θ-2θ scan) of the ZnO layer grown at 300^{o}C were illustrated in Fig. 5-1, where the abscissa $q_z = 4\pi\sin(\theta)/\lambda$ denotes the momentum transfer along surface normal and λ is the incident x-ray wavelength. Only ZnO (0002), γ-Al_2O_3 (111) and (222), and Si (111) reflections were observed, elucidating a crystalline orientation of $(0002)_{ZnO} \parallel (111)_{\gamma-Al_2O_3} \parallel (111)_{Si}$ along surface normal. The pronounced thickness fringe observed near γ-Al_2O_3 (222) reflection indicates the sharpness of the γ-Al_2O_3 interfaces; the fringe period yields a layer thickness of ~ 15.3 nm. From the full width at half maximum of the γ-Al_2O_3 (222) reflection, we derived the vertical coherence length of the buffer layer, using the Scherrer's equation, to be ~15 nm, which is close to the layer thickness. This reflects that the structural coherence of the buffer layer is maintained over almost the entire layer thickness.

Azimuthal cone scans (ϕ–scans) across the off-normal ZnO $\{10\bar{1}0\}$, γ-Al_2O_3 {440} and Si {220} reflections, as illustrated in Fig. 5-2, were measured to examine the in-plane epitaxial relationship. Six evenly spaced ZnO diffracted peaks verified that the hexagonal ZnO film was epitaxially grown on the γ-Al_2O_3/Si(111) composite substrate. Furthermore, two sets of peaks with 3-fold symmetry were observed in the γ-Al_2O_3 {440} ϕ-scan, revealing the cube-on-cube growth of γ-Al_2O_3 on Si and the coexistence of two in-plane rotated variants. The dominant one has the same angular position as that of Si {220}, A-type (111) orientated domain, and the minor one has its in-plane orientation rotated 60° from that of Si substrate, B-type domain [12]. These results suggest that the in-plane epitaxial relationship of this hetero-epitaxial system follows $\{10\bar{1}0\}_{ZnO} \parallel \{22\bar{4}\}_{\gamma-Al_2O_3}$ or $\{4\bar{2}\bar{2}\}_{\gamma-Al_2O_3} \parallel \{22\bar{4}\}_{Si}$,as shown in Fig. 5-3. In this geometry, the two-dimensional hexagonal unit cell of the γ-Al_2O_3 (111) plane is aligned with that of ZnO basal plane with its lattice constant equal to $\sqrt{2} \cdot a(\gamma\text{-}Al_2O_3) = 11.186$ Å, about 3.45 times larger than that of ZnO.

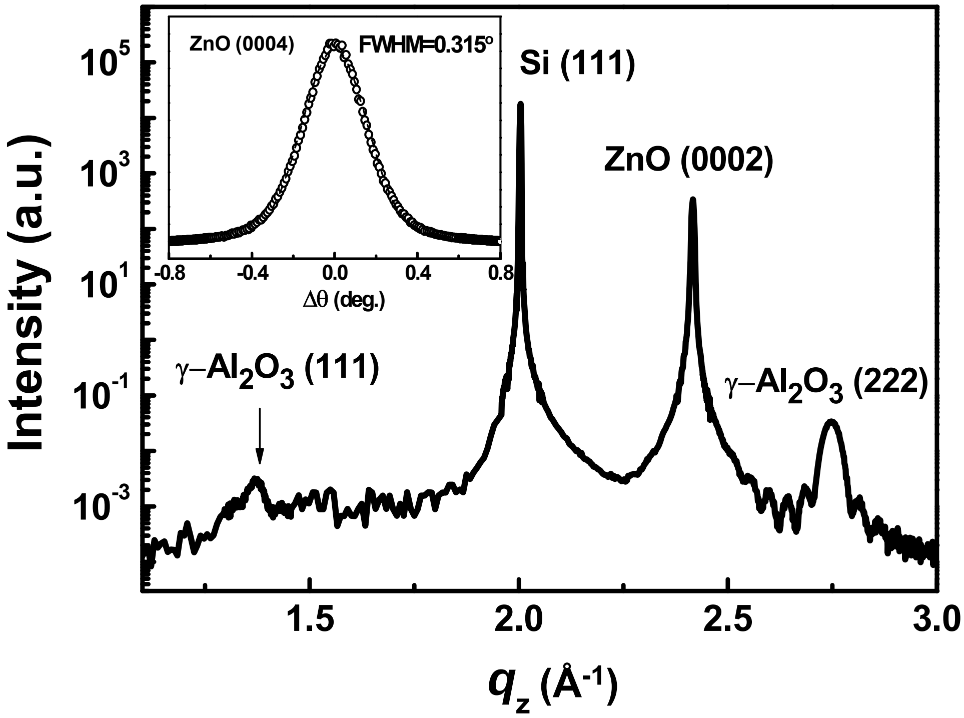

Fig. 5-1 XRD radical scan along surface normal of a 0.3 μm thick ZnO layer grown on the γ-Al_2O_3/Si(111) composite substrate. The inset illustrates a θ-rocking curve of ZnO (0004) reflection.

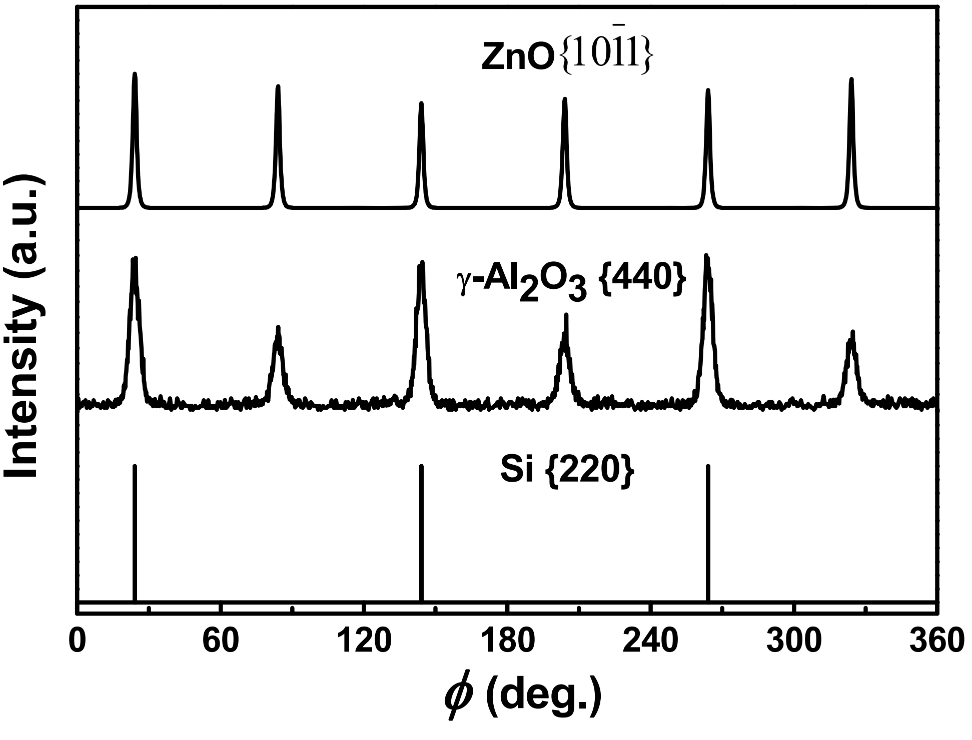

Fig. 5-2 The profiles of ϕ-scans across ZnO$\{10\bar{1}1\}$, γ-$Al_2O_3\{440\}$, and Si {220} reflections.

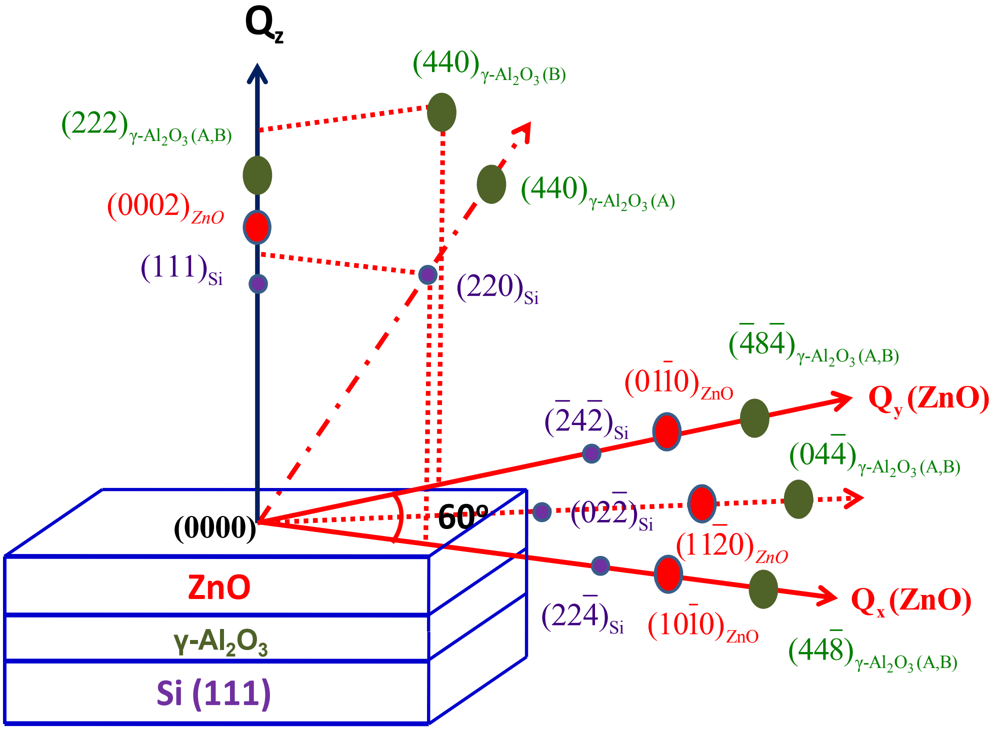

Fig. 5-3 The diagram of the reciprocal lattice of c-oriented ZnO film on Si(111) using γ-Al_2O_3 buffer layer.

Within the employed growth temperature range, all the samples exhibit the same structural characteristics with a small variation of less than 0.2% in ZnO lattice parameters. The lattice parameters of the ZnO layer grown at 300°C were measured to be a = 3.2528 Å and c = 5.1937 Å. As compared with the bulk values, a = 3.2438 Å and c = 5.2036 Å determined from a ZnO wafer, we found that all the ZnO epitaxial films experienced a tensile strain (~ 0.28%) in the lateral direction and were compressively stressed (~ 0.19%) along the surface normal. The mosaicity of the film against sample normal, i.e. the tilt angle, was characterized by measuring the θ-rocking curve of ZnO (0002) and (0004) diffraction peaks and fitting the Williamson and Hall plot. The small values of FWHM, 0.32~0.61° with the minimum obtained at 300°C, as shown in the inset of Fig. 5-1, manifest the good crystalline quality of ZnO epi-layers even for films as thin as 0.3 m. This value is comparable to that of ZnO epi-layers grown on nonoxide buffer layers, such as ZnS ($\Delta\theta = 0.25^{o}$, film thickness = 0.35 μm) [1], Al (0.35^{o}, 1 μm) [13], and 3C-SiC(1.11^{o}, 0.25 μm) [14]. The twist of the ZnO lattice against surface normal was determined from the peak width of azimuthal scans of in-plane and off-normal reflections. The obtained twist angle falls between $1.4\sim4.3^{o}$ depending on the growth conditions. From the structure of ZnO grown on different batches of buffer layer, we found that quality of ZnO epi-films is sensitive to the structural perfection of the γ-Al$_2$O$_3$ buffer layer. However, the lateral domain size and tilt/twist angles of the ZnO layers are always better than the underneath buffer layer and exhibit progressive improvement with increasing film thickness. It is worth noting that for a given film thickness an increase of $\Delta\theta$ is always accompanied by a decrease of $\Delta\phi$ and the ZnO epi-layers grown on γ-Al$_2$O$_3$ buffer at 300^{o}C always have the smallest tilt angle but the largest twist angle. This is different from ZnO grown on other substrates, such as c-plane sapphire, where tilt and twist angles always exhibit the same trend of increase/decrease with growth conditions [15]. This negative correlation between the tilt and twist angles allows us to separate their influence to the optical properties of the ZnO epi-layers, which will be discussed later.

5.3 Analysis of defect structures

Figure 5-4 shows the cross-sectional TEM bright-field image with **g** = $(0002)_{ZnO}$ under a two-beam contrast condition. The major defect structure in the ZnO layer is threading dislocations (TDs) seen as dark lines stemming from the ZnO/γ-Al_2O_3 interface with their dislocation lines primarily along the [0001] direction. The average TD density is about 3×10^{10} cm^{-2} as determined from the TEM image and XRD line width analyses, independently. Employing the two-beam condition with different g vectors (0002), $(11\bar{2}0)$ and $(11\bar{2}2)$ selected, we also found that TDs with edge component are predominant, with its density an order of magnitude higher than that of TDs with screw component. The high magnification TEM image taken at the interfacial region with $[10\bar{1}]_{Si}$ projection, shown in the inset of Fig. 5-4, reveals unequivocal interfaces of ZnO/γ-Al_2O_3 and γ-Al_2O_3/Si. No intermediate layer was observed in either interface. These results demonstrate that the growth of high quality ZnO epi-films on Si using an oxide buffer layer is possible and a γ-Al_2O_3 layer serves well as a template for subsequent ZnO growth.

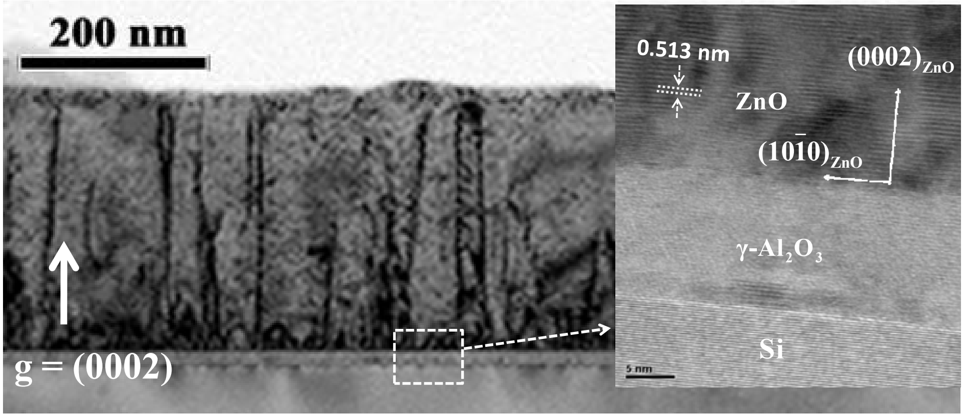

Fig. 5-4 Two-beam bright-field cross-sectional TEM micrographs of the ZnO film with g = (0002)$_{ZnO}$. The inset is the cross-sectional HR-TEM micrograph taken near the interfacial region with $[10\bar{1}]_{si}$ projection.

5.4 Optical properties

The optical properties of ZnO/γ-Al$_2$O$_3$/Si epi-layers were explored by using low temperature (LT) PL measurements at 15K. The PL spectra of ZnO films grown at 200 and 300 ^{o}C were displayed in Figs. 5-5 (a) and (b), respectively. Regardless of the growth temperature, the main features in PL spectra are common for all samples and can be divided into two categories: the near band edge (NBE) emission and deep-level emission (DLE). The assignments of NBE peaks were also shown in the insets of Fig. 5-5 (a) and (b). The peak at 3.375 eV was assigned as the free A-exction (FX$_A$) line; the binding energy of the corresponding A-exction was obtained to be 58.875 meV by fitting the temperature-dependent PL data using the Arrhenius expression. The dominant peak at ~ 3.359 eV and ~ 3.364 eV in NBE region were assigned to the recombination of excitons bound to neutral donor (D^{o}X)

[16] and their FWHM are 13.4 and 9.4 meV in (a) and (b), respectively. The $D^{o}X$ emission accompanied with single phonon ($D^{o}X$ -1LO) and dual phonon ($D^{o}X$ -2LO) replica appear at 3.288 and 3.215 eV. The peak at ~3.23 eV is attributed to the donor-acceptor pair (DAP) transition. Another strong line at 3.328 eV originates from the transition involving radiative recombination of an exciton bound to a neutral donor ($D^{o}X$) and leaving the donor in the excited state. This process is also known as the two-electron satellite (TES). We made such assignment based on the ratio of donor binding energy to exciton binding energy ~ 0.35 as reported by Teke *et al.* [16]. Similar to the E_2-high mode in Raman spectra of ZnO thin films [17], the position of the $D^{o}X$ is sensitive to the strain state of the films. The observed red shift of $D^{o}X$ energy relative to that of ZnO bulk wafer (3.365 eV), marked by the dashed lines in the insets of Fig. 5-5, consistent with the biaxial tensile strain determined by XRD measurements. The broad DLE peak centering at ~2.196 eV has its intensity ratio to the NBE feature (I_{DLE}/I_{NBE}) being 0.032 and 0.24 for 200 and 300°C grown samples. The DLE emission is attributed to the transitions involving point defects such as O vacancies, Zn interstitials as well as other surface defects and its strength is positively correlated with the defect density [18, 19]. Post growth annealing in O_2 atmosphere did lead to a significant reduction of DLE emission, indicating that O vacancies are a major source of DLE emission.

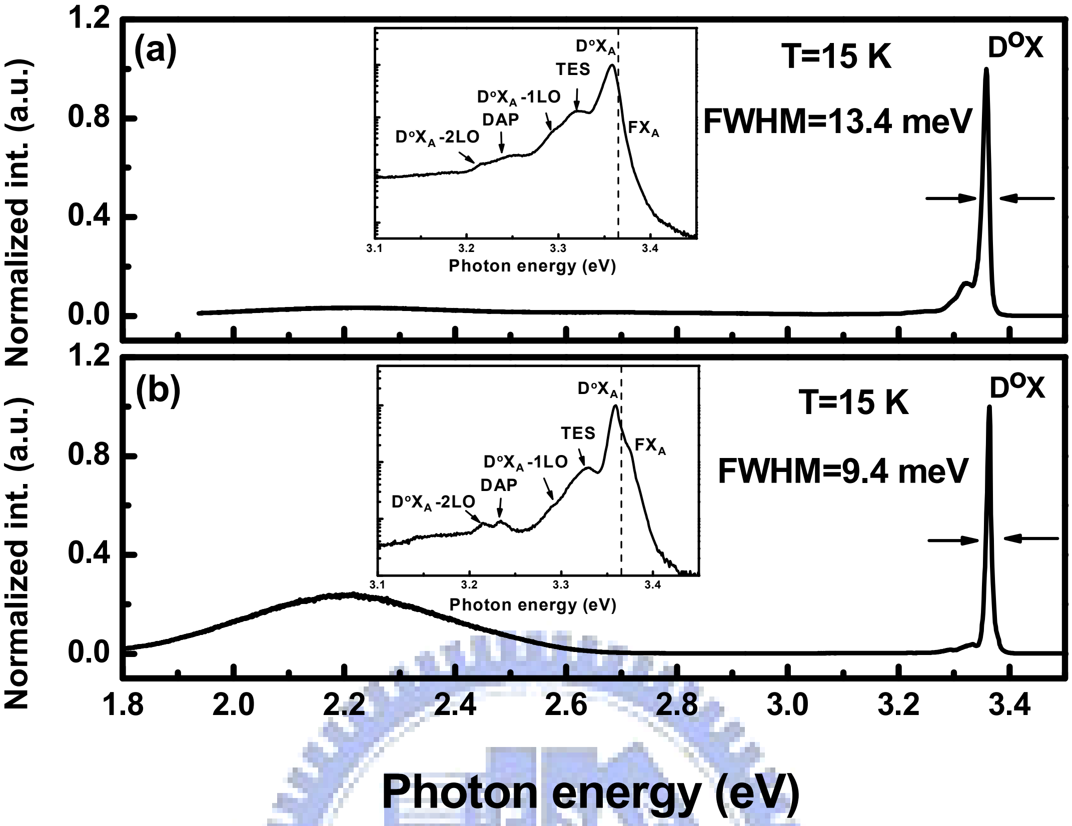

Fig. 5-5 Typically PL spectra measured at 15K for ZnO epi-layers deposited on γ-Al_2O_3/Si(111) at 200°C (a) and 300°C (b). The insets in (a) and (b) are the extended spectra of near-band-edge emission. The dashed lines mark the D°X peak position of bulk ZnO.

5.5 Correlated crystal structure with optical properties and carrier concentration

The brighter intensity and narrower line width of NBE and the low (I_{DLE}/I_{NBE}) intensity ratio are considered as signatures of better optical properties. Comparing the PL spectra of ZnO grown at 200 and 300°C, we found that the optical performance of ZnO grown at 300°C was better in the NBE but worse in the DLE region. We also observed that tilt/twist angle of sample grown at 300°C is smaller/larger than that grown at 200°C. Previous studies pointed out that tilt angle alone, which is coupled with the screw type TDs, is not sufficient to describe the crystalline quality of the ZnO films [15, 20]. Twist angle, which is a measure of edge type TD density, should be taken into consideration to account for the optical properties. The different trend of increase/decrease of the tilt and twist angles with growth conditions observed in this case allows us to independently examine the influence of edge and screw TDs.

The (I_{DLE}/I_{NBE}) ratio *vs.* $\Delta\phi_{(10\bar{1}1)}$, the FWHM of the azimuthal scan across ZnO off-normal $(10\bar{1}1)$ reflection, and the FWHM of NBE *vs.* $\Delta\theta_{(0002)}$, the FWHM of the rocking curve of (0002) specular reflection, are illustrated in Fig. 5-6 (a) and (b), respectively. Here $\Delta\phi_{(10\bar{1}1)}/\Delta\theta_{(002)}$ bears the same physical meaning as the twist/tilt angle and can be considered as a measure of the density of edge/screw TDs. In both figures, (I_{DLE}/I_{NBE}) ratio and FWHM of NBE exhibit monotonic increases with $\Delta\phi_{(10\bar{1}1)}$ and $\Delta\theta_{(0002)}$, respectively. In contrast, the distribution of (I_{DLE}/I_{NBE}) ratio scatters randomly with $\Delta\theta_{(0002)}$ and the line width of NBE didn't show clear correlation with $\Delta\phi_{(10\bar{1}1)}$, either. Evidently, the NBE emission is predominantly governed by the screw component of the TDs and the edge TDs play the key role in affecting the DLE intensity, as shown in Fig 5-7 (a) and (b). After exchanging abscissa of Fig. 5-7 (a) with (b), no clear correlation is observed, as plotted in Figure 5-8 (a) and (b). Our observations support the arguments that screw TDs can act as nonradiative centers in reducing the NBE emission intensity and the existence of edge TDs leads to aggregation of point defects due to stress field near the dislocation core resulting in the enhancement of DLE intensity [9, 21].

The electric properties of the ZnO/γ-Al_2O_3/Si samples were also investigated by Hall effect measurements (Ecopia Corporation HMS-3000 with 1 T magnet). The major carriers in ZnO layers are verified to be electrons, revealing the n-type nature of the ZnO layers, same as the usual undoped ZnO. The dependence of net carrier concentration and mobility on $\Delta\phi_{(10\bar{1}1)}$ and $\Delta\theta_{(0002)}$ were examined. The obtained mobility is in the order of a few tens cm^2/Vs and no obvious correlation between the carrier mobility and twist/tile angle was found. We also observed that the carrier concentration decreased with the increase of $\Delta\phi_{(10\bar{1}1)}$ but distributed randomly with $\Delta\theta_{(0002)}$, as plotted in Fig. 5-6 (a) and (b). This implies that the decrease of net carrier concentration is dominantly affected by the increasing density of edge TDs but is not remarkably influenced by the screw TDs, as shown in Fig. 5-7 (a) and (b). Similar phenomenon was also reported by D.G. Zhao *et al.* on GaN grown on c-plane sapphire by MOCVD, where the carrier concentration decreased with the increase of the FWHM of XRD $(10\bar{1}2)$ reflection [22, 23]. It is known that there exist many dangling bonds along the edge dislocation lines, and they can induce deep acceptor-like trap states which may capture the electrons from conduction band in n-type semiconductors [24, 25]. In the case of n-type GaN, the edge dislocation cores are normally negatively charged and the decrease of free electron concentration can be attributed to the compensation effect from the increasing acceptor levels introduced by the edge dislocations. In our case, SCM and CAFM measurement results presented in chapter 4 indicate the lower local carrier concentration and higher D_{it} in the boundary regions with high density of edge dislocations in ZnO grown in c-plane sapphire by the same method. Consequently, we ascribe the reduction of carrier concentration with increasing edge dislocation density to the compensation effect of the edge dislocation induced acceptor levels, similar to the case of n-type GaN. Edge type TDs seem to be more harmful to the optical and electric properties of ZnO as compared to screw type TDs. How to optimize growth parameters and/or develop new growth method to effectively cut down the density of TDs, especially the edge type ones, in ZnO epitaxial films is still an important issue in the prospective applications to photonic devices.

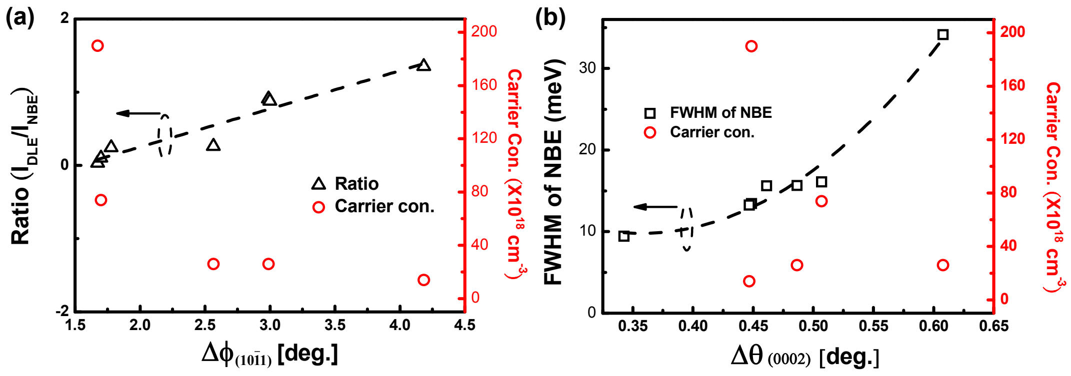

Fig. 5-6 The ratio (I_{DLE}/I_{NBE}) and net carrier concentration dependence of $\Delta\phi$ of ZnO $(10\bar{1}1)$ diffracted peak (a). The NBE width and net carrier concentration dependence of $\Delta\theta$ of ZnO (0002) diffracted peak (b). The dash curves were plotted to guide the eyes.

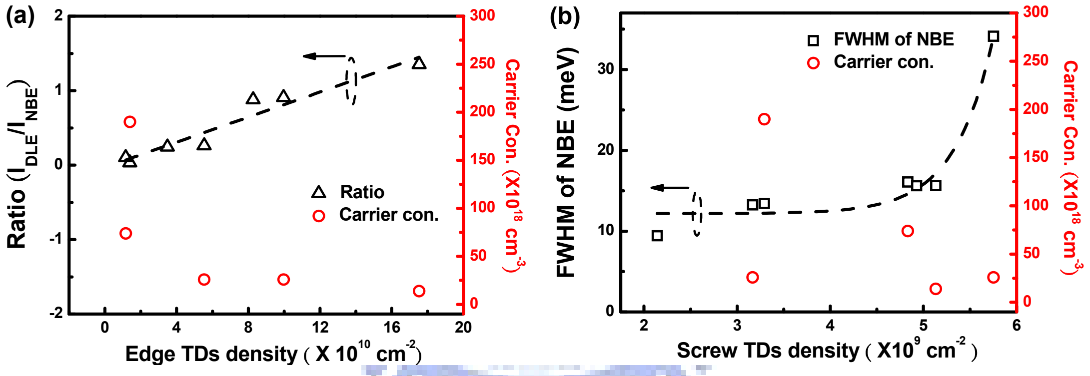

Fig. 5-7 The ratio (I_{DLE}/I_{NBE}) and net carrier concentration dependence of edge TDs density for pile-up model calculation (a). The NBE width and net carrier concentration dependence of screw TDs density (b). The dash curves were plotted to guide the eyes. [unpublished]

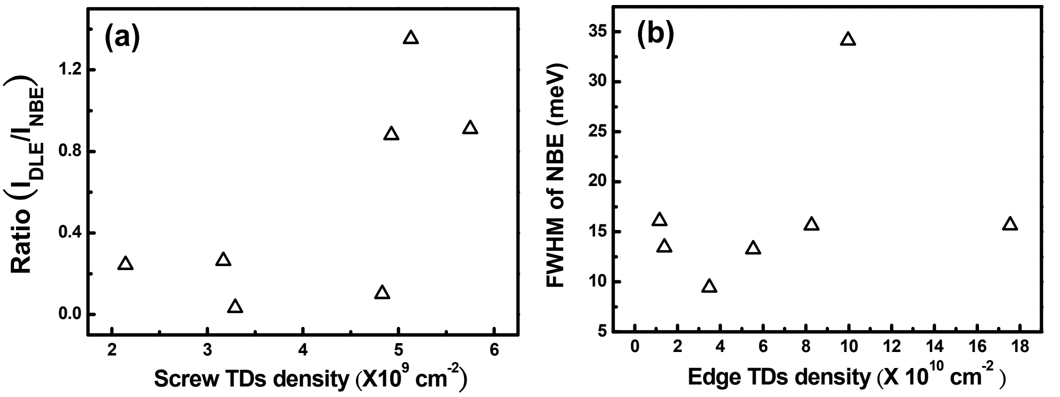

Fig. 5-8 After exchanging abscissa of Fig. 5-7 (a) with (b), the ratio (I_{DLE}/I_{NBE}) dependence of screw TDs density (a), The NBE width dependence of edge TDs density (b). [unpublished]

5.6 Summary

In this work, we have successfully grown high-quality ZnO epitaxial films by PLD on Si(111) substrate with a nano-thick γ-Al_2O_3 buffer layer. There exist two (111)-oriented γ-Al_2O_3 domains rotated 60° from each other relative to the surface normal. The in-plane epitaxial relationship between the wurtzite ZnO, cubic γ-Al_2O_3 and cubic Si follows $\{10\bar{1}0\}_{ZnO} \parallel \{22\bar{4}\}_{\gamma-Al_2O_3}$ or $\{4\bar{2}\bar{2}\}_{\gamma-Al_2O_3} \parallel \{22\bar{4}\}_{Si}$ as determined by XRD and TEM. The connection between the defect characteristics and optical properties of ZnO layer was established by correlating XRD and LT-PL results. Our results indicate that the (I_{DLE}/I_{NBE}) ratio and carrier concentration are dominantly affected by edge TDs and the line width of NBE emission is mainly related to screw TDs.

References

[1] Y. Z. Yoo, T. Sekiguchi, T. Chikyow, M. Kawasaki,T. Onuma, S. F. Chichibu, J. H. Song, and H. Koinuma, *Appl. Phys. Lett.* **84,** 502 (2004)

[2] C. C. Lin, S. Y. Chen, S. Y. Cheng, and H. Y. Lee, *Appl. Phys. Lett.* **84**, 5040 (2004).

[3] H. M. Cheng, H. C. Hsu, S. Yang, C.Y. Wu, Y. C. Lee, L. J. Lin and W. F. Hsieh, *Nanotechnology* **16**, 2882 (2005).

[4] M. Fujita, N Kawamoto, M Sasajima, and Y. Horikoshi, *J. Vac. Sci. Technol.* B **22**, 1484 (2004).

[5] X. N. Wang, Y. Wang, Z. X. Mei, J. Dong, Z. Q. Zeng, H. T. Yuan, T. C. Zhang, X. L. Du, J. F. Jia, Q. K. Xue, X. N. Zhang, Z. Zhang, Z. F. Li, and W. Lu, *Appl. Phys. Lett.* **90**, 151912 (2007).

[6] R. D. Vispute, V. Talyansky, S. Choopun, R. P. Sharma, T. Venkatesan, M. He, X. Tang, J. B. Halpern, M. G. Spencer, Y. X. Li, L. G. Salamanca-Riba, A. A. Iliadis , and K. A. Jones, *Appl. Phys. Lett.* **73**, 348 (1998).

[7] Ahmed Nahhas, Hong Koo Kim, and Jean Blachere, *Appl. Phys. Lett.* **78**,1511 (2001).

[8] Y. Oyama, J. Nishizawa, T. Kimura, and T. Tanno, *Phys. Rev.* B **74**, 235210 (2006).

[9] U. Bangert, A. J. Harvey, R. Jones, C. J. Fall, A. Blumenau, R. Briddon, M. Schreck, and F. Hörmann, *New J. Phys.* **6** 184 (2004).

[10] H. M. Ng, D. Doppalapudi, T. D. Moustakas, N. G. Weimann, and Eastman, *Appl. Phys. Lett.* **73** 821 (1998)

[11] J. Y. Shi, L. P. Yu, Y. Z. Wang, G. Y. Zhang, and H. Zhang, *Appl. Phys. Lett.* **80** 2293 (2002).

[12] R. T. Tung, and J. L. Batstone, *Appl. Phys. Lett.* **52**,1611 (1998).

[13] Y. Chen, F. Jiang, L. Wang, C. Zheng, Y. Dai, Y. Pu, and W. Fang, *J. Cryst. Growth* **275**, 486 (2005).

[14] J. Zhu, B. Lin, X. Sun, R. Yao, C. Shi, and Z. Fu Z, *Thin Solid Films* **478**, 218 (2005).

[15] W. R. Liu, W. F. Hsieh, C. H. Hsu, K.S. Liang, and F. S. S. Chien, *J. Appl. Cryst.* **40**, 924 (2007).

[16] A. Teke, Ü. Özgür, S. Dogan, X. Gu, H. Morkoç, B. Nemeth, J. Nause, and H. O. Everitt , *Phys. Rev.* B **70** ,195207 (2004).

[17] W. J. Shen, J. Wang, Q.Y. Wang, Y. Duan, and Y. P. Zeng, *J. Phys. D: Appl. Phys.* **39**, 269 *(2006).*

[18] Y. F. Chen, D. M. Bagnall, H. J. Koh, K. T. Park, K. Hiraga, Z. Zhu, and T. Yao, *J. Appl. Phys.* **84** ,3912 (1998).

[19] T. Onuma, S F. Chichibu, A. Uedono, Y. Z. Yoo, T. Chikyow, T. Sota, M. Kawasaki, and H. Koinuma, *Appl. Phys. Lett.* **85**, 5586 (2004).

[20] B. P. Zhang, Y. Segawa, K. Wakatsuki, Y. Kashiwaba, and K. Haga, *Appl. Phys. Lett.* **79**, 3953 (2001).

[21] J. H.You, and H. T. Johnson, *J. Appl. Phys.* **101**, 023516 (2007).

[22] D. G. Zhao, H. Yang, J. J. Zhu, D. S. Jiang, Z. S. Liu, S. M. Zhang, Y. T. Wang, and J. W. Liang, *Appl. Phys. Lett.* **89**, 112106 (2006)

[23] D. G. Zhao, D. S. Jiang, H. Yang, J. J. Zhu, Z. S. Liu, S. M. Zhang, J. W. Liang, X. Li, X. Y. Li and H. M. Gong, *Appl. Phys. Lett.* **88**, 241917 (2006).

[24] W. T. Read, *Philos. Mag.* **45**, 775 (1954).

[25] B. Podor, *Phys. Status Solidi* **16**, K167 (1966).

Chapter 6 Epitaxial ZnO on Si (111) using a Y_2O_3 buffer Layer

6.1 Introduction

Epitaxial growth of insulator layers on Si is of great importance in achieving Si on insulator (SOI) structures and for the long-range goal of three dimensional integrated circuits. Recently, Y_2O_3 has attracted great attentions because of its high dielectric constant, high conduction band offset, and thermodynamic stability with Si and is a promising candidate as an alternative gate dielectric [1-3]. Furthermore, the formation enthalpy of Y_2O_3 is larger in magnitude than that of SiO_2 and ZnO on thermal dynamics ($\Delta H_{Y_2O_3}$ = -1905.31 KJ/mole ΔH_{SiO_2} = -910.7 KJ/mole, and ΔH_{ZnO} = -350.5 KJ/mole) [4-5]. This implies the formation of an amorphous silica layer can be obstructed during nucleation stage of Y_2O_3 on Si substrate and provides a nice template for subsequent epitaxial growth. Therefore, the growth of high-quality ZnO on Y_2O_3/Si offers very attractive potential to harmonically incorporate ZnO optoelectronic devices in silicon based integrated circuits. In this chapter, we report the growth of high-quality epitaxial ZnO films by pulsed-laser deposition (PLD) on a Y_2O_3/Si (111) composite substrate and discuss the function of MDs at the interface. The nano-thick Y_2O_3 epi-layer serves not only as a buffer layer to ensure the growth of ZnO epi-film of high structural perfection but also as an insulator layer between

ZnO and Si. The structural properties of the ZnO/Y_2O_3/Si(111) hetero-epitaxial system was thoroughly examined by XRD and TEM. Superior optical characteristics of the ZnO film were verified by PL at room temperature (RT) and low temperature (LT).

6.2 Crystal structure

XRD radial scan (θ-2θ) along the surface normal of a 0.21 μm thick sample is shown in Fig. 6-1. The sharp peaks centered at 2.003 and 2.425 $Å^{-1}$ are Si (111) and ZnO (0002) reflections, respectively; the shoulder at 2.06 $Å^{-1}$ is attributed to Y_2O_3 (222) Bragg peak, revealing the cube-on-cube growth of Y_2O_3 on Si substrate. Additional oscillations observed in the radial scan are known as the thickness fringes, whose presence is an indication of sharp interfaces and good crystalline quality of the grown film. From the fringes period, we derived the thickness of the Y_2O_3 buffer layer to be ~9.6 nm. The fact that only the (0002) reflection of ZnO appears, together with Y_2O_3 (222) and Si (111) reflections, in Fig. 6-1 elucidates the grown ZnO layer is c-plane oriented. From ZnO (0002) peak width, we estimated the vertical coherence length about 0.20 μm indicating its structure maintains coherent almost over the entire film thickness. To examine the in-plane epitaxial relationship, we performed azimuthal cone scans (ϕ-scans) across the off-normal ZnO $\{10\bar{1}1\}$,

Y_2O_3 {440} and Si {220} reflections, as illustrated in Fig. 6-2.

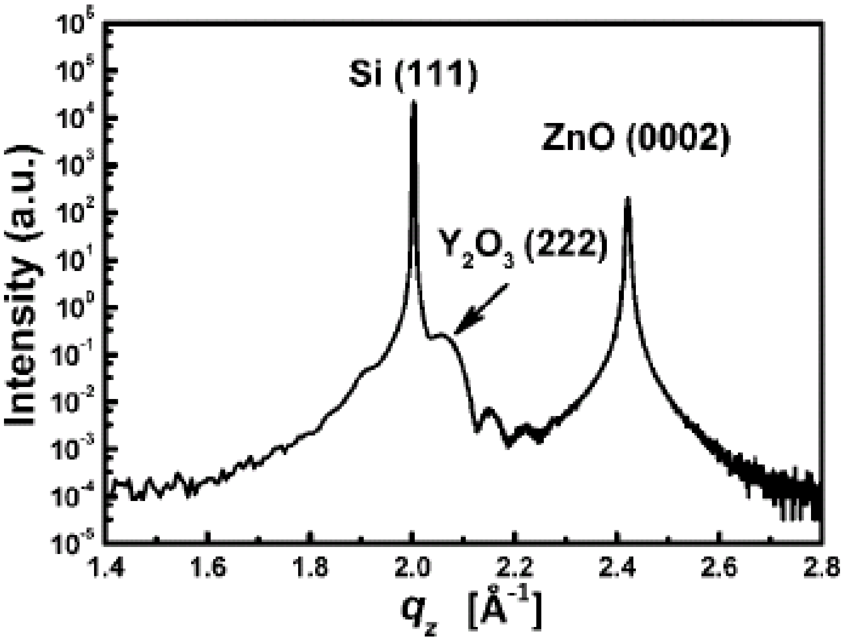

Fig. 6-1 XRD radical scan along surface normal.

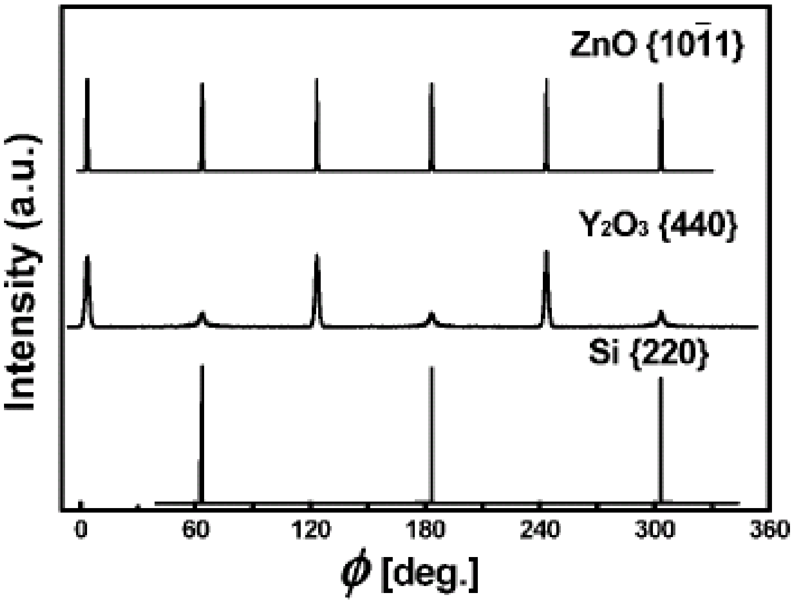

Fig. 6-2 ϕ-scan profiles across $\{10\bar{1}1\}_{ZnO}$, $\{440\}_{Y_2O_3}$, and $\{220\}_{Si}$ off-normal reflections.

In contrast to ZnO grown directly on Si (111), where completely random in-plane orientation was observed, the presence of six evenly spaced ZnO $\{10\bar{1}1\}$ peaks confirmed the epitaxial growth of hexagonal ZnO film on the Y_2O_3/Si (111) substrate. The zone axis associated with the (0001) and $(10\bar{1}1)$ reflections of ZnO is $[\bar{1}2\bar{1}0]$, while the zone axis corresponding to Y_2O_3 (001) and (440) planes is $[\bar{1}10]$. The coincidence in angular positions of ZnO $\{10\bar{1}1\}$ and Y_2O_3 {440} reflections, as shown in Fig. 6-2, reveals these two zone axes are aligned with each other. With the crystal symmetry taken into account, we determined the in-plane epitaixial relationship to be $<2\bar{1}\bar{1}0>_{ZnO} \| <10\bar{1}>_{Y_2O_3}$. Furthermore, it is worth noticing that two sets of 3-fold symmetric peaks with 180^{o} in-plane rotation from each other were observed in the Y_2O_3 {440} ϕ-scan, indicating the existence of two variants of Y_2O_3 on Si. The dominant one, B-type (111)-orientated domain with $[2\bar{1}\bar{1}]_{Y_2O_3} \| [\bar{2}11]_{Si}$, has its axes rotated 180^{o} about the surface normal from that of underlying Si and amounts over 86% in population; the minor one, A-type domain with $[2\bar{1}\bar{1}]_{Y_2O_3} \| [2\bar{1}\bar{1}]_{Si}$, has the identical orientation as Si substrate [2, 6]. Estimating from the line widths of radial and azimuthal scans across Y_2O_3 in-plane reflections, we obtained the average lateral domain size and twist angle of the ~9.6 nm thick Y_2O_3 buffer layer to be about 20.5 nm and 0.67°, respectively.

The lattice parameters of the ZnO layer are a = 3.258 Å and c = 5.182 Å as determined by fitting the positions of several Bragg reflections. As compared with the bulk values, a = 3.2439 Å and c = 5.2067 Å determined from a ZnO wafer, we found that the ZnO epitaxial film was tensily strained (0.45%) in the lateral direction and the lattice along the growth direction is correspondingly compressed by 0.42%. Cubic Y_2O_3 has a bixbyite structure, which can be described as a vacancy-ordered fluorite. Viewing along the [111] direction of Y_2O_3, the O sub-lattice in Y_2O_3 consists of two-dimensional defective hexagonal lattices stacking with ABC sequence along the [111] direction, as shown in Fig. 6-3(a), in which the filled circles denote O atoms and open circles represent O vacancies. The hexagonal unit cell has a lattice constant equal to $a(Y_2O_3)\cdot\sqrt{2}/4$ = 3.750 Å and its axes are aligned with the $<10\bar{1}>_{Y_2O_3}$ directions, identical to the axes in ZnO basal plane. This elucidates the ZnO lattice is aligned with the O sub-lattice in Y_2O_3, as illustrated in Fig. 6-3(b), similar to the case of ZnO grown on c-plane sapphire [7]. The lattice mismatch between ZnO and O sub-lattices in Y_2O_3 and in sapphire are -13.5% and 18.1%, respectively. The opposite sign of lattice mismatch may explain the tensile and compressive strain observed in ZnO layers grown on Y_2O_3 and sapphire, respectively.

6.3 Domain matching and interface engineering

For systems with such a large lattice mismatch, the well established lattice matching epitaxy (LME), where films grow by one-to-one matching of lattice constants or pseudomorphically across the film-substrate interface, is not the favorable mechanism. Instead, domain matching epitaxy (DME) [7], where integral multiples of lattice planes containing densely packed rows are matched across the interface, provides a nice description of the interfacial structure of these systems.

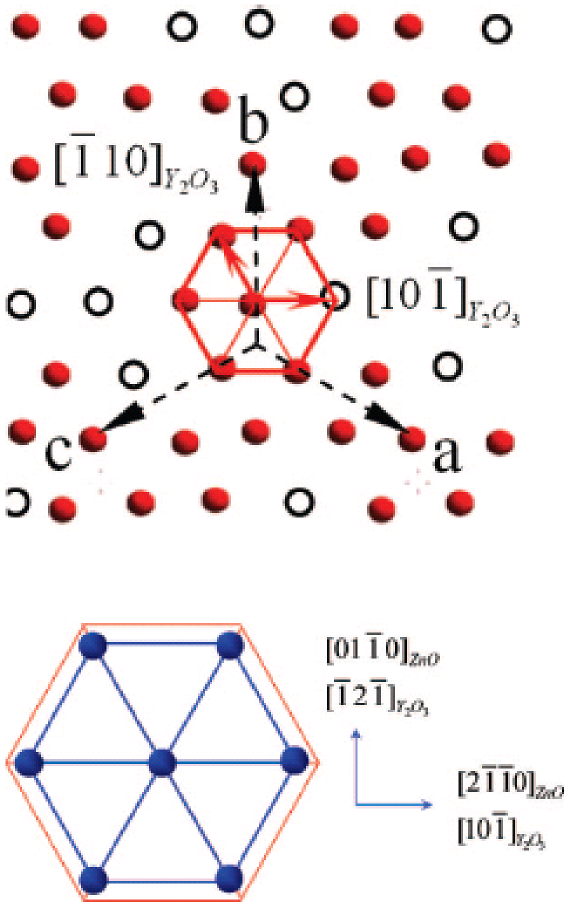

Fig. 6-3 (a) Schematic of atomic arrangement of O sub-lattice in Y_2O_3 (111) planes, where the filled circles are O atoms and the open circles denote O vacnacies. The dashed arrows are (111) projection of the basis vectors of Y_2O_3 cubic lattice. (b) Illustration of the lattice alignment of ZnO basal plane (small hexagon) with O sub-lattice in Y_2O_3 (large hexagon).

The planar spacing ratio of $(11\bar{2}0)_{ZnO}$ to parallel $(4\bar{4}0)_{Y_2O_3}$, which coincides with the $(11\bar{2}0)$ planes of O sub-lattice in Y_2O_3, 1.6292/1.875 falls between 6/7 and 7/8; this implies a matching of 7(8) planes of ZnO with 6(7) planes of Y_2O_3 across the interface along this direction. The large lattice mismatch is thus accommodated by the misfit dislocations localized at the interface with a periodicity of 6(7) times of $(4\bar{4}0)_{Y_2O_3}$ inter-planar spacing, leading to a significant reduction of residual strain down to ~1%. To verify this interfacial structure, we performed cross-sectional TEM measurements. Figure 6-4(a) is the TEM micrograph along $[11\bar{2}]_{Si}$ projection which shows atomically sharp ZnO/Y_2O_3 and Y_2O_3/Si interfaces; no intermediate reaction layer is observed in both interfaces. The periodic contrast variation along the ZnO/Y_2O_3 interface with an average spacing of ~1.2 nm found in the high resolution TEM images, shown in Fig. 6-4(b), was attributed to the misfit dislocations induced strain field. The nearly periodically arranged extra $(11\bar{2}0)_{ZnO}$ half planes with a spacing of 6 or 7 $(4\bar{4}0)_{Y_2O_3}$ planes are clearly seen in the Fourier filtered image shown in Fig. 6-4(c); this confirms the DME of ZnO on Y_2O_3 (111).

To further characterize the crystalline quality of the grown film, θ-rocking curves and radial scans of ZnO normal reflections (000n) with n = 2 and 4 and in-plane reflections ($n0\bar{n}0$) where n = 1, 2 and 3 were measured. Plotting the rocking curve width $\Delta\theta$ versus the diffraction order n, an analog to the Williamson and Hall plot, we obtained the tilt and twist angle of the film to be 0.27° and 0.52°, respectively. The line widths of the radial scans across ZnO surface reflections yield its lateral domain size of ~110 nm. It is interesting that the twist angle and domain size of the ZnO layer are significantly better than that of the Y_2O_3 buffer layer, 0.67° and 20.5 nm, even though we do see the positive correlation between the structure perfection of buffer layer and that of the ZnO layer. Be aware that both the crystalline quality and optical properties of ZnO epi-layers are known to be significantly improved with increasing film thickness [8]. For a film as thin as 0.21 μm, the obtained tilt angle approaches that of ZnO epi-films of similar thickness grown on c-plane sapphire (0.05°) and its twist angle is even smaller than the later films (0.58°) [9], demonstrating the high crystalline quality of the ZnO films grown on Y_2O_3.

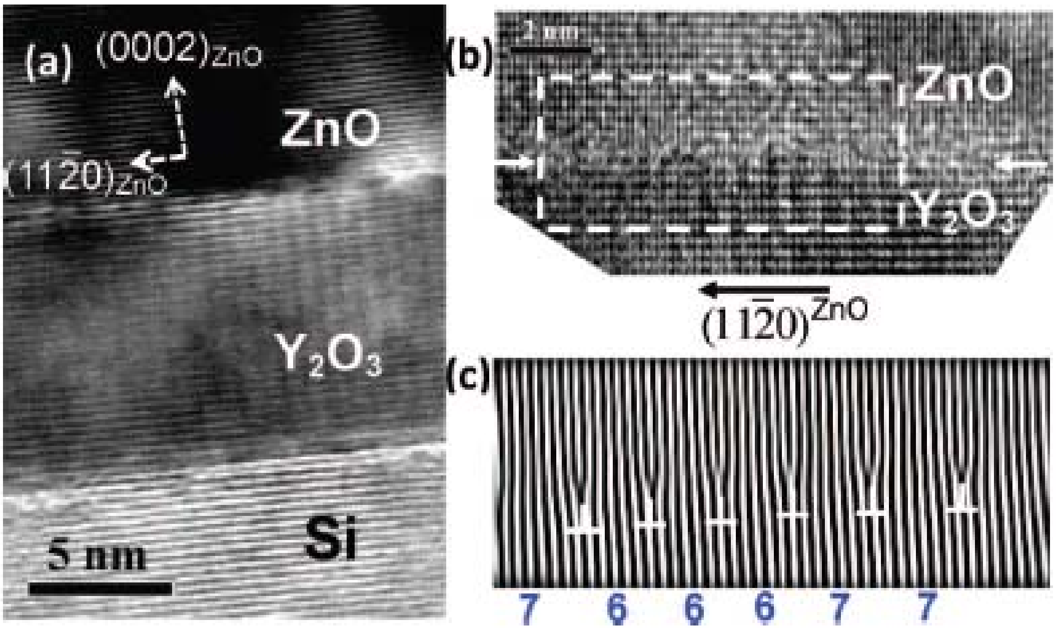

Fig. 6-4 (a) Cross-sectional TEM micrograph recorded along $[11\bar{2}]_{Si}$ projection. The high resolution image of the ZnO/Y_2O_3 interface is shown in (b). The Fourier filtered image of the area enclosed by the dashed rectangle in (b) is displayed in (c), on which the number of $(4\bar{4}0)_{Y_2O_3}$ planes between adjacent extra $(11\bar{2}0)_{ZnO}$ half planes are marked below.

6.4 Photoluminescence

We performed PL measurements at both 300 K (RT) and 13 K (LT) to examine the optical performance of the 0.21 μm thick ZnO films. The RT-PL spectrum, shown in Fig. 6-5(a), exhibits a very weak deep-level emission (DLE) near 2.2 eV and a narrow near-band edge (NBE) emission at 3.296 eV, that is dominated by the free exciton emission. Both low DLE signals as well as the narrow and intense NBE emission are signatures of good optical performance. In comparison with the ZnO films grown on Si using other buffer layers such as LT-ZnO (NBE FWHM/film thickness: 130 meV/0.7 μm) [10], ZnS (>100 meV/0.35 μm) [11], and Mg/MgO (95 meV/1 μm) [12], our ZnO film exhibits equally good or even better optical quality (100 meV/0.21 μm). Its performance is also comparable to ZnO films grown on c-plane sapphire (117 meV/0.4 μm) [13] and CaF_2 (~98 meV/1.3 μm) [14].

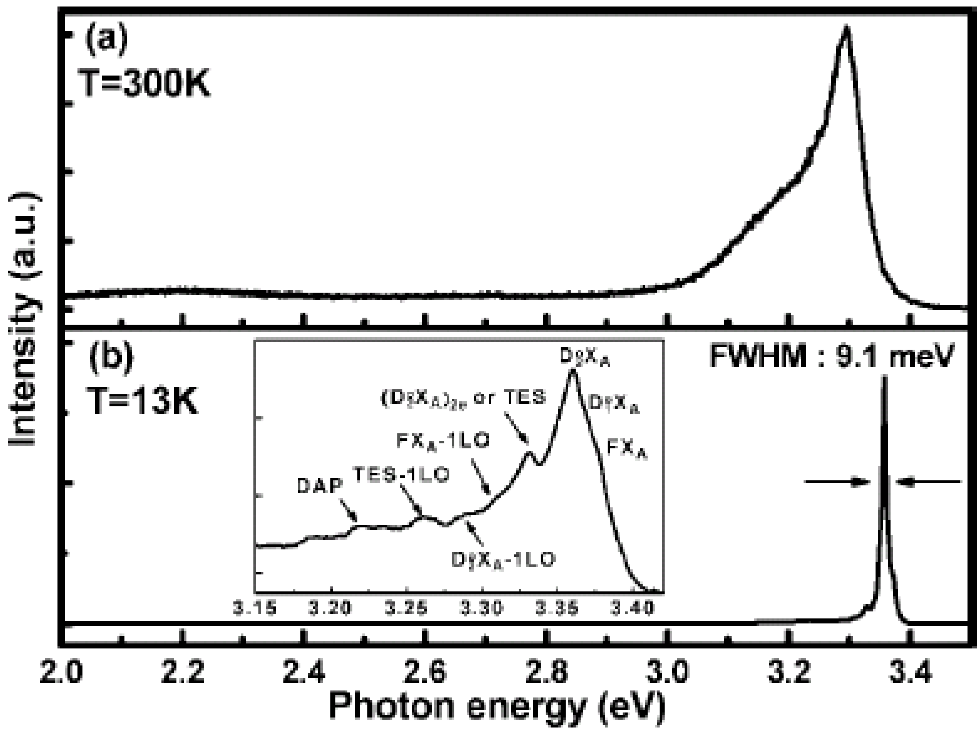

Fig. 6-5 PL spectra of the ZnO film on Y_2O_3/Si (111) measured at 300 K (a) and 13 K (b). The inset is the extended spectrum of NBE emission in (b).

Figure 6-5(b) illustrates the LT-PL spectrum and the enlarged spectrum of the NBE region together with the peak assignment is shown in the inset. The peak for NBE emission shifts to the low energy side from LT to RT, shown in Fig. 6-5, is due to the decrease of the band gap caused by the change of lattice constants or interaction with phonon [15, 16]. The dominant LT luminescence line at 3.358 eV with a FWHM of ~9.1 meV and the lines around 3.368 eV were ascribed to the recombination of A-exciton bound to the neutral donors, $D^o{}_2X_A$ and $D^o{}_1X_A$, respectively. By fitting the temperature-dependent intensity variation of the free A-exciton (FX_A) line at 3.371 eV using the Arrhenius expression [17], we obtained the binding energy of A-exciton 56.57 ± 6.53 meV, in good agreement with the 60 meV for bulk ZnO crystal. The other strong line at 3.329 eV $(D^o{}_2X_A)_{2e}$ originates from the transitions involving radiative recombination of an exciton bound to a neutral donor ($D^o{}_2X_A$) and leaving the donor in the excited state, also known as two-electron satellite (TES). We made such assignment based on the ratio of donor binding energy to exciton binding energy ~ 0.34 as reported by Teke *et al* [18]. The FX_A, $D^o{}_2X_A$ and TES emission accompanied with single phonon (FX_A-1LO, $D^o{}_2X_A$-1LO and TES-1LO) replica were observed at 3.301, 3.288 and 3.26 eV, respectively, and the peak at ~3.22 eV is the donor-acceptor pair (DAP) transition. These results demonstrated the superior optical properties of the ZnO thin film on Si using a Y_2O_3 buffer layer.

6.5 Summary

In conclusion, high quality c-plane ZnO epitaxial films have been successfully grown by pulsed-laser deposition on Si (111) substrates with a thin Y_2O_3 buffer layer. Two (111) oriented domains with 180° in-plane rotation exist in the Y_2O_3 buffer layer and the B-type orientation domain prevails over the A-type one. The in-plane epitaxial relationship between the wurtzite ZnO and cubic Y_2O_3 follows $<2\bar{1}\bar{1}0>_{ZnO} \| <10\bar{1}>_{Y_2O_3}$. The growth of ZnO on Y_2O_3 can be well described by domain matching epitaxy. The photoluminescence spectra of ZnO epi-films exhibit superior optical properties at room temperature even for films of thickness as thin as 0.21 μm. Our results demonstrate that the Y_2O_3 layer well serves as a template for integrating ZnO based optoelectronic device with Si substrate.

References

[1] M. Hong, J. P. Mannaerts, J. E. Bowers, J. Kwo, M. Passlack, W-Y. Hwang, and L. W. Tu, *J. Cryst. Growth* **175/176**, 422 (1997).

[2] C. W. Nieh, Y. J. Lee, W. C. Lee, Z. K. Yang, A. R. Kortan, M. Hong, J. Kwo, and C.-H. Hsu, *Appl. Phys. Lett.* **92**, 061914 (2008).

[3] J. Kwo, M. Hong, A. R. Kortan, K. L. Queeney, Y. J. Chabal, J. P. Mannaerts, T. Boone, J. J. Krajewski, A. M. Sergent and J. M. Rosamilia, *Appl. Phys. Let*t. **77**, 130 (2000).

[4] A. Nahhas, H. K. Kim, and Blachere, *J. Appl. Phys. Lett.* **78**, 1511 (2001).

[5] J-J Liang, A. Navrotsky, T. Ludwig, H. J. Seifert, and F. Aldinger, *J. Mater. Res.* **14**, 1181 (1999).

[6] R. T. Tung, J. C. Bean, J. M. Gibson, J. M. Poate, and D. C. Jacobson, *Appl. Phys. Lett.* **40**, 684 (1982).

[7] J. Naraya, and B. C. Larson , *J. Appl. Phys.* **93**, 278 (2003).

[8] E. S. Shim, H. S. Kang, J. S. Kang, J. H. Kim, and S. Y. Lee, *Appl. Surf. Sci.* **186**, 474 (2002).

[9] W.-R. Liu, W. F. Hsieh, C.-H. Hsu, Keng S. Liang and F. S.-S. Chien, *J. Appl. Cryst.* **40**, 924 (2007).

[10] F. X. Xiu, Z. Yang, D. T. Zhao, J. L. Liu, K. A. Alim, A . A. Balandin, M. E. Itkis, and R. C. Haddon, *J. Crys. Growth* **286, 61 (**2006).

[11] Y. Z. Yoo, T. Sekiguchi, T. Chikyow, M. Kawasaki, T. Onuma, S. F. Chichibu, J. H. Song, and H. Koinuma, *Appl. Phys. Lett.* **84**, 502 (2004).

[12] X. N. Wang, Y. Wang, Z. X. Mei, J. Dong, Z. Q. Zeng, H. T. Yuan, T. C. Zhang, X. L. Du, J. F. Jia, Q. K. Xue, X. N. Zhang, Z. Zhang, Z. F. Li and W. Lu, *Appl. Phys. Lett.* **90**, 151912 (2007).

[13] Y. F. Chen, D. M. Bagnall, H. J. Koh, K. T. Park, K. Hiraga, Z. Zhu, and T. Yao, *J. Appl. Phys.* **84**, 3912 (1998).

[14] H. J. Ko , Y F. Chen, Z. Zhu, and T. Yao, *Appl. Phys. Lett.* **76**, 1905 (2000).

[15] H. C. Hsu, C. S. Cheng, C. C. Chang, S. Yang, C. S. Chang, and W. F. Hsieh, *Nanotechnology* **16**, 297 (2005).

[16] Lijun Wang, and N. C. Giles, *J. Appl. Phys.* **94**, 973 (2003).

[17] D. S. Jiang, H. Jung, and K. J. Ploog, *Appl. Phys.Lett.* **64**, 1371(1988).

[18] A. Teke, Ü. Özgür, S. Dogan, X. Gu, H. Morkoç, B. Nemeth, J. Nause, and H. O. Everitt , *Phys. Rev.* B **70** ,195207 (2004).

Chapter 7 Conclusions and Prospects

7.1 Conclusions

In this dissertation, high-quality c-oriented ZnO film has been epiaxially grown by utilizing PLD on the sapphire (0001), and Si (111) substrates with a nano-thick γ-Al_2O_3 or Y_2O_3 buffer layer, respectively. XRD results show a 30° offset between the $\{20\bar{2}0\}$ reflections of ZnO and sapphire verifies the in-plane epitaxial relationship of $[10\bar{1}0]$ sapphire || $[11\bar{2}0]$ ZnO and $[11\bar{2}0]$sapphire || $[01\bar{1}0]$ZnO; the great disparity of X-ray diffraction line widths between the normal and in-plane reflections reveals the specific threading dislocation (TD) geometry of ZnO. The calculated TDs densities from XRD and TEM indicate most TDs are pure edge dislocations. From a combination of scattering and microscopic results, it is found that the TDs are not uniformly distributed in the ZnO films, but the ZnO films consist of columnar epitaxial cores surrounded by annular regions of edge threading dislocations at a large density. The shift of flatband voltage and the raise of potential barrier at the aggregation of TDs observed by scanning capacitance microscope and conduction atomic force microscope were attributed to the interface trap densities caused by the existence of high-density edge threading dislocations. On the other hand, because the distribution of the screw TDs is much less than that of the edge TDs, we cannot identify the location of the screw TDs and their electrical properties.

The structural analysis of c-oriented ZnO epitaxial films on Si(111) substrates with a thin γ-Al_2O_3 buffer layer reveals that epitaxial γ-Al_2O_3 buffer layer consists of two (111) oriented domains rotated 60^o from each other against the surface normal and the in-plane epitaxial relationship among ZnO layer, γ-Al_2O_3 buffer and Si buffer follows $(10\bar{1}0)_{ZnO} \parallel \{22\bar{4}\}_{\gamma-Al_2O_3}$ or $\{4\overline{2}\overline{2}\}_{\gamma-Al_2O_3} \parallel \{22\bar{4}\}_{Si}$. Studies on the crystalline quality and optical properties of ZnO epi-layers by XRD and PL measurements clearly indicate the intensity ratio of deep-level emission (DLE) to near-band edge emission (NBE) of ZnO films correlates with the width of ϕ–scan across off-normal reflection and the NBE linewidth is strongly dependent on the width of ZnO (0002) rocking curve. These observations manifest that the (I_{DLE}/I_{NBE}) ratio is dominantly affected by edge TDs and the line width of NBE emission is mainly related to screw TDs.

Both high-quality structural and optical properties of ZnO epi-film on Si (111) substrates using a nano-thick high-*k* oxide Y_2O_3 buffer layer was verified by XRD, TEM, and PL measurements. The nano-thick Y_2O_3 epi-layer serves not only as a buffer layer to ensure the growth of ZnO epi-film of high structural perfection but also as an insulator layer between ZnO and Si. Determined by XRD and TEM the epitaxial relationship between ZnO and Y_2O_3 follows $(0001) < 2\bar{1}\bar{1}0 >_{ZnO} \parallel (111) < 10\bar{1} >_{Y_2O_3}$. ZnO lattice aligns with the hexagonal oxygen (O) sub-lattice in Y_2O_3 and the interfacial structure can be well described by domain matching epitaxy with 7 or 8 ZnO $\{11\bar{2}0\}$ planes matching 6 or 7 $\{4\bar{4}0\}$ planes of Y_2O_3; the large lattice mismatch is thus accommodated by the misfit dislocations (MDs) localized at the interface with a periodicity of 6(7) times of $(4\bar{4}0)_{Y_2O_3}$ inter-planar spacing, leading to a significant reduction of residual strain. Superior photoluminescence were obtained even for ZnO-films as thin as 0.21μm. Our results demonstrate that the Y_2O_3 layer well serves as a template for integrating ZnO based optoelectronic devices with Si substrate.

In all three studied systems, the lattice of ZnO is always aligned with the hexagonal O sub-lattice in the oxide layer underneath. The lattice constant a_O of 2D hexagonal oxygen sub-lattice are 2.75, 2.80, 3.75 Å for sapphire, γ-Al_2O_3 and Y_2O_3, respectively. As compared with the lattice constant a of ZnO (3.249 Å), compressive strain along in-plane direction is expected for ZnO epi-film grown on sapphire (0001) and γ-Al_2O_3 (111). In contrast, the expected lateral strain is tensive for ZnO epi-film on Y_2O_3 (111). However, compressive lateral strain is only observed for ZnO epi-layers grown on sapphire. On both γ-Al_2O_3 and Y_2O_3 buffer layers, ZnO epi-films bear tensile strain. In fact, for ZnO epi-film grown on Si(111) using other oxide buffer layers, including Gd_2O_3, and Y_2O_3 doped HfO_2, all ZnO epi-film suffers tensile strain along in-plane direction. Moreover, high density of MDs at

ZnO/oxide-buffer interface should accommodate most of the strain caused by lattice mismatch. It is noted that the thermal expansion coefficient of ZnO ($\alpha \sim 4\text{-}6.5 \times 10^{-6}$ K^{-1}) is less than that of sapphire (8×10^{-6} K^{-1}) but larger than that of Si ($2.6\text{-}3.6 \times 10^{-6}$ K^{-1}). The trend agrees with the observed strain state of ZnO layer grown on sapphire and Si. This observation strongly suggests that the strain of the ZnO-epi layers is dictated by the thermal stress built up during the post-growth cooling. Because of the nano-thickness of the employed buffer layers, the influence coming from the buffer is negligible in these cases.

From these studies, we concluded that the major structural defect for ZnO epi-films on sapphire(0001), γ-Al_2O_3/Si(111), or Y_2O_3 /Si(111) substrates is TDs. Both XRD and TEM results indicate most TDs belong to pure edge dislocations. Table 7-1 summarizes the influence of the two types of TDs on the electrical and optical properties of ZnO epitaxial films. As for the pratical applications of ZnO-based photoelectronic devices, the ZnO/sapphire(0001) system is still the better choice for LED because of low TDs density and high otpical performance. However, considering the cost and the potential of integrating with well-established Si electronics for active and inactive photoelectronic devices on one chip, the depositon of ZnO epi-fim on Si has its unique merit. The ZnO grwon on Si(111) with a Y_2O_3 buffer layer is the more favroable choice than using a γ-Al_2O_3 buffer layer because the better crystalline quality and otpical performance.

Recently, the selective growth methods, such as epitaxial lateral overgrowth [1] and Pendeo epitaxy [2], where epitaxial layer is deposited on the pattern substrate, have attracted much attention becasue of the effective reduction of TDs. Therefore, desirability of deposited ZnO on patterned substrates will be an important approach to further eliminate TDs for the future applications of ZnO thin films.

Table 7-1. The influence of TDs on electrical and optical properties of ZnO epitaxial film in this studies

TDs type	Electrical property	Optical property
Screw TDs	undetermined	Degradation of PL width at NBE
Edge TDs	Extra negative charge due to D_{it}, nonconductive, lower carrier concentration	Enhancement of PL intensity at DLE

7.2 Prospects

In the development of ZnO-based optoelectronic devices, it is necessary to synthesize both high-quality *n*- and *p*-type ZnO films. The *n*-type ZnO is easily available even without any doping; however the fabrication of *p*-type ZnO is difficult due to the self-compensation effect from native defects. Known acceptors in ZnO include group-I elements such as lithium (Li) [3–5], Na and K, copper (Cu) [6], silver (Ag) [7], Zn vacancies and group-V elements such as N, P and As [8]. It has been believed that the most promising dopants for *p*-type ZnO are the group-V elements, although theory suggests some difficulty in achieving a shallow acceptor level. Recently, another *p*-type doping mechanism was proposed for group-V elements (P and As) [9]. P and As substitute Zn sites, forming a donor, then it induces two Zn-vacancy acceptors as complex form (P_{Zn}–$2V_{Zn}$ or As_{Zn}–$2V_{Zn)}$ [10, 11]. However, the choice of *p*-type dopant and growth technique remains controversial and the reliability of *p*-type ZnO and the doping mechanism are still a subject of debate.

Recently, we found that as time elapsed the electric characteristics of impurity (Li and N) doped *p*-type ZnO films with hole carriers gradually changed to *n*-type with electron carriers, the same as that of intrinsic ZnO. The mechanism of this electrical transition is crucial to the fabrication of *p*-type ZnO layer and still unknown. Therefore, it's important to understand the mechanism driving the decay of hole-carriers, which is crucial for the growth of stable *p*-type ZnO layer.

Bose-Einstein condensation (BEC) of an ideal gas of bosons has been the subject of intense study in excitonic and atomic systems. Excitons and biexcitons are bosons at low densities. Ideal bosons exhibit a so-called Bose-Einstein condensation at sufficiently low temperature and high density. BEC is a macroscopic population of one state in ***k*** -space, generally $\boldsymbol{k} = 0$. The appearance of an excitonic condensed phase in bulk crystals and quantum-well (QW) structures has been the major subject: Experiments on Cu_2O are considered to be quite promising [12-14]. In GaAs/AlAs coupled QW's, an anomalous transport behavior of indirect excitons under high magnetic fields, which suggests excitonic superfluidity, was reported [15, 16]. A possibility of the condensation of weakly localized excitons in GaAs/$Al_xGa_{1-x}As$ double QW's was experimentally proposed [17]. With the advent of semiconductor QWs, the possibility of observing the quantum statistics of bosons in two-dimensional systems has been raised. An interesting situation of Bose-Einstein statistics in a QW was reported by Kim and Wolfe [18: a two-component gas system of excitons and biexcitons. They showed theoretically and experimentally that a well-known square law of the density relation between excitons and biexcitons is modified by Bose-Einstein statistics. Assuming thermal equilibrium between excitons and biexcitons, there exists a situation, in which the equilibrium chemical potential (μ) comes close to the biexciton energy per electron-hole pair $E_{\mathrm{BEX}}/2$, i.e., $E_{\mathrm{BEX}}/2 - \mu \leq kT$, where $E_{\mathrm{BEX}}/2$, is lower than the exciton energy (E_{EX}) by a half of the biexciton binding energy. In such a situation, the biexciton density is governed by the strongly increasing part of the Bose-Einstein distribution function, while a saturation of the exciton density occurs, leading to the appearance of a threshold-like increase of the biexciton density. This behavior can be understood from Bose-Einstein statistics of the exciton-biexciton system. It was experimentally demonstrated from time-resolved PL spectra in the decay processes of excitons and biexcitons in a GaAs QW [18] and GaAs/AlAs superlattice [19] at a bath temperature of 2 and 5 K, respectively. Therefore, time-resolved PL measurements are capable of investigating BEC effect for the bosons. However, there are no reports to our knowledge on the phenomena with a BEC of exciton-biexciton in ZnO-based structures. The precise information of the exciton-biexciton density relationship at various excitation powers and bath temperatures estimated from the line-shape analysis of time-resolved PL spectra will be a long-term goal.

References

[1] H. Marchand, N. Zhang, L. Zhao, Y. Golan, S. J. Rosner, G. Girolami, P. T. Fini, J. P. Ibbetson, S. Keller, S. DenBaars, J. S. Speck, and U. K. Mishara, *MRS Internet J. Nitride Semicond. Res.* **4**, 2 (1999).

[2] K. Linthicum, T. Gehrke, D. Thomson, E. Carlson, P. Rajagopal, T. Smith, D. Batchelor, and R. Davis, *Appl. Phys. Lett.* **75**, 196 (1999).

[3] O. F. Schirmer and D. Zwingel, *Solid State Commun.* **8** 1559 (1970).

[4] O. F. Schirmer, *J. Phys. Chem. Solids* **29** 1407 (1968).

[5] A. Valentini, F. Quaranta, M. Rossi, and G. Battaglin, *J. Vac. Sci. Technol.* A **9** 286 (1991).

[6] Y. Kanai, *Jpn. J. Appl. Phys., Part* 1 **30** 703(1991).

[7] Y. Kanai, *Jpn. J. Appl. Phys., Part* 1 **30** 2021(1991)

[8] D. C. Look, D. C. Reynolds, C. W. Litton, R. L. Jones, D. B. Eason, and G. Cantwell, *Appl. Phys. Lett.* **81**, 1830 (2002).

[9] M. Joseph, H. Tabata, H. Saeki, K. Ueda, and T. Kawai. *Physica* B **302–303** 140 (2001).

[10] W. J. Lee, J. G. Kang, and K. J. Chang, *Phys. Rev.* B **73** 024117 (2006).

[11] S. Limpijumnong, S. B. Zhang, S. H. Wei, and C. H. Park, *Phys. Rev. Lett.* **92** 155 (2003).

[12] D. W. Snoke, J. P. Wolfe, and A. Mysyrowicz, *Phys. Rev.* B 41, 11 171 (1990).

[13] E. Fortin, S. Fafard, and A. Mysyrowicz, *Phys. Rev. Lett.* **70**, 3951 (1993).

[14] J. L. Lin and J. P. Wolf, Phys. *Rev. Lett.* **71**, 1222 (1993).

[15] L. V. Butov, A. Zrenner, G. Abstreiter, G. Bo¨hm, and G. Weimann, *Phys. Rev. Lett.* **73**, 304 (1994).

[16] L. V. Butov and A. I. Filin, *Phys. Rev.* B **58**, 1980 (1998).

[17] E. S. Moskalenko, V. V. Krivolapchuk, and A. L. Zhmodikov, Fiz. Tverd. Tela (St. Petersburg) **42**, 1492 (2000) [*Phys. Solid State* **42**, 1535 (2000).]

[18] J. C. Kim and J. P. Wolfe, *Phys. Rev.* B **57**, 9861 (1998).

[19] H. Ichida and M. Nakayama, *Phys. Rev.* B **63**, 195316 (2001).

劉維仁簡歷（Vita）

基本資料

姓名：劉 維 仁（Wei-Rein Liu）

性別：男

出生年月日：1972 年 11 月 09 日

籍貫：花蓮縣

永久通訊處：桃園縣八德市建國路 471 巷 2 弄 2 號

Email: wereinliu.eo92g@nctu.edu.tw

liouforrest@hotmail.com

學歷：

1997.9-2001.6 國立成功大學材料科學及工程系 學士

2001.6-2003.9 國立交通大學光電工程研究所 碩士

2003.9-2009.2 國立交通大學光電工程研究所 博士

博士論文題目：

在氧化鋅磊晶薄膜物理特性中晶體缺陷結構的角色

The role of crystal defect structures in the physical properties of ZnO epitaxial films

Publication list

I. Refereed Journal Publications:

1. **W.-R. Liu**, W.F. Hsieh, C.-H. Hsu, K.S. Liang, and F.S.-S. Chien, “Influence of the threading dislocations on the electrical properties in epitaxial ZnO thin films” *J. Cryst. Growth* **297,** 294-299 (2006).
2. **W.-R. Liu**, W. F. Hsieh, C.-H. Hsu,b, Keng S. Liang and F. S.-S. Chien, “Threading dislocations in domain-matching epitaxial films of ZnO,” *J. Appl. Cryst.* **40** 924-930 (2007).
3. Song Yang, Hsu-Cheng Hsu, **W.-R. Liu**, Hsin-Min Cheng, and Wen-Feng Hsieh, “Correlation between photoluminescence and varied growth pressure of well-aligned ZnO nanorods on fused silica substrate,” *Optical Materials* **30**, 502-507 (2007).
4. **W.-R. Liu**, Y.-H. Li, W. F. Hsieh, C.-H. Hsu, W. C. Lee, M. Hong and J. Kwo, “Correlation between crystal structure and photoluminescence for epitaxial ZnO on Si (111) using a γ-Al_2O_3 buffer layer,” *J. Phys. D: Appl. Phys.* **41**, 065105-1 - 065105-5 (2008).
5. **W.-R. Liu**, Y.-H. Li, W. F. Hsieh, C.-H. Hsu, W. C. Lee, Y. J. Lee, M. Hong and J. Kwo, “Domain Matching Epitaxial Growth of High-Quality ZnO Film Using a Y_2O_3 Buffer Layer on Si (111),” *Crystal Growth & Design* **9**,239-242(2009).
6. Jun-Rong Chen, Tien-Chang Lu, Yung-Chi Wu, Shiang-Chi Lin, **Wei-Rein Liu**, Wen-Feng Hsieh, Chien-Cheng Kuo, and Cheng-Chung Lee, “Large vacuum Rabi splitting in ZnO-based hybrid microcavities observed at room temperature,” *Appl. Phys. Let.* **94**, 061103-1 - 061103-3 (2009).
7. Chia-Lung Tsai, Yow-Jon Lin, Yi-Min Chin, **W-R Liu**, W. F. Hsieh, C-H Hsu and Jian-An Chu, “Low-resistance nonalloyed ohmic contacts on undoped ZnO films grown by pulsed-laser deposition,” *J. Phys. D: Appl. Phys.* **42**, 095108-1 - 065105-6 (2009)

II. Conference

1. **W.-R. Liu**, W. F. Hsieh, C.-H. Hsu, K. S. Liang, and F. S. -S. Chien, “Role of the threading dislocation on domain-epitaxially grown ZnO films using XRD and TEM,” Spring Meeting of Material Research Society (2006).
2. S.Y.Huang, **W.-R. Liu**, F. S. -S. Chien, C.-H. Hsu, K. S. Liang, and W. F. Hsieh, “Correlated scanning capacitance and conductive atomic force microscopy studies of dislocation in ZnO film,” Spring Meeting of Material Research Society (2006).

3. F. S. -S. Chien, **W.-R. Liu**, C. C. Tsai, C. Y. Li, C. C. Hsu, C.-H. Hsu,C. S. Chang, and C.-H. Hsu, “Effect of Dislocations on contact potential in epitaxial ZnO thin flims studies by electricostatic force microscopy,” Spring Meeting of Material Research Society (2006).
4. **W.-R. Liu**, Y.-H. Li, W. F. Hsieh, C.-H. Hsu, W. C. Lee, Y. J. Lee, M. Hong, and J. Kwo, “Y_2O_3 buffer layer for high-quality ZnO epitaxial growth on Si(111),” International Conference on Solid State Devices and Materials, Japan, Tsukuba, Sep. (2008).